Advanced Protection Schemes of Modern Transmission Grids with Large-Scale Power Electronics

Ma, Kaiqi

DOI (link to publication from Publisher):
10.54337/aau478976808

Publication date:
2022

Document Version
Publisher's PDF, also known as Version of record

ADVANCED PROTECTION SCHEMES OF MODERN TRANSMISSION GRIDS WITH LARGE-SCALE POWER ELECTRONICS

BY
KAIQI MA

DISSERTATION SUBMITTED 2022

AALBORG UNIVERSITY
DENMARK

ADVANCED PROTECTION SCHEMES OF MODERN TRANSMISSION GRIDS WITH LARGE-SCALE POWER ELECTRONICS

by

Kaiqi Ma

AALBORG UNIVERSITY
DENMARK

Dissertation submitted

.

Dissertation submitted: 29. April, 2022

PhD supervisor: Prof. Zhe Chen,
Aalborg University

Assistant PhD supervisor: Prof. Claus Leth Bak,
Aalborg University

PhD committee: Associate Professor Zhenyu Yang (chairman)
Aalborg University, Denmark

Professor Matti Ilmari Lehtonen
Aalto University, Finland

Professor Peter Palensky
TU Delft, The Netherlands

PhD Series: Faculty of Engineering and Science, Aalborg University

Department: Department of Energy Technology

ISSN (online): 2446-1636
ISBN (online): 978-87-7573-908-0

Published by:
Aalborg University Press
Kroghstræde 3
DK – 9220 Aalborg Ø
Phone: +45 99407140
aauf@forlag.aau.dk
forlag.aau.dk

Printed in Denmark by Stibo Complete, 2022

CV

Kaiqi MA was born in China. He received a B.Eng. degree in Automation from Hohai University, Nanjing, China, in 2012, and an M.Sc. degree in control engineering also from Hohai University, in 2015.

In the period of 07. 2015~01. 2018, he, being a junior engineer, worked for the R&D center of Xuji Group Corporation, State Grid, China.

He is currently a Ph.D. student at the Department of Energy, Aalborg University, Aalborg, Denmark. His research interests include renewable energy generation and control, and power system protection/control.

ENGLISH SUMMARY

In the modern power system, the transition of conventional fossil sources to renewable energies has achieved huge progress, which benefits from power electronic technologies, including the aspects of topology, control, stability, and reliability, etc. It contributes to reducing the stress on the global environment and achieving the goals of sustainable development. Typically, a growing numbers of renewable energy power plants are integrated (or upgraded) in the transmission level to bear massive electric power supply. Under such background, the conventional network protections face increasing adaptability problems, due to the different fault responses of non-synchronous (power electronic) generators compared with synchronous ones.

Since the majority of fault characteristics in the power system are generated by electrical sources, proper modeling of non-synchronous generators to reveal their fault characteristics is particularly important for analysis, design, and deployment of protective relaying. Regarding this, although several modeling methods have been reported, most of them have shortcomings and limitations, e.g. the simplification (or neglect) of the requirements for converter control during low voltage ride-through (LVRT) period. Line current differential protection and distance protection are two popular choices in the deployments of network protection, however, the existing assessments on these two protections fail to reveal the intrinsic links with various converter controls. Aiming at these issues, the thesis first deduces the sequence component models of the full converter coupled generator, which not only account for the typical fault control rules of LVRT but also are easy-to-use in protective study. Subsequently, the sensitivity problem of line current differential relay and the reliability problem of distance relay are comprehensively assessed, being highly correlated to the angle of converter's current references in positive sequence loop.

Prompted by the above challenges, several novel network protections are developed. On one hand, the time-domain differential principle using the compensated current is presented, where the mapping relationships of fault sampling to pre-defined fault models are employed for fault detection in the new differential protection. Compared to the conventional differential method using current comparison, the new principle reduces the correlation to the converter control.

On the other hand, for the reliability problem of distance relay during resistive faults in the line connecting non-synchronous generators, two types of countermeasures are developed to enhance the performance of conventional distance relay. The first type concerns the improvement of distance relay: 1) A complementary relaying scheme, working for the asymmetrical resistive grid faults, is developed. In contrast to the impedance (or distance) measurement comparison with pre-defined threshold in conventional method, the new scheme detects the faults by inherent angular tilts of apparent impedance, without over- or under-reaching issues. 2) An adaptive tilting

method of polygonal zone top-line is proposed. Compared with the existing off-line tilt function in some numerical relays, the new method can better handle the complex 'reach' problems due to the diverse converter control and intermittence of non-synchronous generator. The second type solves a relaying issue by the converter control. An upgrade fault control method for the converter is proposed to achieve the compatibility of the reactive current regulation of non-synchronous generator during LVRT period with accurate reactance measurement in distance protection.

In the thesis, the assessments on conventional protections, and the validations for the proposed network protections (or the fault control) are based on the targeted test models built in DIgSILENT/PowerFactory platform, while the new algorithms are implemented in Matlab. Besides, the protection compatible fault control scheme is also validated in the real-time simulation platform (Opal-RT).

DANSK RESUME

I det moderne elsystem har overgangen af konventionelle fossile brændstoffer til vedvarende energier opnået store fremskridt på grund af effektelektronik teknologier, herunder aspekterne topologi, kontrol, stabilitet og pålidelighed osv. Det bidrager til at reducere belastningen på det globale miljø og til at nå målene om bæredygtig udvikling. Typisk integreres (eller opgraderes) et voksende antal kraftværker til vedvarende energi i transmissionsniveauet for at sikre massiv elforsyning. På denne baggrund står de konventionelle netbeskyttelse foranstaltninger over for stigende tilpasningsevne problemer på grund af de forskellige fejlreaktioner hos ikke-synkrone (effektelektroniske) generatorer i forhold til synkrone generatorer.

Da størstedelen af fejlkarakteristika i elsystemet genereres af elektriske kilder, er korrekt modellering af ikke-synkrone generatorer med henblik på at afsløre deres fejlkarakteristika særlig vigtig for analyse, design og implementering af beskyttelsesrelæer. Selv om der er blevet rapporteret om adskillige modelleringsmetoder, har de fleste af dem mangler og begrænsninger, f.eks. forenkling (eller negligering) af krav til konverterens kontrol i LVRT-perioden. Linje-differentialbeskyttelse og afstandsbeskyttelse er to populære metoder i forbindelse med implementering af netværksbeskyttelse. De eksisterende vurderinger af disse to beskyttelse mangler imidlertid at afdække de iboende forbindelser med forskellige styringsstrategier for konverter. Med henblik på disse spørgsmål udledes i afhandlingen først sekvens komponent modellerne for den fulde konverterkoblede generator. Modellerne er ikke blot i overensstemmelse med de typiske fejlkontrolregler for LVRT, men er også lette at anvende i beskyttelsesundersøgelser. Efterfølgende vurderes følsomhed problemet i forbindelse med linje-differentialrelæet og pålidelighed problemet i forbindelse med afstandsrelæet grundigt. Disse to problemer er i høj grad korreleret med vinklen på konverterens strømreferencer i positiv sekvenskreds.

På baggrund af ovenstående udfordringer er der udviklet flere nye netværksbeskyttelser. På den ene side foreslås det differentielle princip i tidsdomænet baseret på den kompenserede strøm, som anvender afbildning relationerne for fejlprøvetagning til foruddefinerede fejlmodeller til fejldetektion. Sammenlignet med den konventionelle differentielle metode, der anvender strømsammenligning, reducerer det nye princip korrelationen til styringen af konverter.

På den anden side er der med hensyn til pålidelighed problemet af afstandsrelæet under resistive fejl i den linje, der forbinder ikke-synkrone generatorer, udviklet to typer modforanstaltninger for at forbedre ydeevnen af konventionelle afstandsrelæer. Den første type vedrører forbedring af afstandsrelæet: 1) Der udvikles en supplerende relæordning, der fungerer for asymmetriske resistive netfejl. I modsætning til sammenligningen af impedans- (eller afstands-) målingerne med en foruddefineret

tærskel i den konventionelle metode, registrerer den nye ordning fejlene ved hjælp af iboende vippevinkel af den tilsyneladende impedans uden problemer med over-rækkevidde eller under-rækkevidde af relæer. 2) Der foreslås en adaptiv vippemetode for den zone øverste linje af polygonale afstandsrelæer. Sammenlignet med den eksisterende offline vippemetode i nogle numeriske relæer kan den nye metode bedre håndtere de komplekse "reach"-problemer på grund af den forskellige konverterstyring og intermittence af ikke-synkron generator. Den anden type løser et problemer for beskyttelse ved hjælp af konverterstyring. Der foreslås en opgraderet styringsmetode for konverteren for at opnå kompatibilitet mellem reaktiv strøm regulering af den ikke-synkrone generator i LVRT-perioden og nøjagtig måling af reaktans i afstandsbeskyttelse.

I projektet er vurderingerne af konventionelle beskyttelser, og valideringerne for de foreslåede netværksbeskyttelser (eller fejl styringsmetode) er baseret på de testmodeller bygget i DIgSILENT/PowerFactory platformen, mens de nye algoritmer er implementeret i Matlab. Derudover er den beskyttelseskompatible fejl styringsskema også valideret i realtid simulering platformen (Opal-RT).

ACKNOWLEDGEMENTS

The Ph.D. project, entitled “advanced protection schemes in modern power system with large-scale power electronics”, is carried out from Ferbrary 2018 to April 2022, under the supervision of Prof. Zhe Chen and Prof. Claus Leth Bak. This Ph.D. project is financially supported by the Department of Energy, Aalborg University (ET-AAU). I would like to express my sincere gratitude to them and to Lasse Rosendahl, Mikkel Lønsman Hukiær, Tina Larsen, Corina Gregersen from AAU for their help smoothing my study here.

Great thanks should be given to my supervisor Prof. Zhe Chen. Thanks for providing me the precious opportunity and creative environment to pursue my Ph.D. degree in AAU. Thanks for your constructive guidance, detailed suggestions and patient discussions on this project. Your rigorous work style also motivates my future career deeply. Sincere thanks should also be given to my co-supervisor, Prof. Claus Leth Bak, for your inspired advices and invaluable support to my study and research grogram in AAU.

At the same time, I would like to thank Prof. Hans Kristian Høidalen for his support on the academic discussion and my visiting study in Norwegian University of Science and Technology. Thanks are also given to Dr. Zhou Liu, Assistance Prof. Yanbo Wang, Dr. Weihua Zhou, Mr. Manuel Castillo, Dr. Raymundo E. Torres-Olguin Dr. Nan Qin for the great help in the academic area discussion. All your help enriched my Ph.D. research. Then I appreciate my love Shuangshuang Xu with her support and care of my life. Thanks.

Special thanks to my parents, sparing no effort to support me.

Finally but significantly, I would like to say thanks to all my best friends here. Your names are engraved in my heart. I will cherish the golden time in AAU for the rest of my life.

Kaiqi Ma

April 2022

Aalborg

TABLE OF CONTENTS

LIST OF ACRONYMS

AC	Alternating current
BCC	Balanced current control
CWIT	Clockwise impedance tilt
Counter-CWIT	Counter-clockwise impedance tilt
DC	Direct current
DITA	Deviation of impedance tilt angles
DSC	Decoupled sequence control
FCG	Full converter coupled generator
ITA	Impedance tilt angle
ITA-21	Impedance tilt angle-based distance protection
L-G	One-phase-to-ground short-circuit
L-L	Phase-to-phase short-circuit
L-L-G	Phase-to-phase-to-ground short-circuit
LVRT	Low voltage ride-through
3PH	Three-phase short-circuit
MMI	Model mapping index
NSG	Non-synchronous (power electronic) generator
PCC	Point of common coupling
PCFR	Protection compatible fault regulation
PCG	Partial converter coupled generator
PEC	Power electronic converter

PZTL	Polygonal zone top-line
SG	Synchronous generator
UVR	Unsymmetrical vector reconstruction
WTG	Wind turbine generator
21	Distance relay
87	Differential protective relay
87L	Line current differential relay

TABLE OF FIGURES

CHAPTER 1. INTRODUCTION

Power system protection works for the isolation of short circuit faults (used as 'fault' in short in the thesis), being the first defense-line to ensure the operating security of power system. This Ph.D. project focuses on the protective issues in the transmission network, derived from the nowadays development of advanced electrical generation.

In this chapter, the background and motivations of this Ph.D. project are first introduced. Secondly, the research problems are formulated, followed by the investigation of the state of the art for the research problems. Subsequently, the contributions of the Ph.D. project are concluded. Finally, the thesis outline and the list of publications related to the thesis are presented.

1.1. BACKGROUND AND MOTIVATION

As reported in [1], Europe's energy system is undergoing deep decarbonization, aiming at the goal of zero net greenhouse gas emissions by 2050. In the energy transition, various renewable energies are gradually substituting fossil energies. The consequent changes of generating pattern lead to the large penetration of non-synchronous (power electronics) generators (NSGs), accelerating the power electronic-oriented trend of modern power grids [2]. This trend is particularly obvious in Denmark. Figure 1-1 depicts the estimated share of different renewable energies to expected electrical gross energy consumption in electricity from 2021 to 2030 in Denmark [3].

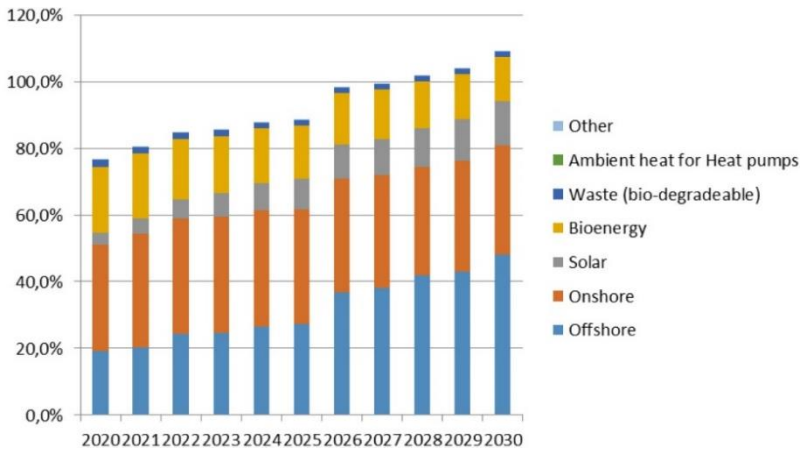

Figure 1-1 Estimated trajectory of renewable energy share in electricity [3]

The ongoing energy substitution improves the dynamic performances of power system, such as the flexible power-flow interaction [4-7], and voltage control [8-9]. But it also raises issues of the low system inertial [10-11] and the adaptability problems of conventional protection methods, etc. Specific to the causes of relaying adaptability, one can analyze from three aspects. In detail,

- The power electronic-oriented trend of modern power system leads to special short-circuit characteristics in fault networks. At the NSG-sided system, these characteristics include the suppressed short-circuit current [12-14], the possibly unstable equivalent impedance of the power source [15-16], and sometimes the severe distortion of fault current and voltage, i.e. the harmonic characteristics [17-18], etc. In general, these fault characteristics are due to the vulnerability of power electronic converters (PECs) and the inherent control pattern of PEC devices themselves, which will affect the functions of conventional protections in a certain degree.
- The diversity of fault control strategies of NSGs, as well as their flexible deployments in different voltage levels, will cause the variation of network parameters or even topologies. For instance, the local network connecting NSGs may operate in the 'island mode' under certain grid fault conditions [12]. In another view, the different types, penetration, and grid-connecting points of NSGs lead to the change of fault levels in NSG-integrated distribution network [19]. These raise the adaptive requirements on the traditional protections adopting preset thresholds, for example, reset relays as per the changing fault level. Ref. [20] assesses the feasibility of the adaptive protection scheme in the power systems integrating bulk NSGs, based on the connection of all relays, switches, and control centers through bi-directional communication links.
- Commonly, the design and deployment of NSG protection/control is independent to the vicinal network protection. The resulting incompatibility (or even conflict) in response speeds and acting objectives of each other may increase the malfunction risk of conventional protections. Bearing the controllable ability of PECs during faults in mind, one can reasonably infer that the protection reliability and sensitivity can be improved by means of the cooperative control of PEC within its safety margin. Some interesting explorations have been reported on the revision of power electronic control to achieve the protection target in flexible direct current (DC) power grids. Ref. [21-24] have developed several new submodule structures of the modular multilevel converter, e.g. the full-bridge type, the clamp-double type, the self-resistance enhanced type, and the diode-based clamp type, to improve the capability of modular multilevel converter for DC fault clearance.

During the energy transition, massive NSGs organized as power plants at the sub-transmission (or transmission) system is one of the mainstream integration method, especially for the regions with concentrated endowment of renewable resources, e.g. Denmark [3], China [25], etc. In fact, the primary electrical components in power

system are subject to faults, which is inevitable and attributed to various causes. However, according to the latest statistic report [26], the most vulnerable link in the electric power system to faults is the transmission network, especially the transmission line. Because the transmission line is generally exposed to atmospheric conditions. It is pointed out that the average percentage of faults on the transmission lines occupies about 50% of all faults (10-year average) in Denmark. And this value even reaches 61 % in the Nordic and Baltic areas. Thus, the transmission network protections are of high importance.

In the context of these potential risks, the development and validation of novel network protection schemes and the upgrade of the PEC fault controls are of theoretical and practical significance to facilitate the security operation and management of the modern power system with large-scale NSGs installation.

1.2. PROBLEMS FORMULATION

This Ph.D. project focuses on the transmission network protections, in the context of large-scale NSGs integration. In the transmission network, line differential protection and distance protection are two kinds of the primary means with widespread application. As we know, almost all the fault characteristics are driven by power source, except for the wave propagation. Thus, identifying fault characteristics is of importance for protective relaying. However, the fault control strategies of PEC affect the fault characteristics reflected in the protections in a power system connecting NSGs.

Proper short-circuit model of electrical component is the basis of short-circuit analysis, protection design, and setting. The first research problem for this project is,

Problem 1: What are the mainstream PEC fault control methods? Which PEC fault control is the most promising approach in the future? How to determine the short-circuit model of NSG (considering the characteristics of PEC control) to be compatible with the protective analysis?

Following the built NSG short-circuit model(s) are the second and third research problems,

Problem 2: What are the failure mechanisms of conventional network protections in the future power system with high penetration of NSGs? By failure mechanism, I mean the causes leading to the malfunction in a relay. In this thesis, the line current differential relay (ANSI/IEEE code 87L)[1] and the distance relay (ANSI/IEEE code 21)[1] deployed in the transmission grid will be evaluated, respectively.

1. ANSI/IEEE C37.2-1991, "IEEE Standard Electrical Power System Device Function Numbers," IEEE, New York, 1991.

Problem 3: Based on the assessment of the above two protection schemes in *problem 2*, how to improve the conventional protection schemes (or design novel protection schemes) for future power networks with high penetration of NSGs? This will be the main goal of this Ph.D. project.

1.3. STATE OF THE ART

This project focuses on the protection and control for the power grids connecting large-scale NSGs, including the network protections and the coordination between network protection and PEC protection/control. The state of the art regarding the research problems is introduced below. From the perspective of the different grid-connection modes, the mainstream NSGs mainly include two categories, as displayed in Figure 1-2.

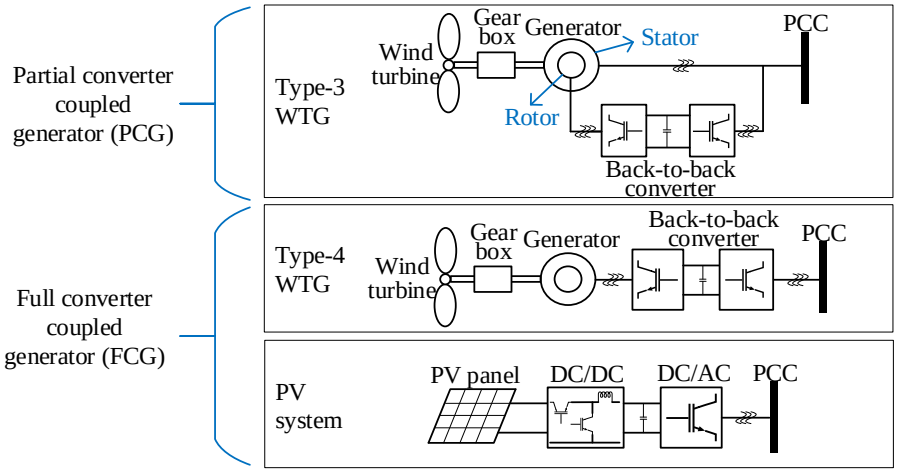

Figure 1-2 Grid connection modes of different NSGs

First, the partial converter coupled generator (PCG) refers in particular to the Type-3 wind turbine generator (WTG). In the physical configuration of PCGs, the stator of the inductor machine follows the direct connection with the point of common coupling (PCC), while a back-to-back converter is deployed in between the machine rotor and the PCC point. Since mainly the excitation current flows through the rotor loop, the converter occupies a low proportion of the total machine capacity, normally 25% [27]. Due to the merits of efficient energy conversion and small PEC capacity [27-28], PCGs have an evident installation rate in the modern wind power generations [29].

On the other hand, type-4 WTGs and photovoltaic (PV) systems are full converters coupled to the external grid, which are collectively called FCGs in this thesis. In

contrast to the PCG, the response of FCG, e.g. to power system faults, is completely determined by the control strategy employed in PECs [30].

To date, many fault-related research works on NSG-based generation systems, e.g. short-circuit calculations, protection adaptability, control system design, have been reported.

NSGs often respond sensitively during abnormal system conditions (such as the system short-circuit). In the past, the NSGs are generally isolated from the grid to protect the PEC components from the large transient overcurrent. With the rapid popularity of NSGs, many transmission system operators around the world have defined the grid codes for the fault control of NSGs to support voltage recovery and system stability during faults [31-33]. Following such requirements, the NSGs cannot disconnect from the grid, directly. This is the so-called low voltage ride-through (LVRT) technique of NSGs.

1.3.1. SHORT-CIRCUIT MODEL OF RENEWABLE GENERATOR

In the PCG system, the LVRT solution of a crowbar circuit is commonly adopted to isolate the rotor side converter after the grid fault is detected [27, 34]. To date, many research works on the fault characteristics of PCGs have been performed with the consideration of LVRT capability. In [35], the magnetic flux of PCG based on the superposition of a forced component and a natural one is used to analyze the transient overcurrent during symmetrical grid faults. Ref. [36] deduces the short-circuit current analytic expression of PCG (considering the crowbar effect during symmetrical grid faults), and meanwhile quantitatively determines the maximum short-circuit contribution. In [37], a more practical expression of short-circuit current is deduced from the view of complex topology of PCG cluster for engineering application. Moreover, the asymmetrical fault condition is proved more harmful to the PCG than the symmetrical one [38]. The analytical current expressions of the PCG operating under asymmetrical fault conditions are deduced in [39].

Concluding from [36, 39-40], the characteristics of PCG's fault current highly relate to the operating status (i.e. activation or not) of crowbar protection. What has aroused wide concern is the frequency deviation of stator current during crowbar circuit in-service. At this moment, the fault current of PCG stator is the result of a forced alternating current (AC) overlapping with a natural current, where the natural current consists of two decaying components, i.e. an AC component at rotor speed frequency and a DC component. In contrast, the current component at rotor speed frequency is absent when the crowbar circuit is out of service.

For the FCGs, the PEC control fully determines the fault characteristics, featuring as,

- PECs usually consist of multiple semiconductor devices, which are quite expensive and are not designed to handle large currents. Usually, PECs can only provide an overcurrent at a relatively low level, about (1.1 ~ 2) p.u [14]. However, a traditional synchronous generator (SG) may supply a fault current more than 10 times (10 p.u.) of its rated current [41].
- Compared to a SG, FCG may perform delayed fault response due to the inherent control feature of PECs. In detail, FCG begins to provide fault current after a delayed detection and the current follows with a ramp-up regulation [42].
- PECs may behave different fault characteristics due to their diverse fault control schemes. In addition, PEC output during fault transient shows strong nonlinear characteristics, which also relates to the control system [30, 43].

At present, the mainstream short-circuit model of FCG is generally over simplified, e.g. the Thevenin voltage source circuit [44-45], or the current source with user-defined short-circuit capacity [46-47], where the complex characteristics of PEC control are ignored. In [46-47], the short-circuit models of FCG consider the PEC current limits, however, none of them accord with the LVRT requirements of majority grid codes for grid voltage support during faults. Besides, the constant voltage source representation of a FCG in parallel with the variable impedance is reported in [48]. However, the PEC control of grid voltage support is disregarded, either. In [49], the improved Thevenin voltage source model covers the dynamic supporting requirement of reactive power but applies for the short-circuit calculation only. In [50], the phasor-domain modeling method is deduced from the controllable equivalent circuits of FCGs, which incorporates the LVRT function in an iterative way. However, this model is only valid for the PECs occupying the coupled sequence control.

During unbalanced system conditions or grid faults, FCGs adopting the coupled sequence control produce the second harmonic oscillations in the active power and the DC side voltage, which is due to the existence of the negative sequence component in the PCC voltage. For this, many research works point out that the decoupled sequence control (DSC) scheme of PEC can eliminate the second harmonic influence [51]. From the perspective of the protection system, the DSC is promising to emulate the fault behavior of SG and mitigate certain control-caused relaying issues, which has attracted many attentions for the PEC control [51-52]. In [52], a phasor-domain modeling approach of FCG for short-circuit computation is presented, which considers the situation of modern DSC strategy.

1.3.2. DEVELOPMENT OF NETWORK PROTECTIONS AND CHALLENGES

In this section, the developments of different network protections and their coordination with power electronic control are reviewed separately. The protective challenges in the power system connecting large-scale NSGs are also included.

A. differential protection

Differential protection is the unit-type protection adopted for a specified electrical component in the power system, e.g. power transformer, transmission line, generator or power substation, etc. [53]. Due to its simple principle, differential protection can provide absolute selectivity and fast operation. Commonly, differential protection based on Kirchhoff's current law compares the input currents of the protective zone with the output ones, where the protective zone is seen as an electric 'node'. Thus, a communication link is required if the data acquisition terminals have a certain electrical distance from each other. The development of cost-effective communication systems, e.g. metallic pilot wires, fiber optic cables, and directional radio links, enables the application of differential protection for protection objects with a long electrical distance. For the deployment in transmission networks, current comparison-based differential protection is the simplest and most frequently applied type. With the recent development against various application problems, many novel line current differential protections have been reported. Ref. [54] improves the operating stability of the conventional line differential protection by introducing the adjustable restraining coefficients. In [55], the line current differential protection adopting the continuous wavelet transform algorithm shows strong robustness to CT saturation. For the influence of high resistive faults as well as the unbalanced pre-fault system conditions on the phase current based α-plane differential protection, a supplemental criterion using the angular difference between voltage and current and the current magnitude variation is developed [56]. In addition, many new differential protection principles are also reported. In [57], a new α-plane based on the incremental complex power is defined, which has simple setting requirements and excellent performance. Besides, the differential protections based on the comparison of fault network impedance also show good performances [58-59].

For the assessment of line current differential protection in the networks connected to NSGs, most of the existing researches focus on the PCGs-integrated power system [65-67]. As mentioned in section 1.3.1, the current contribution of PCG includes a current component at the rotor speed frequency when the crowbar circuit is put into service after grid faults. It can bring in the fluctuation of differential and restraining currents (at fundamental frequency), leading to a certain malfunction risk of the line current differential protection [67]. Note that, the malfunction risk is easy to happen when the PCGs have a high penetration level. On the other hand, it should be pointed out that the above relaying risk only exists in the fault transient and will decrease

gradually, resulting from the decaying characteristic of the non-fundamental frequency current component.

As for the FCGs-integrated power networks, study on the performance of line differential protection is relatively narrow. Ref. [71] reports the starting problem of the pickup element in the line current differential protection, and an auxiliary low-voltage component or remote-end relay signal is suggested to address this problem. In [72], the influence of the FCG-based plant on the differential protection is investigated from the perspective of different features of current's phase angle. However, the regular influences from different PEC fault controls are not analyzed. Ref. [73] outlines the influencing factors of a transmission system connecting FCG-based plant on the current differential protection. However, the FCG-based plant commonly operates according to a certain grid code during grid faults, and such reality is not directly mentioned. In addition, some interesting explorations on improved current differential protections have been reported. Ref. [74] discusses the current differential protection based on the positive sequence fault component in the active distribution networks connecting FCGs. Ref. [75-76] develop a series of novel multi-terminal current differential protections of active distribution networks, being based on the FCG fault (or fault component) current estimation. Ref. [77] improves the sensitivity and reliability of the conventional current differential protection in the line connecting FCG-based plant by introducing a differential coefficient.

B. Distance protection

The basic principle of distance protection is to compare the measured line impedance from relay location up to fault point with a pre-defined threshold. Distance protection has been widely adopted to protect the transmission line, since only the local current and voltage measurements of relay device are used in the impedance computation, without additional communication requirements as in differential protection. According to the operating characteristics on the impedance plane, the popular types include the Mho characteristic, the reactance characteristic, and the polygonal characteristic, etc. [53, 60]. Because of the inaccurate impedance measurement of distance relay resulting from measuring errors, CT errors, and the inaccurate line impedance, at least two protective zones with a certain time grading are needed to reach 100% of the protected line in practice. For example, zone 1 commonly covers 80~85% of the protected line, while zone 2 covers the entire length of the first line and 20~50% of the subsequent line (no more than zone 1 of the next relay) [60]. Similarly, many novel distance protections focusing on different application scenarios have been reported. Aiming at the change of line positive sequence impedance in a series compensated system, a distance protection scheme based on the mutual impedance of line is developed in [61]. In [62], a novel impedance calculation method is developed to eliminate the influence of large fault resistance. Ref. [63] presents a non-communication distance protection that improves the detection speed for faults at the end of the line. In [64], a novel time-domain distance protection by

incorporating the parameter identification theory is presented, showing fast tripping speed and strong adaptability to fault transients.

Similar to the line current differential protection, the distance protection equipped in the outgoing lines of PCG-based plant performs a similar transient problem after the activation of crowbar protection, as reported in [39, 68-70]. Compared to the differential protection, the transient influence is much severe for distance protection using only the single-end measurements. Furthermore, the time-domain distance protection is reported to be a good choice to address transient adaptability [39].

For the distance protection installed in the transmission lines emanating from FCG-based plant, research works on the operational risks concerning the impedance element [78-81], the directional element and relay characteristic [78], as well as the phase selector [82], have been reported. As mentioned in [78], the proper selection of the directional element and the relay characteristic in accord with the PEC fault control mode and the fault type is necessary. Ref. [82] points out, the replacement of the current-based phase selector with the voltage-based one may be more effective in the system connecting the FCG-based plant. In fact, the malfunction risk due to the error of reactance measurement (during resistive faults) in the impedance element is worst. In [79], a supplemental solution incorporating the zero-sequence impedance criterion and the time grading with the backward position relay is reported. In addition, many adaptive distance protections are reported [83-85]. Generally speaking, they define an adaptive quadrilateral trip boundary based on the varying fault location, fault resistance, and the pre-fault system loading. However, the FCGs considered in [84-85] are deemed to accord with a Thevenin voltage source model, which does not conform with the realistic FCGs with LVRT capabilities. Recently, several protective solutions of transmission lines connecting FCG-based plant are reported, which are followed for either protection decision [86-87] or distance relay setting [88]. However, these proposals are all based on the premise of homogeneity in the external grid, which may not be always valid in practice.

C. Coordination between network protection and power electronic control

With regard to the coordination between the protection system and the PEC control, Ref. [89] has reported a coordination method between the protection system and the controllable power of HVDC link in the AC system based on the voltage stability index. It demonstrates the possibility of coordinating the over-current protection with the HVDC power flow controller in order to alleviate the voltage instability problem. Another interesting exploration on the coordination between protection and PEC control in the DC grid of a HVDC system is the fault detection under a weak current condition by switching the modular multilevel converter into non-controlled rectifying mode [21]. In addition, considering the controllable ability of PEC, a control-based solution for the FCG has been presented to improve the accuracy of

measured impedance in distance protection [81], however, no comments on the consistency with existing grid codes are reported.

Except for the classical protection methods, many advanced protection methods, e.g. wide-area protections [90-92], multi-agent technology-based protections [93-95], and adaptive protections [96-97], have been presented. These benefit from the rapid development of measurement technology, communication means, and Intelligent Electronic Devices. Actually, the coordination between these intelligent backup protections acting on the wide-area system and the local protections is promising to handle the protective issues of complicated modern power networks with large penetration of NSGs. However, the influence of the NSGs and the countermeasure need a further investigation.

1.4. CONTRIBUTIONS

Compared with the PCG, the research in FCG modeling and protection related assessment is prone to the PEC controls and needs more work. The Ph.D. project focuses on the FCGs and the contributions of this thesis can be clarified as follows:

On the short-circuit model of FCG:

- Introduce a general FCG modeling method for protective analysis. Compared with the existing modeling works, the newly deduced sequence models of FCG incorporate the current regulating rules of modern grid codes and contain definite physical meaning.
  Papers related to this contribution are J3 and J6.

On the line differential protection:

- Assess the conventional line current differential relay in the transmission system connecting FCG-based plant. This contribution deeply reveals the inner relations between the sensitivity problem of differential relay and the different operating modes of FCG during grid faults.
  Paper related to this contribution is J5.

- Propose a novel time-domain differential protection principle based on the compensated current. The newly proposed time-domain differential principle identifies faults according to the mapping relations of fault sampling to predefined fault network models. Its application in SG-dominated transmission networks and revision in the presence of FCG-based plant are discussed, separately.
  Papers related to this contribution are J1, J2 and C1.

On the distance protection:

- Assess the conventional distance protection in the outgoing line of FCG-based plant. This work comparatively analyzes the malfunction tendencies of relay during resistive faults, where different factors, e.g. FCG fault controls, fault types, fault resistance, and penetration level of FCG, are included.
  Paper related to this contribution is C2.

- Develop a novel distance protection of the outgoing line from FCG-based plant during asymmetrical resistive faults. The innovative relaying method detects faults by comparing the tilting angles of the apparent impedance to two line impedance up to different pre-defined positions on the protected line.
  Paper related to this contribution is J6.

- Present an adaptive zone setting scheme suitable for the polygonal distance relay in the lines emanating from FCG-based plant. In contrast to the existing zone tilt setting scheme, the new proposal is a kind of on-line method, and can adaptively compensate for both the possible over- or under-reaching problems during asymmetrical grid faults.
  Paper related to this contribution is J4.

- Propose an upgrading method of the FCG control for resistive faults in the outgoing line of FCG-based plant. The improved FCG control can improve the accuracy of fault distance ‘seen’ by the vicinal distance protection. This improvement aims at eliminating the error of apparent impedance in the reactance direction by adjusting the active current of positive sequence control system, which does not conflict with the reactive current supporting rules of grid codes.
  Paper related to this contribution is J3.

1.5. THESIS OUTLINE

This thesis contains seven chapters. The main body of the thesis, from Chapter 2 to Chapter 6, is organized according to the above contributions and illustrated as the following logic diagram.

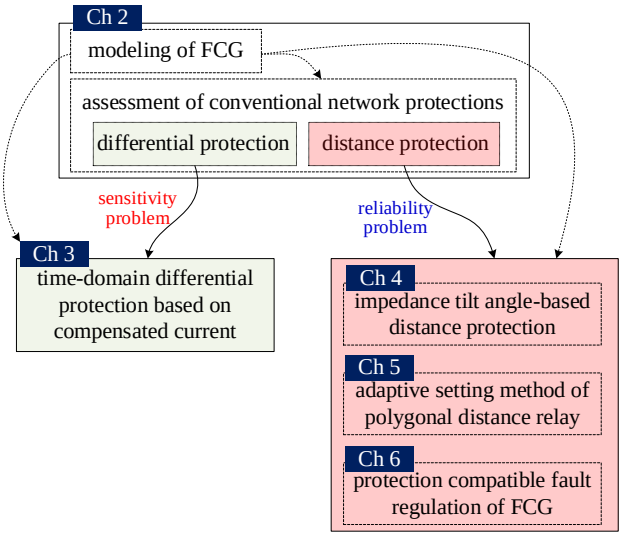

Figure 1-3 Logic diagram of main chapters

Chapter 1 gives a brief introduction of the Ph.D. project, including the background and motivations, the problem formulation, the state of the art, the contributions, the thesis outline, and the list of publications.

Chapter 2 starts with the sequence component modeling of FCG during grid faults, which will support the protective analysis and design in other chapters. Then, the sensitivity issue of line current differential protection due to the different features of current angle during different PEC's fault control modes is elaborated. In parallel, the reliability problems (i.e. over- and under-reach) of distance protection during resistive grid faults caused by the PEC fault controls are analyzed. In addition, the influence of network configurations (i.e. meshed vs. radial) on both two conventional network protections are compared.

Regarding the sensitivity issue of line current differential protection analyzed in Chapter 2, the novel differential principle using the model mapping relations is presented **in Chapter 3**. This chapter begins with the basic definition of compensated current and related differential equation in time-domain. And, the feasibility for fault identification is preliminarily validated. Following this, the new principle is enhanced by incorporating a restraining equation. And, comprehensive simulations based on a SG-dominated system are carried out to validate the performance of the enhanced

differential scheme. Finally, the modulus selection for restraining equation, considering the different features of FCG's short-circuit models, is revised for the application in a transmission system connecting FCG-based plant. The further simulation studies of revised new differential scheme prove its excellent adaptability compared to the traditional one, in the presence of FCG-based plant.

The following three chapters propose three different countermeasures, revolving around the over- or under-reaching problems of distance protection in the outgoing line of FCG-based plant (summarized in Chapter 2).

Chapter 4 presents an impedance tilt angle-based distance protection. This chapter firstly defines two tilting angles of the apparent impedance sensed by distance relay. The qualitative relationships of these two angles under all forwards faults along the protected line are then combed, where the possibly different fault conditions due to the diverse PEC control modes are considered. Based on this, the new criterion for fault detection is built and the implementing process is refined. After that, a comprehensive simulations are conducted, which covers the influences of diverse PEC control modes, operating dead zone, and different control deployments. The results validate the feasibility and effectiveness of the new protection scheme.

Chapter 5 formulates an adaptive tilt setting scheme of polygonal distance relay. This chapter firstly analyzes the challenges of the existing zone tilt setting function in some numerical relays, in the line connecting FCG-based plant. By incorporating the effects of PEC fault control on the impedance tilt sensed by distance relay, a new adaptive tilt setting scheme of polygonal zone top-line is developed. For efficiency consideration, the new setting scheme is further refined by introducing the pickup criteria for specific fault conditions. Since the same tilting angles defined in chapter 4 are used, partial of the test scenarios in the previous chapter are re-used to elaborate the performance of the new tilt setting method. Meanwhile, the influence from FCG's intermittent characteristics are analyzed. Finally, the error property of the new tilt setting method due to the estimated tilting angles is assessed.

Chapter 6 addresses the same protective issue from a control-based perspective. Firstly, the feasibility of the protection compatible fault regulation for FCG is elaborated. Then, the adaptability of FCG's short-circuit models in the presence of protection compatible fault regulation is analyzed. Following this, the basic principle of how to incorporate the target of minimized error of relay's reactance measurement into the FCG active current control is presented. In the final stage, both the commercial software (DIgSILENT/PowerFactory) and the real-time simulation based on the Opal-RT are used for validation. This proves the effectiveness and authenticity of the new control proposal.

The concluding remarks and the future perspectives of this research project are organized in **Chapter 7**.

1.6. LIST OF PUBLICATIONS

A list of publications related to the thesis is given below. It contains 6 journal papers and 2 conference papers. They have been published or under review, where the journal papers are marked as J1-J6 and the conference papers are marked as C1-C2.

Journal papers:

J1. K. Ma, Z. Liu, C. L. Bak, Z. Chen, “Novel differential protection based on the ratio of model error indices in time-domain for transmission cable system”, Electric Power Systems Research, Vol. 180, 106077, 03.2020.

J2. K. Ma, Z. Chen, C. L. Bak, Z. Liu, M. Castillo, R. E. Torres-Olguin, N. Qin, “Novel differential protection using model recognition and unsymmetrical vector reconstruction for the transmission line with wind farms connection”, International Journal of Electrical Power and Energy Systems, Vol. 123, 106311, 12.2020.

J3. K. Ma, Z. Chen, Z. Liu, Zhou; C. L. Bak, M. Castillo, “Protection collaborative fault control for power electronic-based power plants during unbalanced grid faults”, International Journal of Electrical Power and Energy Systems, Vol. 130, No. 107009, 09.03.2021.

J4. K. Ma, H. K. Høidalen, Z. Chen, C. L. Bak, “Improved zone 1 top-line tilting scheme for the polygonal distance protection in the outgoing line of type-4 wind parks”, Journal of Power and Energy Systems, second revision.

J5. K. Ma, Y. Wang, Z. Chen, “Analysis of the line current differential protection considering inverter-interfaced generation station and countermeasures”, Journal of Yangtze University, accepted.

J6. K. Ma, Z. Chen, C. L. Bak, “Novel control compatible distance protection in the outgoing line of type-4 wind power plants”, IEEE transactions on power delivery, submitted.

Conference papers:

C1. K. Ma, Z. Chen, C. L. Bak, Z. Liu, “A Novel Model Recognition -based Current Differential Protection in Time-Domain”, Proceedings of 2019 IEEE Milan PowerTech, Milano, Italy, 2019.

C2. K. Ma, Z. Liu, Z. Chen, C. L. Bak, M. Castillo, “Influence of converter-based power sources on the distance relay under system asymmetrical Faults”, 2020 12th IEEE PES Asia-Pacific Power and Energy Engineering Conference (APPEEC), Nanjing, China, 2020.

CHAPTER 2. SHORT-CIRCUIT MODEL AND PROTECTIVE CHALLENGE IN MODERN POWER NETWORK CONNECTING FCG-BASED PLANT

Power system fault analysis is to calculate the current and voltage in the network under a fault condition, which is the basis of power system design, control and management, power equipment selection, protection system settings, and emergency control design, etc. In three-phase AC power circuits, the short-circuit faults are usually resulted from the breakdown of insulation between one phase and other phase(s) (or earth) [53]. In detail, it mainly follows:

- One-phase-to-ground short-circuit (L-G).
- Phase-to-phase short-circuit (L-L).
- Phase-to-phase-to-ground short-circuit (L-L-G).
- Three phases short-circuit (3PH-G or 3PH).

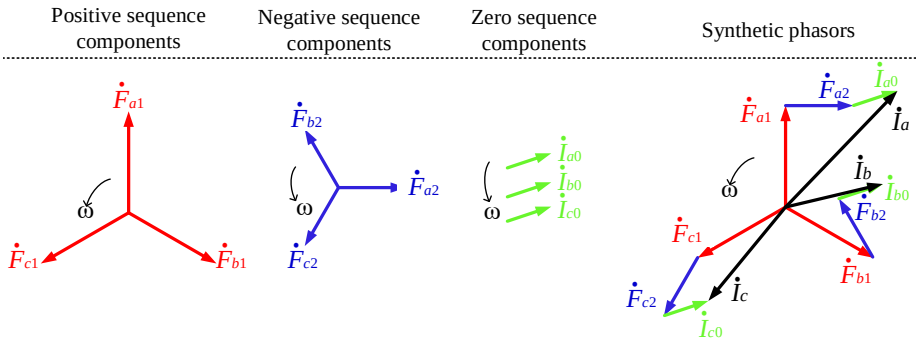

1) Phase sequence in positive sequence system—phase A leads phase B, and phase B leads phase C;

2) Phase sequence in negative sequence system—phase A leads phase C, and phase C leads phase B;

3) Phase A, B, C stay in-phase in zero sequence system;

4) Superposing each sequence phasors, one can get the original current phasors in phase-domain.

Transformation formula from phase components to sequence components ($\alpha = e^{j\cdot 120^\circ}$ is the rotation factor):

$$\begin{bmatrix} \dot{F}_{a1} \\ \dot{F}_{a2} \\ \dot{F}_{a0} \end{bmatrix} = \frac{1}{3} \cdot \begin{bmatrix} 1 & \alpha & \alpha^2 \\ 1 & \alpha^2 & \alpha \\ 1 & 1 & 1 \end{bmatrix} \cdot \begin{bmatrix} \dot{I}_a \\ \dot{I}_b \\ \dot{I}_c \end{bmatrix} \quad \begin{cases} \dot{F}_{b1} = \alpha^2 \cdot \dot{F}_{a1}, & \dot{F}_{b2} = \alpha \cdot \dot{F}_{a2}, & \dot{F}_{b0} = 1 \cdot \dot{F}_{a0} \\ \dot{F}_{c1} = \alpha \cdot \dot{F}_{a1}, & \dot{F}_{c2} = \alpha^2 \cdot \dot{F}_{a2}, & \dot{F}_{c0} = 1 \cdot \dot{F}_{a0} \end{cases}$$

Figure 2-1 Symmetrical components and the synthetic phasor [98]

For asymmetrical faults, such as L-G or L-L faults, the symmetrical component method is a powerful tool for analysis. By means of this method, any set of three-phase asymmetrical physical quantities (e.g. voltage, current, etc.) can be decomposed into three sets of symmetrical physical quantities in the same frequency. Taking a common three-phase quantity $\dot{F}_{abc}$ as an example, the phasor plane representation of the symmetrical component method is concluded in Figure 2-1. Subscripts '1, 2, and 0' represent the positive, negative, and zero sequence components, respectively.

Notably, there exist mature sequence models for common electric components to support the application of symmetrical component method in the SG-dominated power networks.

In this chapter, the key technical aspects to be solved include the analysis of PEC's operating mechanism during grid faults (i.e. the modeling analysis of FCG) and the assessments of conventional network protections.

2.1. SHORT-CIRCUIT MODEL OF FCG

A review of fault analysis and protective assessment for the PCGs-dominated power networks has been outlined in section 1.3, which will not be repeated in this chapter.

For analyzing and designing network protections in the rest content of this thesis, the steady-state short-circuit models of FCG in sequence systems are revised based on the existing knowledge in [50-52, 99]. The equivalent parameters in different sequence circuits relating to the modern LVRT control requirement are deduced.

During the abnormal system condition, the FCG is thought of operating as a controlled current source, where the outer power control loop(s) is generally bypassed [100]. Under such condition, the reference inputs of the inner current control loop are generated by the deployed grid codes.

Figure 2-2 illustrates the DSC block diagram of PECs operating in the grid synchronous coordinates (angular velocity is indicated as ω). In Figure 2-2, U_{dc} is the DC link voltage of the PEC; i_{gabc} and v_{gabc} are the instantaneous current and voltage at the PCC point; i''_{dq}, i_{dq}, and v_{dq} are respectively the current reference, current feedback, and voltage feedforward components in the rotating reference frame. Note that a rotating factor S is adopted to simplify the assignment of negative sequence current references, as the phase-locked loop of the whole control system is based on the positive sequence system voltage.

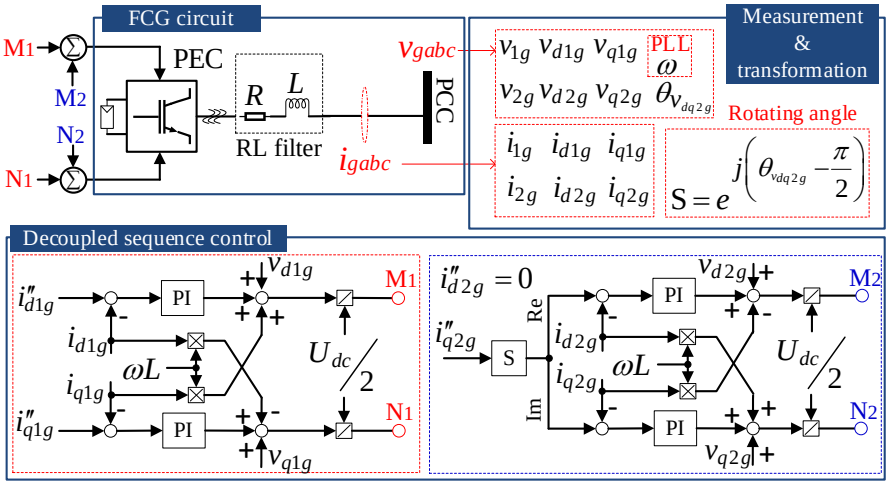

Figure 2-2 The DSC diagram of PEC [100]

In general, most of the protection systems concern the electrical quantities at fundamental frequency only. Thus, the fundamental frequency phasors are directly used in the analysis of FCG's short-circuit model below. In the derivation, the control signals in the rotating reference frame are expressed in uppercase format, since they are mainly DC components when the control system enters the steady state.

Referring to Figure 2-2, the positive and negative sequence current phasors of FCG during asymmetrical grid faults meet [100],

$$\dot{I}_{1g} = \left(I''_{d1g} + j \cdot I''_{q1g}\right) \cdot \exp\left[j \cdot angle\left(\dot{V}_{1g}\right)\right] \tag{2.5}$$

$$\dot{I}_{2g} = \left(I''_{d2g} + j \cdot I''_{q2g}\right) \cdot \exp\left[j \cdot angle\left(\dot{V}_{2g}\right)\right] \tag{2.6}$$

where $\dot{I}_g$ and $\dot{V}_g$ are the phasor representations of sequence components i_g and v_g, and I''_{dqg} denote the steady-state current references i''_{dq} [100]. As given in (2.7) and (2.8), the active/reactive current references I''_{dqg} are the revised quantities of the current references I'_{dqg} specified by grid codes. I_g^{lim} and I_{qg}^{lim} are the upper limits of the PEC current and the one in the $q-axis$.

$$\begin{cases} I''_{q1g} = min\left(I'_{q1g}, \dfrac{I'_{q1g}}{M}\right) \\ I''_{q2g} = \min\left(I'_{q2g}, \dfrac{I'_{q2g}}{M}\right) \end{cases}, M = \frac{\left|I'_{q1g}\right| + \left|I'_{q2g}\right|}{I_{qg}^{lim}} \tag{2.7}$$

$$\begin{cases} I''_{d1g} = min\left(I'_{d1g}, \sqrt{\left(I_g^{lim}\right)^2 - \left(\left|I''_{q1g}\right| + \left|I''_{q2g}\right|\right)^2} \right) \\ I''_{d2g} = 0 \end{cases} \tag{2.8}$$

During the LVRT period, the PEC controller gives priority to the reactive current output to support the voltage recovery at the PCC terminal. Then, the rest capacity of PEC is used for the active power transfer [52]. According to the reactive current supporting rules of FCG for grid connection in Figure 2-3, I'_{qg} in the positive and negative sequence systems respectively meet (2.9) and (2.10) [100],

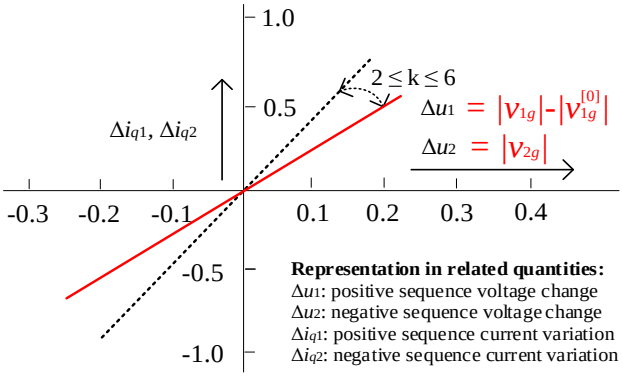

Figure 2-3 Reactive current supporting rules of FCG during voltage sags (swells) [99]

$$I'_{q1g} = -K_{V1}\left(1 - \left|\dot{V}_{1g}\right|\right) \tag{2.9}$$

$$I'_{q2g} = K_{V2}\left|\dot{V}_{2g}\right| \tag{2.10}$$

$$I'_{d1g} = \frac{P_{in}}{\left|V_{d1g}\right|} \tag{2.11}$$

In (2.9) and (2.10), K_{V1} and K_{V2} are the proportional gains of the positive and negative components. In (2.11), P_{in} is the pre-fault active power input from the DC side, which is assumed constant during grid faults [52]. Besides, I''_{d2g} remains 0, as active power generation in the negative sequence system is undesired from the FCG side [100].

From (2.7)-(2.11), the current phasors of FCG in (2.5) and (2.6) are revised as,

$$\dot{I}_{1g} = \dot{I}_{source} - Y_{1FCG} \cdot \dot{V}_{1g} \tag{2.12}$$

$$\dot{I}_{2g} = Y_{2FCG} \cdot \dot{V}_{2g} \tag{2.13}$$

where $\dot{I}_{source}$ and Y_{1FCG} denote the equivalent current source and the admittance in positive sequence circuit, respectively. Y_{2FCG} represents the admittance in the negative sequence circuit.

$$\begin{cases} \dot{I}_{source} = \left(I''_{d1g} - j \cdot \dfrac{K_{V1}}{M'} \right) \cdot \exp\left[j \cdot angle\left(\dot{V}_{1g} \right) \right] \\ Y_{1FCG} = \dfrac{K_{V1}}{j \cdot M'} \quad , \quad Y_{2FCG} = j \cdot \dfrac{K_{V2}}{M'} \end{cases} , M' = max\left(1, M\right) \tag{2.14}$$

According to (2.12) and (2.13), the equivalent short-circuit models of FCG in the sequence systems can be expressed as Figure 2-4.

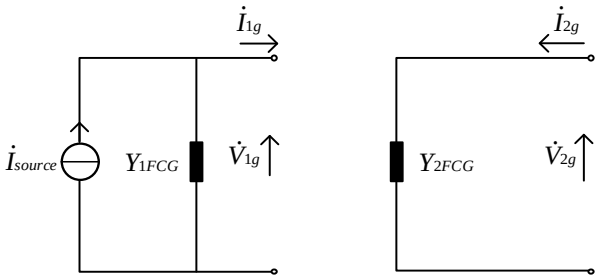

Figure 2-4 Equivalent models of FCG in the positive and negative sequence systems [100]

From Figure 2-2, one can see that the negative sequence currents in d and q $axises$ are purposively incorporated into the control loop under the DSC regulation method. According to whether the negative sequence control loop is enabled, PEC can run in different control strategies, including balanced current control (BCC) strategy and DSC strategy.

- In the presence of BCC strategy, only the positive sequence control loop regulates the PEC current output, regardless of the grid fault types. Thus, the PEC always outputs the balanced positive sequence current. Under such PEC control mode, the negative sequence circuit of FCG always stays in open-circuit condition.

- In contrast, the DSC strategy can meet the requirements of current regulation in either the positive sequence system or the negative one during asymmetrical grid fault conditions.

2.2. CHALLENGE ASSESSMENT OF THE TRADITIONAL NETWORK PROTECTIONS

In this section, the adaptability of the conventional line current differential protection and distance protection is assessed in the power networks connecting FCGs.

2.2.1. LINE CURRENT DIFFERENTIAL PROTECTION

A. Differential protection principle

Figure 2-5 is used to illustrate the differential principle in a transmission line, which can be intuitively represented as the differential current of (2.15),

$$I_{diff} = \left| \dot{I}_s + \dot{I}_r \right| \tag{2.15}$$

where $\dot{I}_s$ and $\dot{I}_r$ correspond to the phasor format of the time-domain (directional) currents in Figure 2-5.

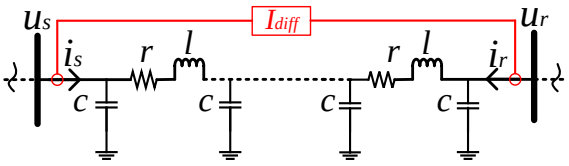

Figure 2-5 Distributed parameter line model

Besides the differential current (2.15), a restraining current is designed to enhance the security of differential protection in practical application. Generally, it is selected as a constant threshold or the difference of two-sided currents,

$$I_{res} = \left| \dot{I}_s - \dot{I}_r \right| \tag{2.16}$$

Take the line current differential relay with a percentage restraint characteristic, for example. The corresponding operation criterion is defined as [101],

$$\begin{cases} I_{diff} \geq I_{op[0]} \\ I_{diff} \geq k_{res} \cdot I_{res} \end{cases} \tag{2.17}$$

where $I_{op[0]}$ is the current threshold (for pickup function). k_{res} represents the restraining coefficient [102]. A typical selection of k_{res} in the system connecting wind parks is 0.8 [72].

B. Protective challenge analysis

To investigate the performance of the conventional 87L, the test system connecting the FCG-based plant in Figure 2-6 is modeled in DIgSILENT/PowerFactory [103]. The rated power of the FCG-based plant is initialized as 240 MW. SG represents the system slack node. Line L_{2-3} is the protective zone of the 87L element. System runs at 50 Hz and 400 kV. Table A-1 given in Appendix A lists the system parameters in detail.

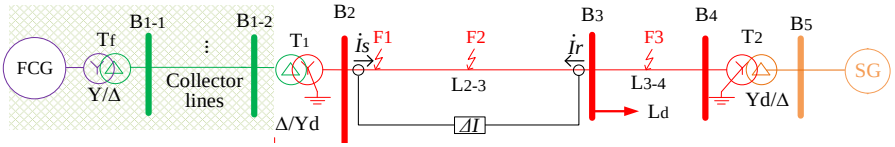

Figure 2-6 400kV test system model [103]

As mentioned in [72, 102-103], the high penetration of FCGs in the transmission network may reduce the sensitivity of 87L when FCGs operate in BCC strategy. Meanwhile, the sensitivity issue mainly occurs during L-L faults. Table 2-1 compares the current components sensed by 87L during different internal faults. In the table, one can see the evident difference between the two-sided current components during L-L faults.

TABLE 2-1 COMPARISON OF CURRENTS SENSED BY 87L DURING DIFFERENCE INTERNAL FAULTS

Fault Type	**FCG-based plant side**	**Main grid side**
L-L fault	Only positive sequence current	Positive & negative sequence currents
L-G fault	Zero-sequence current dominated	
L-L-G fault		
3PH fault	Positive sequence current	

In this section, the influence of various fault control requirements from different grid codes on the 87L is further investigated.

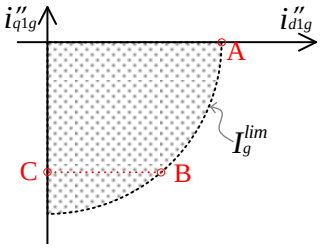

Figure 2-7 Vector diagram of the positive sequence current references in the rotating reference frame [103]

Figure 2-7 depicts the vector diagram of positive sequence current references in the rotating reference frame, where the dotted area represents the possible operation zone during grid faults. The dashed arc denotes the operation trajectory where the output current has maximum magnitude, i.e. I_g^{lim}. To see the effects of different fault controls, three fault control modes of FCG are selected for the comparison purpose, as points A, B, and C shown in Figure 2-7 [103].

1) Fault control mode A: FCG outputs maximum positive sequence active current.
2) Fault control mode B: FCG first provides the positive sequence reactive current according to the grid code [99], referring to (2.9) (set the positive sequence control gain $K_{V1} = 2$); By then, the rest capacity of FCG works for the transfer of positive sequence active current.
3) Fault control mode C: FCG only provides the same amount of positive sequence reactive current as point B.

Considering a bolted L-L fault BC on the line L_{2-3}, one can build the current equation in the healthy phase A (As shown in Figure 2-6, the branch orientation is assumed positive for current) [102],

$$\dot{I}_{sa} + \dot{I}_{ra} + \dot{I}_{cap.aa} - \dot{I}_{cap.ac} - \dot{I}_{cap.ab} = 0 \tag{2.18}$$

where $\dot{I}_{sa}$ and $\dot{I}_{ra}$ represent the currents at FCG-based plant and SG sides, respectively. $\dot{I}_{cap.aa}$ represents the self-capacitive current in the healthy phase, while $\dot{I}_{cap.ac}$ and $\dot{I}_{cap.ab}$ represent the mutual capacitive currents in between the faulty and the healthy phase(s) [102].

Since zero sequence current is absent during L-L fault BC, the currents at the SG side meet $\dot{I}_{ra} + \dot{I}_{rb} + \dot{I}_{rc} = 0$. When the line capacitive current is ignored, (2.18) can be simplified as [102],

$$\dot{I}_{rb} + \dot{I}_{rc} = \dot{I}_{sa} \tag{2.19}$$

To analyze the effects of different fault control modes of FCG on 87L, it is first assumed that the FCG-based plant is at a low penetration level. Under this circumstance, one may think that the angular difference at SG side between $\dot{I}_{rb}$ and $\dot{I}_{rc}$ approaches 180°, as $\dot{I}_{sa}$ being small in magnitude. On the complex plane, $\dot{I}_{rb}$ is assumed locating in the horizontal positive direction, then the phasor representations of $\dot{I}_{rb}$ and $\dot{I}_{rc}$ (dashed phasors) are first displayed in Figure 2-8. Under the fault control mode C, if one considers the following two aspects:

1) There is no active power transfer on the line;
2) Network loss is ignored.

the current phasors at the FCG-based plant side can be then positioned with respect to those of the SG side, as the red-marked phasors in Figure 2-8. Since the angular difference of $\dot{I}_{sb}$ to $\dot{I}_{sc}$ at FCG-based plant side stays at 120º due to the balanced current control, the angular difference between $\dot{I}_{rb}$ and $\dot{I}_{sb}$ (or $\dot{I}_{rc}$ and $\dot{I}_{sc}$) approaches 30° at the moment. Thus, $I_{diff} > I_{res}$ is valid in both phases B and C.

Subsequently, the fault control mode A is considered. As depicted in Figure 2-7, the current reference vector rotates 90° in the counterclockwise direction when compared with the one under the fault control mode C. For simplicity, it is assumed that the voltage phase angle has no shift due to the fault control variation from mode C to A. One can infer that the FCG current will rotate at the same angle in the counterclockwise direction, as the green-marked phasor position in Figure 2-8. Under this circumstance, the angular difference between $\dot{I}_{rc}$ and $\dot{I}_{sc}$ approaches 120º, while it is around 60º for the one between $\dot{I}_{rb}$ and $\dot{I}_{sb}$. In other words, $I_{diff} > I_{res}$ is valid in phase B, however, it meets $I_{diff} < I_{res}$ in phase C. It proves that the differential relay in phase C probably faces poor sensitivity. In addition, the differential relay in phase C may also have a similar sensitivity issue under the fault control mode B. It will happen when the counterclockwise rotation of FCG currents relative to the ones under fault control mode C is larger than 60°, as the blue-marked phasor position in Figure 2-8.

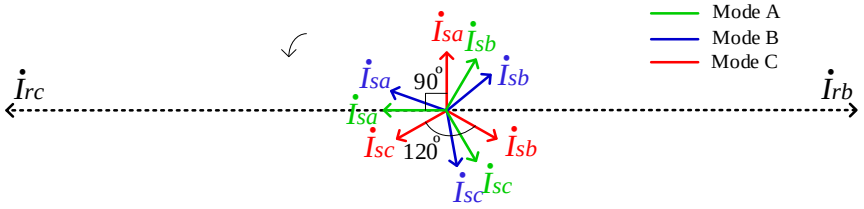

Figure 2-8 Current phasor representation, in the case of FCG-based plant at low penetration level

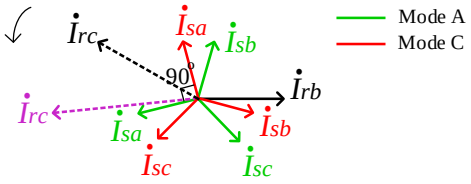

Figure 2-9 Current phasor representation, in the case of FCG-based plant at high penetration level

When the FCG-based plant is at a high penetration level, the angular difference between $\dot{I}_{rb}$ and $\dot{I}_{rc}$ at SG side is no longer 180°, due to the evident magnitude of $\dot{I}_{sa}$. On the complex plane, $\dot{I}_{rc}$ and $\dot{I}_{sa}$ will be on the same half-plane when $\dot{I}_{rb}$ is remained in the positive horizontal direction, referring to (2.19). For certain fault conditions of the fault control mode C, if $\dot{I}_{rb}$ is ahead of $\dot{I}_{sb}$ in an angle less than 30°, the $\dot{I}_{sa}$ under fault control mode A and the new $\dot{I}_{rc}$ (marked in purple) will locate on the below half-plane, as depicted in Figure 2-9. Under such circumstance, the angular difference of

$\dot{I}_{rc}$ to $\dot{I}_{sc}$ even exceeds 120º. It indicates that the differential relay in phase C probably performs worse sensitivity under the high penetration condition.

As control mode B falls in between the control modes C and A, the sensitivity of differential relay in phase C may also be threatened under some fault conditions, which is not discussed here in detail.

C. Simulation verification

Scenario 1: A bolted L-L fault BC located at point *F*1 (10 km away from FCG-based plant) is tested to verify the above analysis. The capacity of SG is initialized as 500 MVA. The complex plane representations of the relay's secondary currents under different fault control modes are displayed in Figure 2-10 (Current transformer (CT) ratio equals 1000:1). In the figure, the rotation of FCG currents accords with the above theoretical analysis when the fault control of FCG moves from mode C to mode B then to mode A.

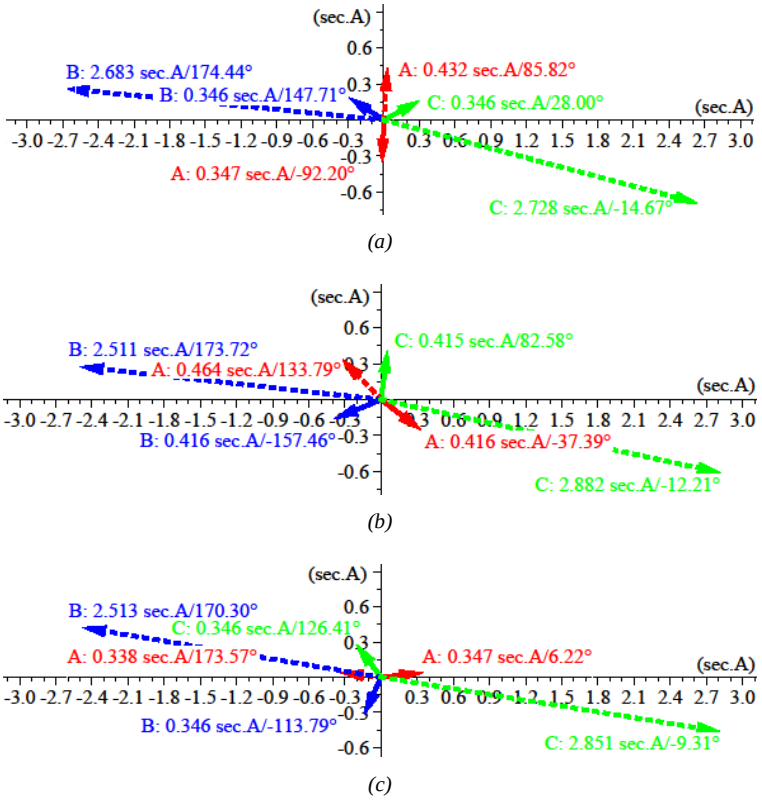

Figure 2-10 Complex plane representations of relay's secondary currents, the capacity ratio of SG to FCGs being 500 MVA:240 MW. (solid arrow: FCG side; dashed arrow: SG side) (a) Fault control mode C (b) Fault control mode B (c) Fault control mode A [103]

Keeping the FCG-based plant at 240 MW while adjusting the capacity of SG from 500 MVA → 360 MVA → 240 MVA → 120 MVA → 60 MVA, the power system connecting the FCG-based plant with different penetration conditions are compared.

For the same bolted fault BC located at $F1$, Table 2-2 lists the angular differences of steady-state fault currents, as well as the ratios of I_{diff} to $(k_{res}I_{res})$. According to the criterion in (2.17), the current ratio of I_{diff} to $(k_{res}I_{res})$ will be larger than 1 if internal faults occur.

From Table 2-2, one can see that the angular differences θ_{r-s} in phase C increase a lot when the fault control of FCG moves from mode C to mode B then to mode A. It indicates that mode A is most prone to relay malfunction, and it is true for any column in Table 2-2 with different capacity ratios of SG to FCG-based plant. From the row under fault control mode A in Table 2-2, one may find that the angular differences θ_{r-s} in phase B are all within 90°, i.e. $I_{diff} > I_{res}$. Meanwhile, θ_{r-s} in phase C are all much larger than 90°, i.e. $I_{diff} < I_{res}$. Combining the results of current ratio $I_{diff}/(k_{res}I_{res})$, one can infer that the differential relay in phase C probably has reliability issue due to the poor sensitivity.

TABLE 2-2 ANGULAR DIFFERENCE OF FAULTY PHASE CURRENTS AND CURRENT RATIO [103]

Parameter \ Capacity ratio of SG to FCG			Column 1 500:240	Column 2 360:240	Column 3 240:240	Column 4 120:240	Column 5 60:240
Fault control mode A	Ph-B	θ_{r-s}	75.91°	76.73°	77.98°	81.13°	87.71°
		$\frac{I_{diff}}{k_{res}I_{res}}$	1.3394	1.353	1.3756	1.425	1.3984
	Ph-C	θ_{r-s}	135.72°	136.34°	137.19°	138.82°	140.68°
		$\frac{I_{diff}}{k_{res}I_{res}}$	1.0577	1.0266	0.9747	0.844	0.6644
Fault control mode B	Ph-B	θ_{r-s}	28.82°	29.02°	29.23°	29.22°	27.17°
		$\frac{I_{diff}}{k_{res}I_{res}}$	1.659	1.755	1.948	2.751	5.206
	Ph-C	θ_{r-s}	94.79°	95.98°	97.93°	102.97°	110.7°
		$\frac{I_{diff}}{k_{res}I_{res}}$	1.221	1.209	1.185	1.103	0.947
Fault control mode C	Ph-B	θ_{r-s}	26.73°	27.02°	27.73°	30.64°	36.89°
		$\frac{I_{diff}}{k_{res}I_{res}}$	1.578	1.644	1.7469	2.148	2.954
	Ph-C	θ_{r-s}	42.67°	44.1°	46.47°	52.82°	64.49°
		$\frac{I_{diff}}{k_{res}I_{res}}$	1.489	1.528	1.6568	1.732	1.786

Take the fault scenarios in columns 3~5 of mode A, for example. The dynamic ratios $I_{diff}/(k_{res}I_{res})$ sensed by 87L in phases B and C for these three faults are plotted in Figure 2-11. It can be seen that the differential relay in phase C even fails to clear these internal faults (fault occurs at 0.1 s).

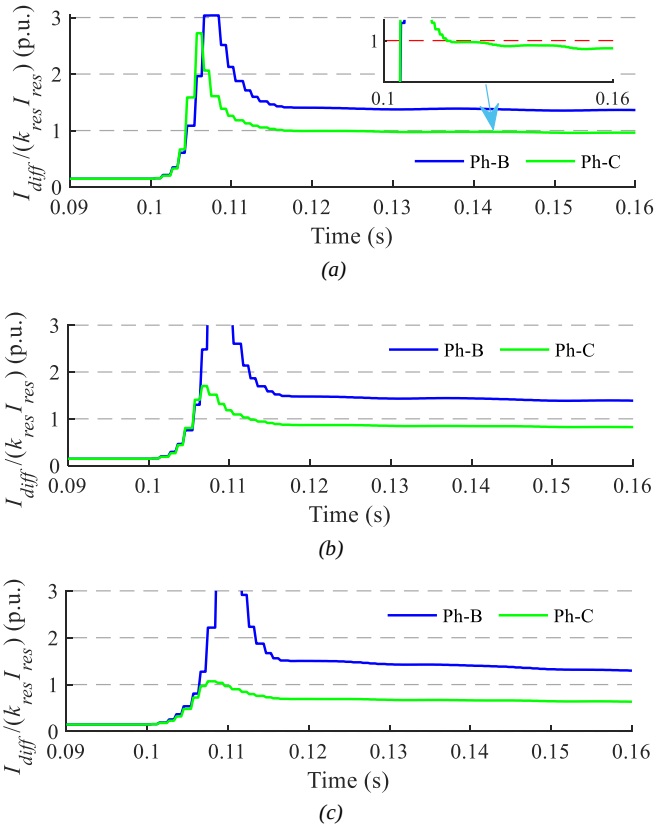

Figure 2-11 Dynamic current ratios $I_{diff}/(k_{res}I_{res})$ under the FCG fault control mode A considering different capacity ratios of SG to FCG. (a) 240:240 MW (b) 120:240 MW (c) 60:240 MW

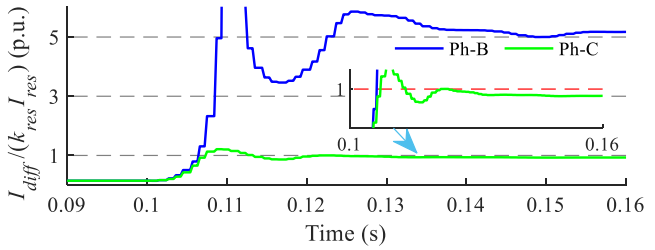

Figure 2-12 Dynamic current ratios $I_{diff}/(k_{res}I_{res})$ sensed by 87L under the FCG fault control mode B, with the capacity ratio of SG to FCG equaling 60:240 MW

Under mode B, θ_{r-s} either in fault phase B or in phase C clearly decrease, however, they are still larger than 90° in phase C ($I_{diff} < I_{res}$), as listed in Table 2-2. Referring to the current ratios $I_{diff}/(k_{res}I_{res})$, it can be seen that the differential relay in phase C also performs a poor sensitivity. Taking the fault scenario in column 5 as an example, the dynamic ratios $I_{diff}/(k_{res}I_{res})$ sensed by 87L in phases B and C are plotted in Figure 2-12. From the figure, one can see that the differential relay in phase C will also refuse to trip the fault.

As a comparison, the fault scenarios in Figure 2-11 (c) and Figure 2-12 are re-tested, considering the resistive fault condition of $R_f = 20\Omega$. From Figure 2-13, one can see that the differential relay in phase C shows similar reliability issues and will fail to clear these internal faults. This indicates that the potential sensitivity and reliability issues of differential relay during L-L fault has no relationship with the fault resistance.

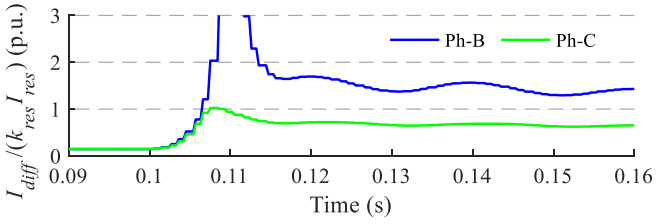

(a)

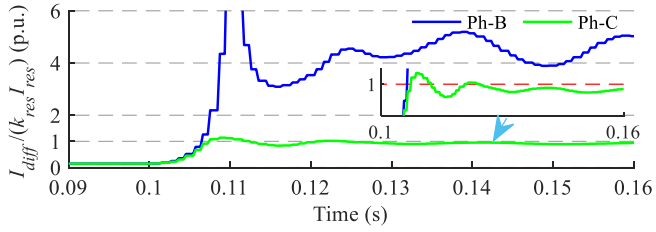

(b)

Figure 2-13 Dynamic current ratios $I_{diff}/(k_{res}I_{res})$ sensed by 87L during resistive faults, with the capacity ratio of SG to FCG equaling 60:240 MW. (a) Fault control mode A (b) Fault control mode B

From the above comparison in Figure 2-11, one can also conclude that the sensitivity of differential relay tends to reduce when the penetration of FCG-based plant increases. This can further cause the reliability issue.

In contrast, one may see that the differential relays both in phases B and C will perform good sensitivity under the fault control mode C (Table 2-2).

Scenario 2: In the above scenario study, the BCC strategy is adopted in the FCG-based plant during grid faults. As far as the LVRT requirements in Denmark are concerned, one can think that FCGs operate under fault control mode B. As mentioned in section 2.1.2, the DSC strategy is a promising solution for PECs during asymmetrical grid faults. The injection of negative sequence reactive current from FCG-based plant can help to reduce the imbalance of the system voltage.

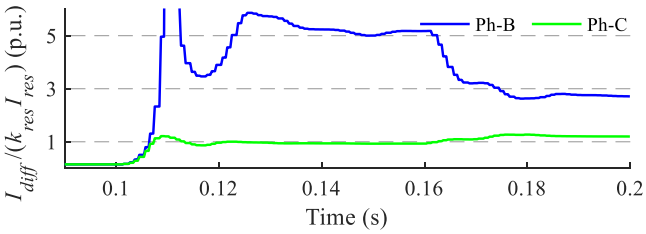

Figure 2-14 Dynamic current ratios $I_{diff}/(k_{res}I_{res})$ under the FCG fault control mode B with negative sequence current injection

By activating the negative sequence control loop at 0.16 s (setting the negative sequence control gain in (2.10) as $K_{V2} = 2$), the L-L fault BC studied in Figure 2-12 is re-tested to examine the effects of negative sequence control loop.

From the simulation results shown in Figure 2-14, one can see that the differential relay in phase C cannot work correctly at the initial fault period (before 0.16 s) under the BCC strategy. However, the injection of negative sequence current after 0.16 s improves the sensitivity of the differential relay in phase C to a certain degree [103].

2.2.2. DISTANCE PROTECTION

A. Distance protection principle and protective challenge analysis

The modeling analysis in section 2.1.2 shows that the fault current generation of FCGs is fully determined by the PEC fault control. The sensitivity issue of differential protection resulting from the PEC fault controls has been analyzed in section 2.2.1. Similarly, the challenges of distance protection are further investigated in this section.

As reported in [104], during resistive grid faults, the distance relay installed at the power sending terminal faces the risk of relay over-reach in the conventional SG-dominated power grid with a remote in-feed. This is because of the transmission angle for the real power transfer across the line, which in turn causes the angular difference of the two-sided currents. This issue becomes even severer for the distance relay installed at terminals of a power transmission grid connecting FCGs [105]. Because the real power output from FCGs is adjustable according to the active power transfer requirement during fault conditions in various Grid Codes.

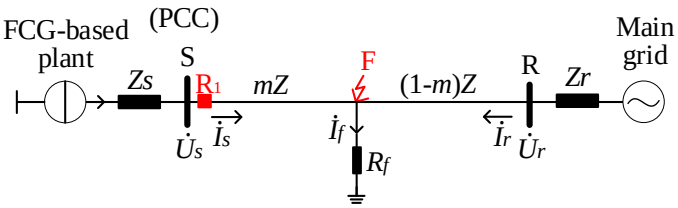

Figure 2-15 Single-line diagram of the fault network

Figure 2-15 displays the single-line fault model of the transmission system connecting FCG-based plant, where FCGs operate in the current source mode. ($\dot{U}_s$, $\dot{I}_s$) and ($\dot{U}_r$, $\dot{I}_r$) are respectively the terminal voltage and the terminal current (flowing into line) at terminals S and R. Z_r, Z_s, and Z are the impedance of main grid, FCG system, and transmission line. $\dot{I}_f$, R_f, and m are the fault current, fault resistance, and fault distance in per unit length.

The apparent impedance seen by the distance relay R_1 can be expressed as [105],

$$Z_{app} = \frac{\dot{U}_s}{\dot{I}_s} = mZ_1 + \underbrace{R_f \cdot \left(1 + \frac{\dot{I}_r}{\dot{I}_s}\right)}_{virtual\_increment} \tag{2.20}$$

In (2.20), the fault resistance R_f causes a 'virtual' increment in the apparent impedance, i.e. $(1 + \frac{\dot{I}_r}{\dot{I}_s})R_f$. Actually, the 'virtual' resistance $real\left(1 + \frac{\dot{I}_r}{\dot{I}_s}\right)R_f$ leads to

the right-shift of the apparent impedance only. As shown in Figure 2-16, this influence can be avoided by adjusting the right-sided bounder of distance relay [105].

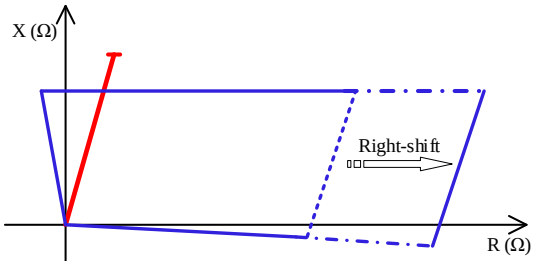

Figure 2-16 Distance relay with polygonal boundary

However, the 'virtual' reactance $imaginary\left(1+\frac{\dot{I}_r}{\dot{I}_s}\right)R_f$ will produce the error in X-direction due to the angular difference between $\dot{I}_r$ and $\dot{I}_s$. In theory, the apparent impedance of the distance relay at FCG-based plant side can be either tilted up or down [105]. Because the Grid Codes from different countries follow different regulation requirements during grid faults [31, 106].

B. Simulation verification

To investigate the effects of different fault regulation requirements on distance protection, the 110 kV test system connecting FCG-based plant in Figure 2-17 is adopted, where FCG operates under the BCC strategy. Detailed system parameters of the test model can be found in Table A-2 in Appendix A. In this section, zone 1 of distance protection is assumed to cover 80% of line length. Both the L-L fault BC and L-G fault AG are tested to elaborate the effects of impedance tilt. In the following test scenarios, two boundary conditions of fault control, i.e. pure reactive current output and pure active current output, are considered. And, an internal fault position is considered under the former control boundary to see the relay malfunction risks, while an external for the later one.

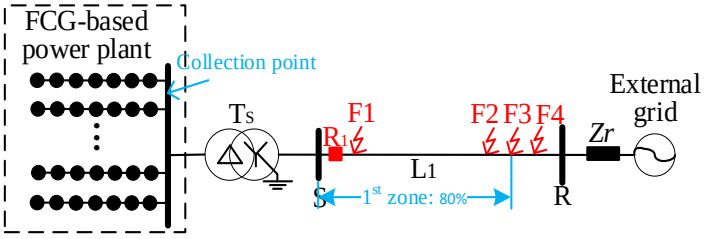

Figure 2-17 Single-generator infinite test system of FCG-based plant [100]

Figure 2-18 shows the trajectories of the relay's apparent impedance with the increase of fault resistance during an L-L fault BC. In Figure 2-18 (a), the internal fault locates at point F2, 70% line length apart from terminal S. It can be seen that the relay tends to under-reach for resistive grid faults, when FCG operates under the control mode of pure reactive current output.

Correspondingly, the external fault located at point F4, 90% line length apart from terminal S, is further tested when FCG runs under the control mode of pure active current output, as shown in Figure 2-18 (b). Clearly, the relay tends to over-reach during resistive faults under this control mode.

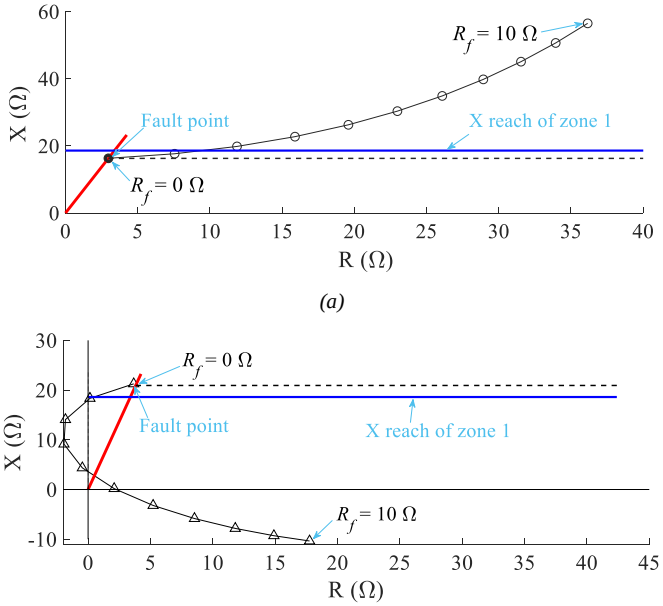

Figure 2-18 Influence of the fault resistance during L-L fault BC (R_f per step increment 1 Ω) (a) Pure reactive current output (b) Pure active current output

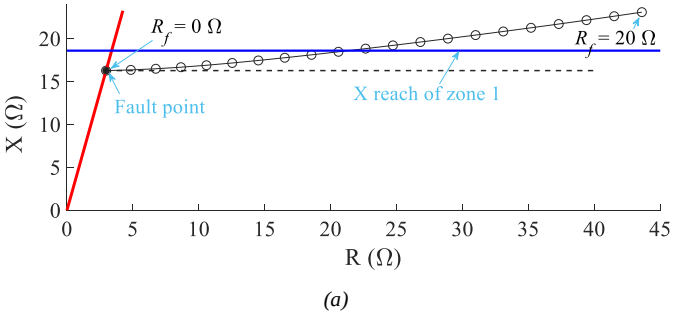

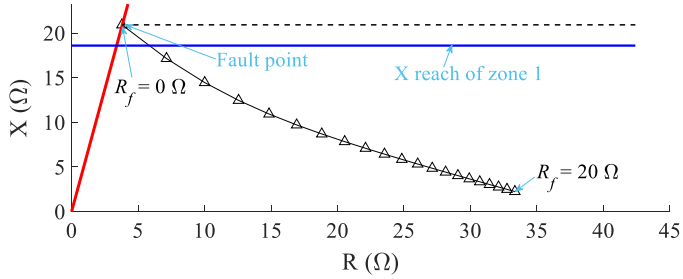

(b)

Figure 2-19 Influence of the fault resistance during L-G fault AG (R_f per step increment 1 Ω) (a) Pure reactive current output (b) Pure active current output

Meanwhile, the above over- or under-reaching issue becomes worse for a fault scenario with larger fault resistance [105]. The above trends are also true for the L-G fault AG studied in Figure 2-19. In addition, one can see that the relay over- or under-reach under the L-G fault is slighter than the L-L fault situation. This benefits from the evident zero-sequence current during a L-G fault [105].

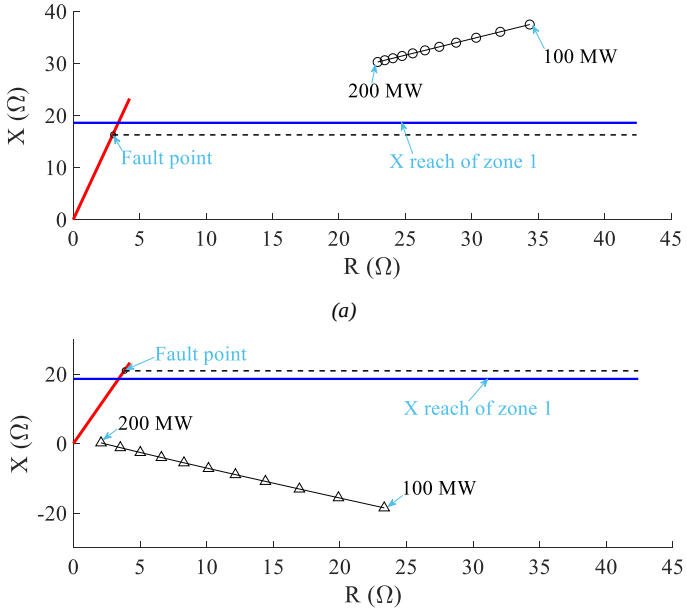

(a)

(b)

Figure 2-20 Influence of the FCG penetration level during L-L fault BC (FCG per step decrement 10 MW) (a) Pure reactive current output (b) Pure active current output

On the other hand, the influence of the FCG penetration level on distance protection is tested. The trajectories of relay's apparent impedance for the L-L fault BC (R_f =

5 Ω) are displayed in Figure 2-20. In the figure, the relay under-reach (or over-reach) corresponding to the FCG control mode of pure reactive current output (or pure active current output) becomes worse with the decrease of FCG capacity [105]. This trend accords with the feature of current in magnitude during L-L fault BC.

In detail, the virtual increment in (2.20) should be revised as $R_f(1+\frac{\dot{I}_{rbc}}{\dot{I}_{sbc}})$ for L-L fault BC. With the decrease of FCG capacity, the magnitude $\left|1+\frac{\dot{I}_{rbc}}{\dot{I}_{sbc}}\right|$ will increase, which evidently enlarges the error of reactance measurement [105]. It should be mentioned that the influence of the FCG capacity on the distance protection during L-G faults is different.

For the L-G fault AG in Figure 2-21, the virtual increment in (2.20) should be revised as $R_f(\frac{\dot{I}_f}{\dot{I}_{sa}+k_0\dot{I}_{0s}})$. When the FCG capacity decreases, the angular difference between $\dot{I}_f$ and $\dot{I}_{sa}+k_0\dot{I}_{0s}$ will decrease too. This leads to the reduced error of reactance measurement.

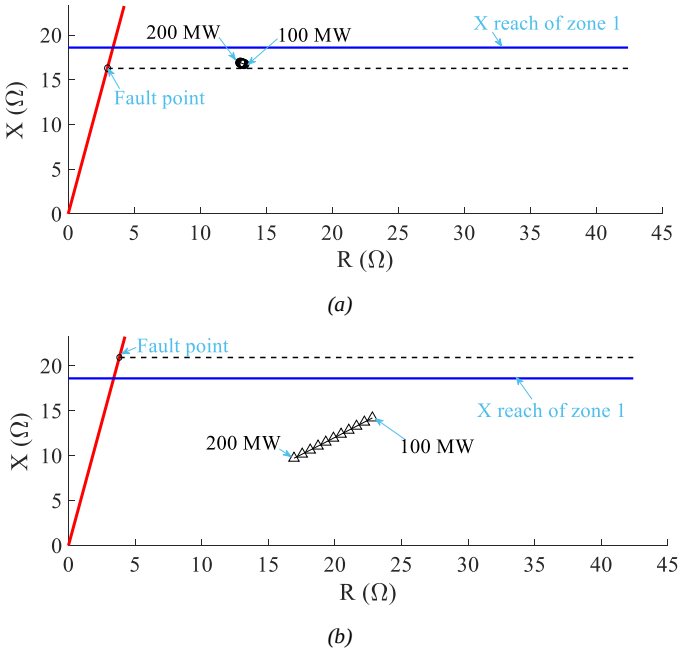

Figure 2-21 Influence of the FCG penetration level during L-G fault AG (FCG per step decrement 10 MW) (a) Pure reactive current output (b) Pure active current output

2.2.3. MESHED NETWORK CONFIGURATION

Meshed connection of the transmission grid is commonly deployed to maintain the reliability of power supply. The performance of both the line current differential protection and the distance protection in a meshed network is further elaborated in this section.

A. Line current differential protection

Actually, the sensitivity problem of the 87L phase element during L-L grid faults mentioned in section 2.2.1 is insignificant in a meshed network. This is because the extra path between the two-sided terminals of protected line can help to balance the angular difference of fault currents sensed by relay.

Take the same fault case studied in Figure 2-11 (c), for example. The performance of 87L deployed in the following two kinds of system configurations are compared.

Configuration 1: The system shown in Figure 2-6;

Configuration 2: A new transmission link between terminals B2 and B4 of the system in Figure 2-6 is added to simulate a meshed system condition. (Here, a 30 km line is considered for test purpose only)

Comparing the angular differences θ_{r-s} in phases B and C given in Figure 2-22 (a) and (b), one can see that θ_{r-s} in phase C is much larger than 90° under configuration 1. However, both the θ_{r-s} in phases B and C stay within 90° under configuration 2. It indicates that the relay sensitivity problem happening in configuration 1 may disappear in meshed configuration 2. This can be further seen from the comparison of the dynamic current ratios of I_{diff} to $k_{res}I_{res}$ in Figure 2-22 (c) with those in Figure 2-11 (c). In Figure 2-21 (c), both the current ratios I_{diff} to $k_{res}I_{res}$ in phases B and C are larger than 1, which meet the criterion (2.17). And, the internal fault can be tripped correctly.

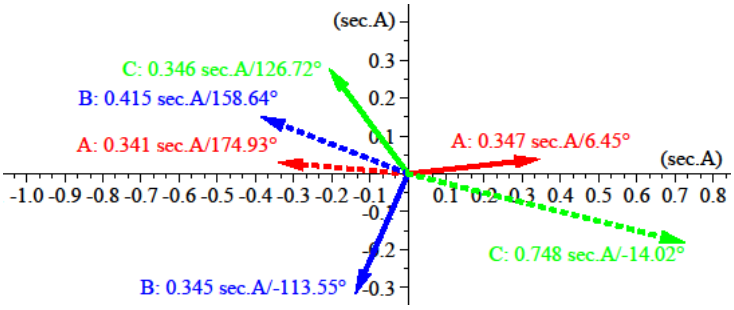

(a)

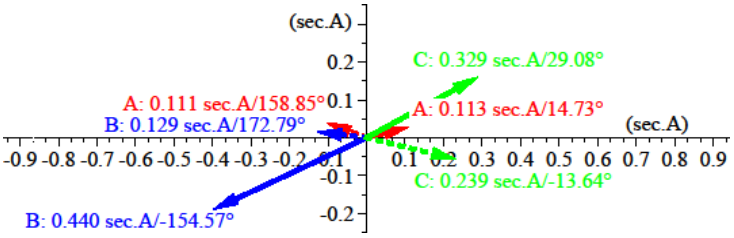

(b)

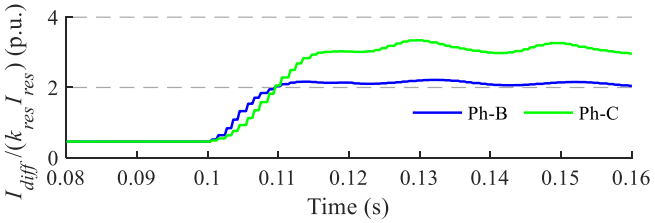

(c)

Figure 2-22 FCG operates in control mode A during a bolted L-L fault BC (10 km far from B2), with the capacity ratio of SG to FCG equaling 60:240 MW. (a) Configuration 1 (b) Configuration 2 (c) Dynamic current ratios $I_{diff}/(k_{res}I_{res})$ sensed by 87L

B. Distance protection

Similarly, the over- or under-reaching issue of the distance relay during resistive grid faults discussed in section 2.2.2 will be weakened in a meshed network due to the decrease of angular difference between $\dot{I}_r$ and $\dot{I}_s$, either.

As displayed in Figure 2-23, the test system of Figure 2-17 is reconfigured with extra links between terminals S and R. The line between terminals S and M is 20 km and the one between terminals R and M is 10 km (for test purpose only). The rated power of the load is 20 MW.

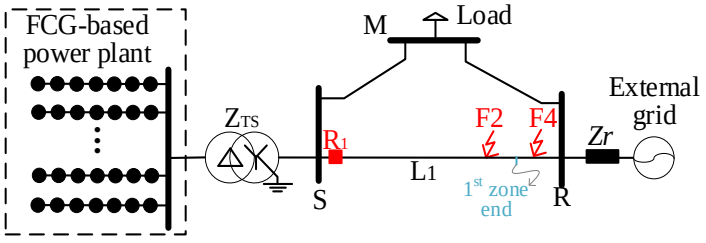

Figure 2-23 Meshed test system

In the reconfigured test system, the same L-L fault BC scenarios in Figure 2-18 are tested again, and the simulation results are displayed in Figure 2-24. Compared to Figure 2-18 (a), one can see that the under-reaching tendency of distance relay during the same fault condition is evidently reduced in the meshed system, as shown in Figure 2-24 (a). This also applies to the under-reaching tendency displayed in Figure 2-24 (b).

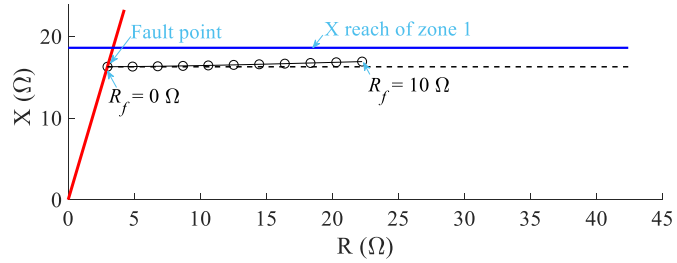

(a)

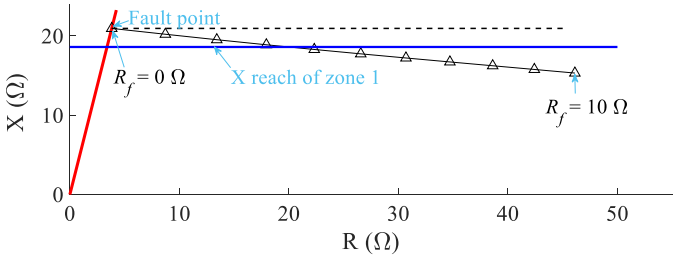

(b)

Figure 2-24 Influence of the fault resistance during L-L fault BC in meshed network (R_f per step increment 1 Ω) (a) Pure reactive current output (b) Pure active current output

2.3. SUMMARY

A. Current differential protection

In section 2.2.1, the 87L deployed in the power network connecting the FCG-based plant is assessed. From the tested fault scenarios when FCG operates in the BCC strategy,

1) For L-L faults, since only positive sequence current exists in the high voltage system at FCG-based plant side, the current differential relay is prone to malfunction due to the reduced sensitivity (regardless of the fault resistance condition).
2) The higher the FCG penetration level is, the higher the above malfunction risk of differential protection is [102].
3) The fault control mode of FCG heavily affects the performance of differential protection [103]. During a L-L fault, appropriate reduction of the active power transfer from FCGs whilst preserving the existing Grid Codes for reactive power supports can improve the sensitivity of differential protection.
4) The injection of negative sequence reactive current during the L-L fault does good to alleviate the sensitivity problem of differential protection [103], as the proportion of active current in the total fault current tends to decrease under such FCG fault control condition.

Limitation statement:

In this chapter, the magnitude comparison-based current differential protection is taken as an example for assessment. In fact, in terms of the differential current comparison, there are other methods, e.g. phase comparison, phasor comparison, and charge comparison, etc., that are also popular but not evaluated here.

B. Distance protection

The impacts of different FCG fault controls on the impedance element of distance protection are elaborated in section 2.2.2. In summary,

1) The relay over- or under-reach generally relies on the fault controls of PEC. Meanwhile, the larger the fault resistance is, the worse the over- or under-reaching problem is [105].
2) For L-L faults, the relay over- or under-reach becomes severe along with the decreasing capacity of local FCG-based plant. However, it performs an inverse trend during L-G faults [105].
3) The angular difference of the two-sided currents brings in the error of reactance measurement in distance protection [105]. An improved fault control considering

the proper active and reactive current output is one of the solutions to improve the reactance measuring accuracy of distance protection.

Limitation statement:

This chapter mainly focuses on the malfunction risk of impedance element in distance protection. And it is assumed that other functional elements, e.g. start unit, faulty phase selector, etc., can work properly.

C. Meshed system

The comparative studies in section 2.2.3 point out that the FCG control-caused relay sensitivity problem of 87L, as well as the over- or under-reaching problem of impedance element, are relatively slighter in a meshed system than those in a radial system.

CHAPTER 3. COMPENSATED CURRENT-BASED DIFFERENTIAL PROTECTION PRINCIPLE

Time-domain protections have strong transient adaptability and fast tripping ability, attracting a lot of attention. Reference [107] reports a line differential protection based on the instantaneous energy and synthetic reactive power. However, the influence of the diversity of PEC control strategies needs further assessment in the FCGs dominated power system. Another popular time-domain differential protection principle, the travelling wave-based protection method, is inherently unaffected by the NSG fault controls. But a very high sampling frequency is generally required. In [108], a modified travelling wave method achieves success in lower communication traffic at 250 kHz, remaining a challenge.

To systematically introduce the compensated current-based differential principle, this chapter is organized into three sections. Section 3.1 focuses on how to build the compensated current-based time-domain differential equation and the implementing method for fault detection. For reliability concerns, the restraining equation is designed to enhance the compensated current-based differential principle in section 3.2. Because the newly proposed time-domain differential principle in section 3.2 is on the premise of SG source, the corresponding revision is further elaborated for the particularity of FCG model during grid faults in section 3.3.

3.1. COMPENSATED CURRENT-BASED DIFFERENTIAL PRINCIPLE IN TIME-DOMAIN

As mentioned in section 2.2.1, the basic principle of 87L is the differential current equation (2.15), being rewritten as,

$$I_{diff} = \left| \dot{I}_s + \dot{I}_r \right| \tag{3.1}$$

This chapter focuses on the compensated current-based differential principle. Select one compensation point on the protected line in Figure 2-5, yielding Figure 3-1. From the figure, the new differential current equation is built as,

$$i_{diff} = i_s^* + i_r^* = f\left(u_s, i_s, x_s\right) + f\left(u_r, i_r, x_r\right) \tag{3.2}$$

where $i_s^* = f\left(u_s, i_s, x_s\right)$ and $i_r^* = f\left(u_r, i_r, x_r\right)$ are the compensated currents. For a homogeneous transmission line, they can be estimated by the Bergeron line model-based time-domain calculation method given in Appendix B.

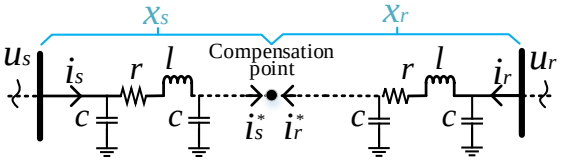

Figure 3-1 Distributed parameter line model

Compared to (3.1), one can see that the new differential current equation has essentially incorporated the influence of capacitive current.

3.1.1. MODEL MAPPING ANALYSIS OF DIFFERENTIAL EQUATION

Since the time-domain current and voltage change with the lapse of time, they manifest evident fluctuation (especially in the fault transient). The conventional current threshold-based comparison for fault detection performs the reliability issue. This section introduces the fault model mapping-based fault detection method.

To eliminate the influence of load current component, the time-domain differential current equation in (3.2) is re-declared in the fault component circuits of Figure 3-2. Here, a universal situation with an external grid (dashed blue link) in between the protected zone is considered. (R_s, L_s), (R_r, L_r), and (R_p, L_p) represent the equivalent impedance parameters of two-sided sources and the external grid.

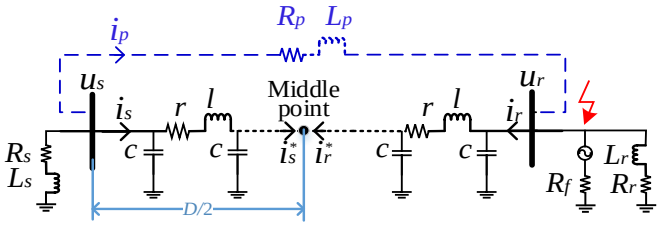

Figure 3-2 Fault component circuit during general external faults

Defining $i_{cd}(t)$ and $u_{cd}(t)$ as the differential variables in the fault component circuit of Figure 3-2 [109],

$$\begin{cases} i_{cd} = i_s + i_r \\ u_{cd} = u_s + u_r \end{cases} \tag{3.3}$$

Substituting (3.3) and (B.1) into (3.2), the differential equation is revised as [109],

$$\begin{aligned}&\frac{Z_c+rx/4}{2Z_c^2}\left[u_{cd}\left(t+\frac{x}{v}\right)-\left(Z_c+rx/4\right)i_{cd}\left(t+\frac{x}{v}\right)\right]-\\&\frac{Z_c-rx/4}{2Z_c^2}\left[u_{cd}\left(t-\frac{x}{v}\right)-\left(Z_c-rx/4\right)i_{cd}\left(t-\frac{x}{v}\right)\right]-\\&\frac{rx}{4Z_c^2}\left[u_{cd}\left(t\right)-\left(rx/4\right)i_{cd}\left(t\right)\right]=0\end{aligned} \tag{3.4}$$

where the midpoint in the line is selected as the compensation point. Note that, one need to adopt the interpolation method to estimate the differential voltages and currents $u_{cd}\left(t+\frac{x}{v}\right)$, $i_{cd}\left(t+\frac{x}{v}\right)$, $u_{cd}\left(t-\frac{x}{v}\right)$, and $i_{cd}\left(t-\frac{x}{v}\right)$. Because the required values at the point-in-time $(t\pm\frac{x}{v})$ do not always align to the sampling point [108].

Subsequently, one can see that the differential current equation (3.4) meets a complete mapping relationship with the external fault-based model of Figure 3-2 [109]. And, this mapping relationship is continuously valid regardless of the external grid link. However, it is not valid for an internal fault condition, since a new fault path is added in the protected zone, as illustrated in Figure 3-3 [109].

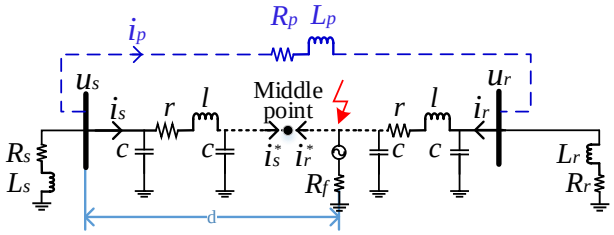

Figure 3-3 Fault component circuit during general internal faults [108]

To quantize the mapping relation of the differential current equation (3.4) with the fault status, the model mapping index is introduced as follows.

3.1.2. MODEL MAPPING INDEX AND CRITERION IMPLEMENTATION

A. Computation of model mapping index

Let [109],

$$\begin{cases} f_{diff}\left(t\right)=i_s^*\left(t\right) \\ g_{diff}\left(t\right)=i_r^*\left(t\right) \end{cases} \tag{3.5}$$

The relevant model mapping index (MMI) of (3.4) can be defined as [109],

$$MMI_{diff} = \frac{\int_0^T \left| f_{diff}(t) + g_{diff}(t) \right| dt}{\int_0^T \left(\left| f_{diff}(t) \right| + \left| g_{diff}(t) \right| \right) dt} \tag{3.6}$$

As discussed in [109], neglecting the error in the sampling/computation process and that of line parameters, $MMI_{diff} = 0$ is true for an external fault, since $i_s^*(t) + i_r^*(t) = 0$. However, $i_s^*(t)$ stays in-phase with $i_r^*(t)$ for an internal fault, so that $|i_s^*(t) + i_r^*(t)| = |i_s^*(t)| + |i_r^*(t)|$ is true at the moment, i.e. $MMI_{diff} = 1$. In practical, MMI_{diff} approaches 0 (or 1) only due to the influence of various errors. In this section, the threshold is initialized as 0.5, maintaining the maximum security margin on either internal or external faults [109]. The protection criterion of the proposed compensated current based differential principle can be expressed as [109],

$$MMI_{diff} > 0.5 \tag{3.7}$$

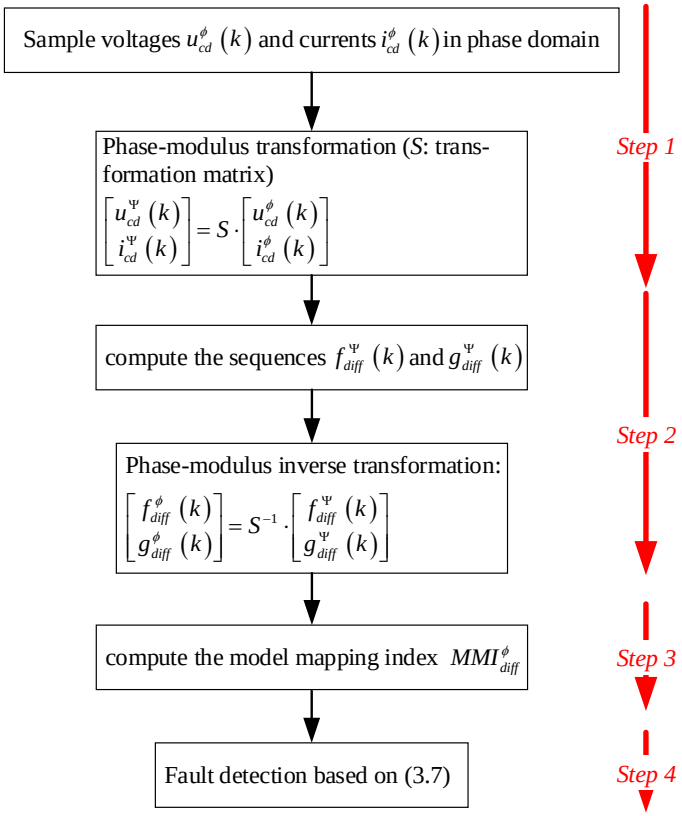

Figure 3-4 Implementing procedule of the MMI computation

B. Criterion implementation

To implement the protection criterion in a three-phase system, one needs first to compute the sequences $f_{diff}^{\psi}(k)$ and $g_{diff}^{\psi}(k)$ in three modulus circuits respectively (phase-modulus transformation is used in this process) [109]. Then, compound the sequences $f_{diff}^{\phi}(k)$ and $g_{diff}^{\phi}(k)$ in the three-phase system based on the inverse phase-modulus transformation and execute the MMI computation in separated phases [109]. Superscripts 'ϕ' and 'ψ' denote the phase components (phase a, b, c) and modulus components (modulus 0, 1, 2) respectively. As displayed in Figure 3-4, there are four steps to implement the criterion (3.7) in a three-phase system.

Once the model mapping index $MMI_{diff}^{\phi} > 0.5$ is satisfied, the fault occurs in the protected zone. Otherwise, it is out of the protected zone.

3.1.3. CASE STUDY

The feasibility of the proposed compensated current-based differential principle is tested in the 500 kV transmission system modeled in DIgSILENT/Power Factory, as illustrated in Figure 3-5. As shown in the figure, differential relays locate at the ends of protected line. (E_s, Z_s) and (E_r, Z_r) correspond to the power potentials and their source impedance, respectively. In addition, the fault points $F1$, $F2$, $F3$, and $F4$ are respectively 25 km, 50 km, 75 km, and 100 km apart from terminal B_s. Transmission line parameters are listed in Table A-3 in Appendix A.

A sampling frequency of 10 kHz is selected for fault recording. The data processing and protection criterion are implemented in Matlab. 20 ms data window is used to observe the dynamics of the proposed differential principle.

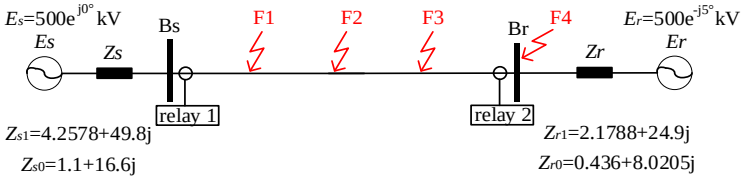

Figure 3-5 Simple test system with two side infeed [109]

Figure 3-6 displays the dynamic MMIs for four bolted faults, including the L-G fault AG at $F1$, the L-L-G fault BCG at $F2$, the 3PH fault ABC at $F3$, and the L-L fault BC at $F4$. Based on the discussion in section 3.1.2-A, one knows that the MMI(s) of the faulty phase(s) for an internal fault will have a larger magnitude than the threshold [109]. This can be seen from the three internal faults, cases 1~3, given in Figure 3-6. In these subplots, the MMIs of the faulty phases converge to the gray area above the

threshold, which represents the faulty region. On the contrary, the MMIs of the healthy phases keep smaller than the threshold in cases 1~3 [109]. So do the three phases for external faults. As illustrated in case 4 of Figure 3-6, all MMIs of the external fault gradually stabilize at the level below the threshold.

The tested faults in Figure 3-6 all occur at 0.2 s. In view of the speed performance, the dynamic MMIs in Figure 3-6 show fast convergence time, within 5~10 ms.

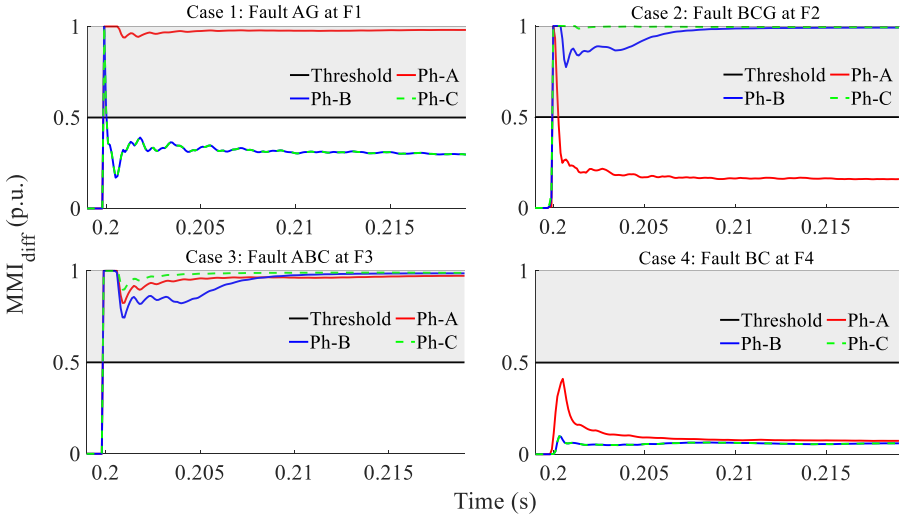

Figure 3-6 Dynamic MMIs for different bolted faults

TABLE 3-1 STEADY STATE MMIS OF DIFFERENT BOLTED FAULTS [109]

Fault condition	Model mapping index			
Location	*F*1	*F*2	*F*3	*F*4
L-G fault AG	Ph-A '+' Ph-B,C '-, -'	Ph-A '+' Ph-B,C '-, -'	Ph-A '+' Ph-B,C '-, -'	Ph-A,B,C '-, -, -'
L-L fault BC	Ph-B,C '+, +' Ph-A '-'	Ph-B,C '+, +' Ph-A '-'	Ph-B,C '+, +' Ph-A '-'	Ph-A,B,C '-, -, -'
L-L-G fault BCG	Ph-B,C '+, +' Ph-A '-'	Ph-B,C '+, +' Ph-A '-'	Ph-B,C '+, +' Ph-A '-'	Ph-A,B,C '-, -, -'
3PH fault ABC	Ph-A,B,C '+,+,+'	Ph-A,B,C '+,+,+'	Ph-A,B,C '+,+,+'	Ph-A,B,C '-, -, -'

* Note: '+' and '-' indicate larger than 0.5 and smaller than 0.5, respectively.

As listed in Table 3-1, one can see that the compensated current-based differential principle can reliably detect all the tested faults.

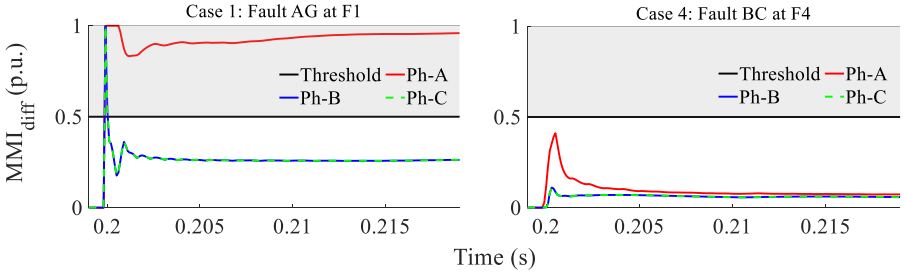

Figure 3-7 Dynamic MMIs for different high resistive faults

In addition, Figure 3-7 verifies the effects of fault resistance on the time-domain differential principle. In Figure 3-7, case 1 and case 4 studied in Figure 3-6 are re-tested under a high resistive fault condition, i.e. $R_f = 200\ \Omega$. Compared with the bolted fault conditions in Figure 3-6 (case 1 and case 4), one can see that the time-domain differential principle is slightly affected by the fault resistance.

Take different resistive L-G fault AG, for example. The compensated current-based differential principle is further investigated and the results are listed in Table 3-2.

TABLE 3-2 STEADY STATE MMIS OF DIFFERENT RESITIVE L-G FAULT AG [109]

Fault condition	Model mapping index			
Location	$F1$	$F2$	$F3$	$F4$
$R_f = 10\ \Omega$	Ph-A '+' Ph-B,C '-, -'	Ph-A '+' Ph-B,C '-, -'	Ph-A '+' Ph-B,C '-, -'	Ph-A,B,C '-, -, -'
$R_f = 100\ \Omega$	Ph-A '+' Ph-B,C '-, -'	Ph-A '+' Ph-B,C '-, -'	Ph-A '+' Ph-B,C '-, -'	Ph-A,B,C '-, -, -'

* Note: '+' and '-' indicate larger than 0.5 and smaller than 0.5, respectively.

Clearly, all the tested resistive faults in the above table are detected correctly. This is due to the fact that the model mapping relationships of the differential equation (3.4) with the fault component circuits in Figures 3-2 and 3-3 are definite, regardless of the magnitude of the fault resistance [109].

3.2. IMPROVED DIFFERENTIAL PRINCIPLE INCORPORATING THE RESTRAINING EQUATION

As discussed in section 3.1.2, due to the computation error factors, the MMI does not equal 0 (or 1) during external (or internal) faults. This can be seen from the simulation results given in section 3.1.3. Drawing on the restraining current (2.16) in the conventional 87L to secure the differential protection, for similar consideration, a restraining equation is built based on the fault component circuit during internal faults displayed in Figure 3-3. In this section, the line differential protection principle incorporating the restraining equation is named as 87L(MMI-1) for the convenience of narration.

3.2.1. MODEL MAPPING ANALYSIS OF RESTRAINING EQUATION

Suppose for a moment that the external grid link in Figure 3-3 is absent. One can build the following two voltage equations, respectively [110].

$$u_s\left(t\right)=-R_s i_s\left(t\right)-L_s\frac{di_s\left(t\right)}{dt} \tag{3.11}$$

$$u_r\left(t\right)=-R_r i_r\left(t\right)-L_r\frac{di_r\left(t\right)}{dt} \tag{3.12}$$

Drawing on the reciprocal relationship of $K_{s-r}=\frac{\dot{I}_s}{\dot{I}_r}=\frac{Z_n+(D-d)Z}{Z_m+dZ}$ between two-sided currents and impedance in frequency-domain ($\dot{I}_s$, $\dot{I}_r$, Z_s, Z_r, and Z correspond to the time-domain quantities in Figure 3-3), for a certain fault distance d, one can infer that the current ratio $\frac{i_s}{i_r}$ in time-domain meets a similar real scale factor,

$$k_{s-r}\left(d\right)=\frac{i_s}{i_r} \tag{3.13}$$

Substituting (3.11)-(3.13) into (3.3), the restraining equation is finally deduced [110],

$$\begin{aligned} u_{cd}\left(t\right)&=-\frac{R_r+k_{s-r}R_s}{1+k_{s-r}}i_{cd}\left(t\right)-\frac{L_r+k_{s-r}L_s}{1+k_{s-r}}\frac{di_{cd}\left(t\right)}{dt}\\ &=-R_{eq}i_{cd}\left(t\right)-L_{eq}\frac{di_{cd}\left(t\right)}{dt}\end{aligned} \tag{3.14}$$

where R_{eq} and L_{eq}, the equivalent system parameters, are the function of some unknown quantities, e.g. fault location and source parameters. Subsequently, the

recursive Least-Square method is adopted in this thesis to estimate R_{eq} and L_{eq} in the restraining equation (3.14) [110]. Detailed estimation formulas can be found in Appendix C.

With the existence of the external grid link in Figure 3-3, assume that the source impedance meet the following parallel relations,

$$\begin{cases} R_s + (j\omega)\cdot L_s = (R_{s.1} + (j\omega)\cdot L_{s.1}) \| (R_{s.2} + (j\omega)\cdot L_{s.2}) \\ R_r + (j\omega)\cdot L_r = (R_{r.1} + (j\omega)\cdot L_{r.1}) \| (R_{r.2} + (j\omega)\cdot L_{r.2}) \end{cases} \tag{3.15}$$

where $j\omega$ represents the complex factor. '||' is the symbol of parallel function.

The fault circuit of Figure 3-3 will be equivalent to the one given in Figure 3-8. From the black path in Figure 3-8, one can see that the restraining equation (3.14) is also valid when substituting the source parameters (R_s, L_s, R_r, L_r) with ($R_{s.1}$, $L_{s.1}$, $R_{r.1}$, $L_{r.1}$). Since the new source parameters are included in R_{eq} and L_{eq} during the Least-Square method-based parameter estimation, one may infer that the restraining equation (3.14) applies to the system condition with external grid connection too.

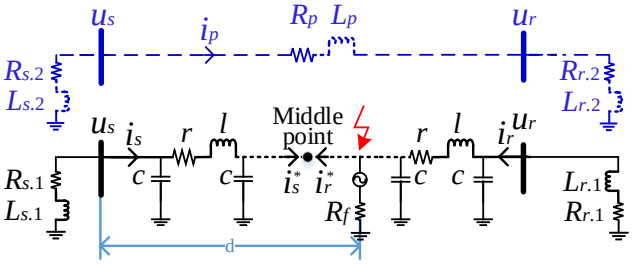

Figure 3-8 Decoupled fault component circuit during internal fault

From the derivation of the restraining equation (3.14), one knows that the restraining equation has a complete mapping relation with the internal fault-based model in Figure 3-3. Rewriting (3.14) as [110],

$$f_{res}(t) + g_{res}(t) = 0 \tag{3.16}$$

where

$$\begin{cases} f_{res}(t) = R_{eq} i_{cd}(t) + L_{eq} \dfrac{di_{cd}(t)}{dt} \\ g_{res}(t) = u_{cd}(t) \end{cases}.$$

By adopting the computation method of model mapping index defined in section 3.1.2-A, one can calculate the model mapping index MMI_{res} of the restraining

equation (3.14). In addition, MMI_{res} meets exactly a reverse mapping relationship between internal and external faults compared with MMI_{diff} mentioned in section 3.1. In detail, MMI_{res} tends to 0 during internal faults, but it approaches 1 during external faults. Table 3-3 lists the convergent tendencies of both MMI_{diff} and MMI_{res} under different fault conditions. Meanwhile, the ratio of MMI_{diff} to MMI_{res} is given too.

TABLE 3-3 CONVERGENT TENDENCY OF DIFFERENT MMIS [110]

MMIs / Faults	MMI_{res}	MMI_{diff}	$\frac{MMI_{res}}{MMI_{diff}}$
Internal fault	tends to 0	tends to 1	< 1
External fault	tends to 1	tends to 0	> 1

Subsequently, the protection criterion of 87L(MMI-1) including the restraining component is defined as [110],

$$R_{MMI} = \frac{MMI_{res}}{MMI_{diff}} < 1 \tag{3.17}$$

To guarantee the relay reliability, criterion (3.17) needs to be satisfied continuously for a certain time interval. A longer pre-defined time interval improves the reliability, however, it will sacrifice the speed performance. Here, a quarter of the fundamental frequency cycle is considered for the time interval.

3.2.2. CRITERION IMPLEMENTATION

In a three-phase system, both MMI_{diff} for the differential equation (3.4) and MMI_{res} for the restraining equation (3.14) should be calculated to implement the protection criterion (3.17).

For the restraining equation (3.14), it is directly revised as,

$$u_{cd}^{\phi}(t) = -R_{eq}^{1}\left(i_{cd}^{\phi}(t) + k_r i_{cd}^{0}(t)\right) - L_{eq}^{1}\frac{d\left(i_{cd}^{\phi}(t) + k_l i_{cd}^{0}(t)\right)}{dt} \tag{3.18}$$

where the zero sequence compensation of differential current i_{cd} improves the sensitivity during L-G faults [106]. Superscript 'ϕ' has the same definition to the one in section 3.1.2. i_{cd}^{0}, $k_r = (R_{eq}^{0} - R_{eq}^{1})/R_{eq}^{1}$ and $k_l = (L_{eq}^{0} - L_{eq}^{1})/L_{eq}^{1}$ represent the zero-sequence differential current, the resistive and inductive zero sequence

compensation factors, respectively. R_{eq}^{1}, L_{eq}^{1} and R_{eq}^{0}, L_{eq}^{0} are the equivalent system parameters in positive and zero sequence systems [110].

The proposed 87L(MMI-1) is further described in the flowchart shown in Figure 3-9.

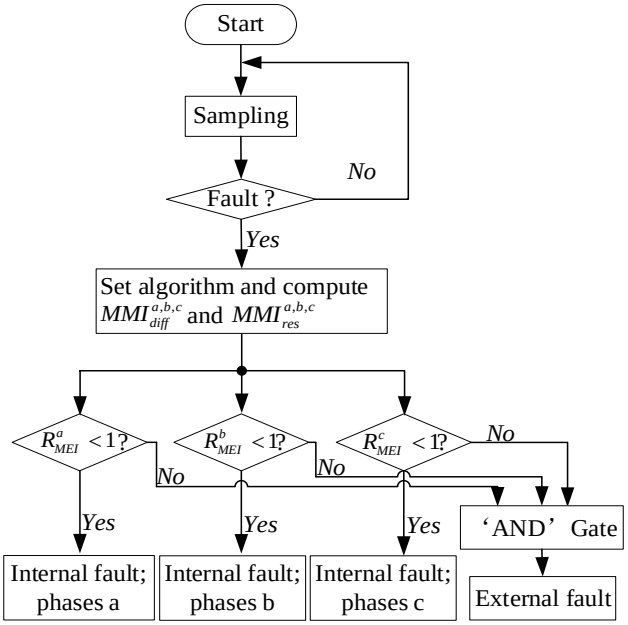

Figure 3-9 Flowchart of the proposed 87L(MMI-1) [110]

3.2.3. CASE STUDY

The cable system is deemed to be a promising power transmission method due to the slight visual pollution and land resource waste, being widely adopted in the Danish power systems [111]. For the cable system, the evident capacitive parameter is the main difference compared with the conventional over-head-line, which draws a lot of attention to the calibration problem of differential protection in cable systems [111-112]. In view of the capacitive current compensation, Ref. [112-115] have reported several effective methods. In general, they include two categories, i.e. the passive compensating type and the active eliminating type. For the passive method, a programmable current threshold is adopted to compensate for the pre-calculated capacitive current component, probably reducing the relay sensitivity. For the active method, the capacitive current estimation from the terminal current (or voltage) is subtracted in the differential current.

The above 87L(MMI-1) is free of compensation for the capacitive current due to the utilization of the compensated current-based differential equation [110]. This has been mentioned at the beginning of section 3.1. In this section, the 87L(MMI-1) is tested in a cable transmission system built with DIgSILENT/PowerFactory.

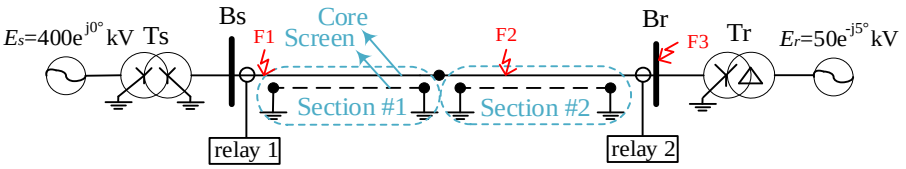

Figure 3-10 Test model of a cable transmission system [110]

Figure 3-10 displays a 165 kV transmission system including two cross-bonded major sections. The system runs at 50 Hz. The parameters of the cable system are respectively given in Table A-4, Figure A-1, and Table A-5 in Appendix A. Sampling frequency is set as 4 kHz for fault records. Similar to section 3.1.3, a 20 ms data window is adopted in this section.

As shown in Fig. 3-10, different fault positions are considered to test 87L(MMI-1).

1) $F1$ and $F2$ are two internal fault positions, located at 1 km and 40 km away from terminal B_s, respectively.
2) $F3$ represents an external fault position on terminal B_r.

In the following part, four simulation scenarios are organized, including the feasibility validation in scenario 1 and the influence analysis in scenarios 2~4, i.e. the DC offset in fault currents, the power swing, and the CT saturation.

Scenario 1 [110]: In this scenario, the feasibility of 87L(MMI-1) is first verified with the consideration of different fault types, fault locations, fault resistance, and (pre-fault) system loading. Figure 3-11 depicts the dynamic R_{MMI} of two bolted fault cases in the cable system. In the figure, the gray area below the threshold and the upper blank area respectively represent the operating and restraining zones. For case 1 in Figure 3-11 (bolted L-L fault BC at $F1$), only the R_{MMI} of phases b and c stabilize in the operating zone. Meanwhile, the healthy phase R_{MMI} crosses into the restraining zone rapidly. Case 2 in Figure 3-11 corresponds to the bolted L-G fault AG at point $F3$. Under such external fault condition, R_{MMI} of all three phases enter the restraining zone rapidly.

As a comparison, the high resistive fault condition for the same cases in Figure 3-11 are re-tested, simulation results shown in Figure 3-12 prove that the 87L(MMI-1) is still effective for the high resistive faults. As mentioned in section 3.1.3, the model mapping relationships are definite regardless of the fault resistance, applying to both the differential and restraining equations.

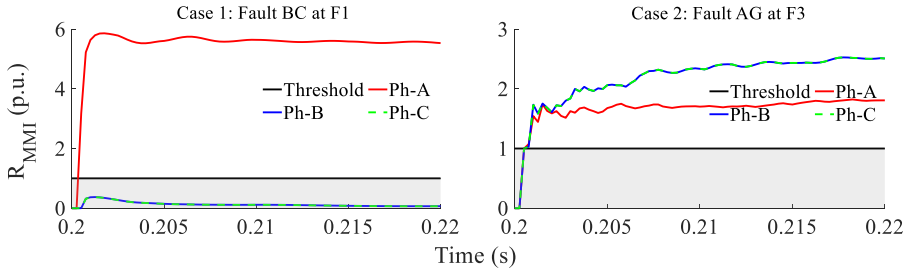

Figure 3-11 Dynamic R_{MMI} for different bolted faults

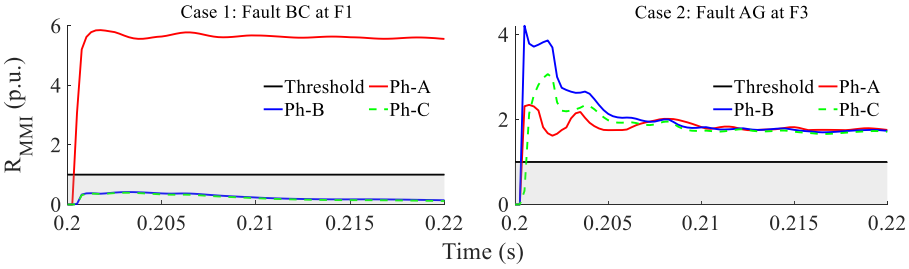

Figure 3-12 Dynamic R_{MMI} for different resistive faults ($R_f = 300\Omega$)

TABLE 3-4 LIST OF THE AVERAGE R_{MMI} UNDER DIFFERENT CABLE FAULT CONDITIONS [110]

Fault types $R_f = 0\ \Omega$		Column 1				Column 2			
		Cable loading = 47%				Cable loading = 82%			
		Ph-A	Ph-B	Ph-C	Fault	Ph-A	Ph-B	Ph-C	Fault
AG	*F1*	0.372	2.312	2.296	'+, -, -'	0.369	2.323	2.307	'+, -, -'
	F2	0.504	1.818	1.793	'+, -, -'	0.459	2.067	2.014	'+, -, -'
	F3	1.648	2.029	2.029	'-, -, -'	1.45	1.516	1.513	'-, -, -'
BC	*F1*	5.652	0.183	0.181	'-, +, +'	5.647	0.172	0.171	'-, +, +'
	F2	5.609	0.203	0.201	'-, +, +'	5.66	0.156	0.154	'-, +, +'
	F3	5.693	4.134	4.142	'-, -, -'	5.676	3.073	3.083	'-, -, -'
ABC	*F1*	0.107	0.173	0.078	'+, +, +'	0.112	0.177	0.081	'+, +, +'
	F2	0.113	0.161	0.085	'+, +, +'	0.118	0.169	0.088	'+, +, +'
	F3	1.859	2.071	1.667	'-, -, -'	1.576	1.639	1.418	'-, -, -'

* Note: '+' and '-' indicate the faulty and healthy phases, respectively.

In addition, Table 3-4 compares the influence of pre-fault system loading on the 87L(MMI-1). To do this, the pre-fault transmission angle (angular difference of two-sided potentials) is adjusted from 5° to 11°, leading to the increase of cable line loading from the initial 47% to 82%. Here, different bolted faults and fault positions are considered. The table lists the average R_{MMI} within the first half data window after faults. One can see that the average R_{MMI} in the healthy phase(s) during internal faults and those in all three phases during external faults are larger than 1. This accords with the criterion (3.17). Comparing the average R_{MMI} for the same faults in column 2 with

those in column 1, the average R_{MMI} vary slightly, proving that the influence of pre-fault system on the 87L(MMI-1) is slight. That is, the model mapping relationships are rarely affected by load currents.

Scenario 2 [110]: In addition, the influences of the DC offset on the 87L(MMI-1) are also investigated. It is well known that the smaller the initial fault voltage angle is, the larger the DC offset is. In this part, case 1 of fault BC at $F1$ in Figure 3-11 is re-tested by setting the fault voltage initial angle as 0°. Under such fault condition, one can see heavy DC offset in the two-sided fault currents in Figure 3-13 (a). However, the R_{MMI} curves in Figure 3-13 (b) show slight changes during the initial fault transient only, compared with the ones in Figure 3-11. This proves that the 87L(MMI-1) has robust performance for the DC offset in fault currents, which benefits from the utilization of time-domain fault information to compute the R_{MMI}.

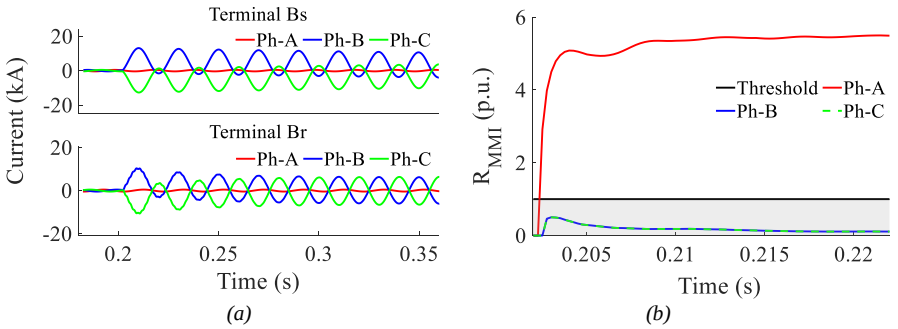

Figure 3-13 Dynamic R_{MMI} for bolted fault BC at F1 with large DC offset

Scenario 3: After the clearance of a close-in disturbance (e.g. short-circuit fault) in the power system, SG probably undergoes a power swing phase. In this phase, differential protection may risk malfunction. For this consideration, the impact of power swing on the 87L(MMI-1) is verified in the reconfigured test system of Figure 3-10. As shown in Figure 3-14, the voltage source E_r in Figure 3-10 is substituted with a SG, where the IEEET1-type automatic voltage regulator and the IEEEG1-type governor are deployed to regulate the turbine voltage and speed. And only one major section with 20 km cable line is configured. Other system parameters are kept the same as those in Figure 3-10.

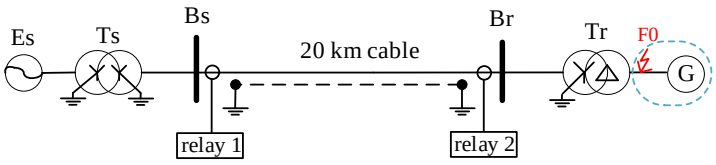

Figure 3-14 Test cable system considering power swings

To create significant power swings, short-circuit events (occurring at 0.4 s) are first set at $F0$ vicinal to the generator, and they are cleared at 0.5 s. As displayed in Figure 3-15 (a), terminal currents show a certain oscillation after the clearance of the bolted 3PH fault. However, the corresponding R_{MMI} curves in Figure 3-15 (b) only perform slight variations after the fault clearance and remain in the restraining zone. It indicates that the power swing in the system after the fault clearance does not lead to the malfunction of 87L(MMI-1). This is also proven by a bolted L-L-G fault ACG at $F0$ with the same fault inception and clearance times, as displayed in Figure 3-16.

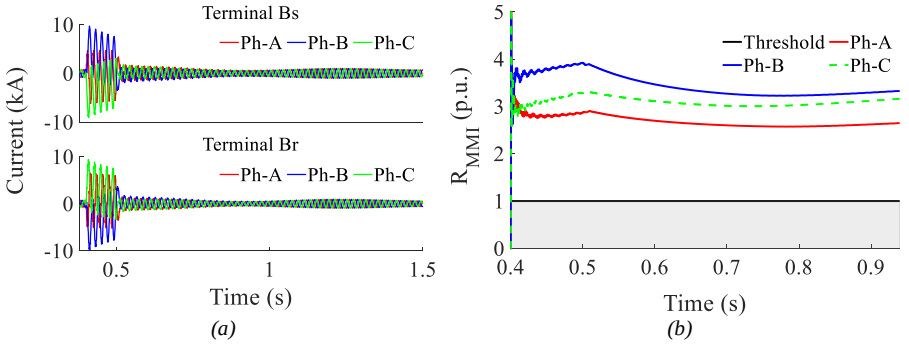

Figure 3-15 Dynamic R_{MMI} during power swing after the clearance of 3PH fault ABC

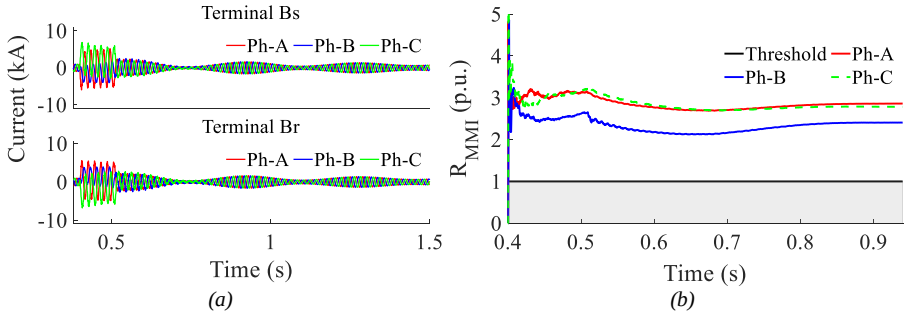

Figure 3-16 Dynamic R_{MMI} during power swing after the clearance of L-L-G fault ACG

Scenario 4 [110]: As for the conventional 87L, the transient CT saturation can heavily affect its performance. In this part, the effects of CT saturation on the 87L(MMI-1) are assessed. In general, the larger the fault current offset is, the heavier the CT saturation probably is. For differential protection, the single-sided CT saturation is deemed to be the most harmful condition, which usually happens during external faults. Setting the fault inception angle as 0°, the influence is tested based on a bolted L-G fault BG located at point $F3$.

Figure 3-17 gives the instantaneous fault currents, including both the saturated and unsaturated operating conditions of the CT at terminal Br. Under such two CT operating conditions, the corresponding R_{MMI} results are plotted in Figure 3-18. For the unsaturated case 1, R_{MMI} in three phases all stay in the restraining zone. However, for the saturated case 2, R_{MMI} all show drastic variations after the inception of CT saturation (at around 0.208s), which even approach the operating zone. This proves that the CT saturation can finally affect the reliability of 87L(MMI-1).

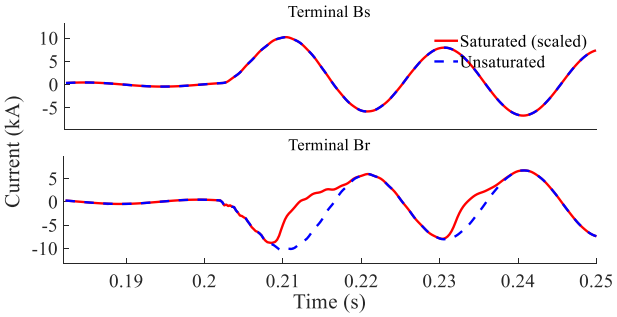

Figure 3-17 Instantaneous currents in the faulty phase under different CT saturation cinditions

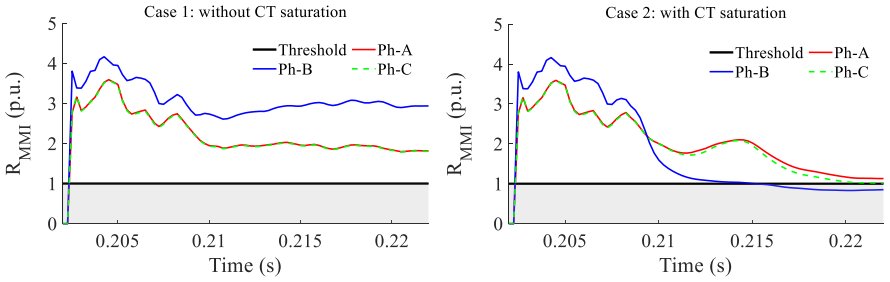

Figure 3-18 Dynamic R_{MMI} for external fault BG under different CT saturation conditions

One thing is that the CT saturation does not directly happen after fault, i.e. the primary current can be precisely reproduced by the CT during the time-to-saturation. Bearing this factor in mind, one can infer that the 87L(MMI-1) can detect the fault states before the CT saturation, if the lasting time (i.e. the time interval discussed below (3.17)) for criterion judgement in the proposed time-domain approach is selected properly.

3.3. OPTIMAL APPLICATION IN THE POWER NETWORK WITH FCG-BASED PLANT INTEGRATION

The above 87L(MMI-1) shows good performance in the power network connecting SGs, however, the FCG-based plant may be problematic. As discussed in section 2.1.2, FCG shows the nonlinear control feature when grid faults occur. Finally, it operates as a voltage-controlled current source during faults.

In general, the fault component circuits at FCG-based plant side (in Figures 3-2 and 3-3) need to be revised as Figure 3-19. In the figure, the original impedance circuits are replaced by a voltage-controlled current source. i_{s_L} is the equivalent source current. In the view of revised fault component circuits, the compensated current-based differential equation deduced in section 3.1.1 (relating to the inherent line parameter only) is unaffected. However, the restraining equation deduced in section 3.2.1 is affected by the PEC control. In detail, the passive fault component circuit displayed in Figure 3-3 is no longer valid in the positive sequence circuit when FCG-based plant is connected. On the other hand, the negative sequence circuit at FCG-based plant side depends on the negative sequence control of PEC. Under the BCC control mode, it is open-circuit.

In most practical applications, PEC uses a three-phase three-leg configuration, which cannot produce any zero-sequence current. Under such condition, the zero-sequence loop mainly includes the transmission link and the grounding circuit of the transformer at the high voltage side. As a result, the restraining equation (3.15) in the zero-sequence system is unaffected and mainly used in this section.

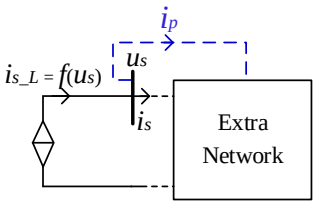

Figure 3-19 Equivalent fault component circuits at FCG-based plant side [102]

3.3.1. UNSYMMETRICAL VECTOR RECONSTRUCTION

But, one should know that the zero-sequence loop can only reflect the L-G (or L-L-G) faults. To improve the sensitivity of the restraining equation (3.15) to L-L or 3PH faults, the unsymmetrical vector reconstruction (UVR) is proposed [102]. Figure 3-20 depicts the graphical representation of UVR. Equation (3.20) is the corresponding transformation function.

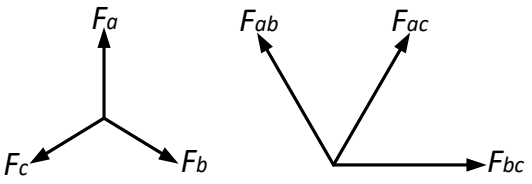

(a) *(b)*

Figure 3-20 Graphical representation of UVR. (a) Symmetrical vector (b) Unsymmetrical vector [102]

$$\begin{bmatrix} F_{ab} \\ F_{bc} \\ F_{ac} \end{bmatrix} = M \cdot \begin{bmatrix} F_a \\ F_b \\ F_c \end{bmatrix}, \quad M = \begin{bmatrix} 1 & -1 & 0 \\ 0 & 1 & -1 \\ 1 & 0 & -1 \end{bmatrix} \tag{3.20}$$

Based on this, the new vectors in the unsymmetrical reference frame can represent any L-L faults in the symmetrical reference frame. For example, an original L-L fault can be viewed as a single-phase fault in the unsymmetrical reference frame, so that the sensitivity based on the zero-sequence component is enhanced.

3.3.2. CRITERION IMPLEMENTATION

To distinguish with the 87L(MMI-1) discussed in section 3.2, the new approach incorporating the UVR transformation is named as 87L(MMI-2). For 87L(MMI-2), both the model mapping index MMI_{res}^{0} and MMI_{res}^{00} of the restraining equation (3.15) in the original reference frame and the unsymmetrical one are needed, where the superscript '00' represents the variables in the unsymmetrical reference frame. After that, the composite model mapping index $MMI_{res} = MMI_{res}^{0} * MMI_{res}^{00}$ will be calculated, which would approach 0 in the case of an internal fault. In detail,

1) Sample the voltage and current vectors $u_{cd}^{\Phi}(k)$ and $i_{cd}^{\Phi}(k)$ and reconstruct the vectors $u_{cd}^{\Phi\Phi}(k)$ and $i_{cd}^{\Phi\Phi}(k)$ in the unsymmetrical reference frame. Then is the phase-mode transform:

$$\begin{bmatrix} u_{cd}^{\psi}(k) \\ i_{cd}^{\psi}(k) \end{bmatrix} = S \cdot \begin{bmatrix} u_{cd}^{\phi}(k) \\ i_{cd}^{\phi}(k) \end{bmatrix}, \begin{bmatrix} \overline{u}_{cd}^{\psi}(k) \\ \overline{i}_{cd}^{\psi}(k) \end{bmatrix} = S \cdot \begin{bmatrix} u_{cd}^{\phi\phi}(k) \\ i_{cd}^{\phi\phi}(k) \end{bmatrix} \tag{3.21}$$

2) Compute the sub-sequences $f_{res}^{0}(k)$, $g_{res}^{0}(k)$ and $f_{res}^{00}(k)$, $g_{res}^{00}(k)$ of the restraining equation (3.15) in the earth modulus circuit.

3) Compute MMI_{res}^{0} and MMI_{res}^{00} of the restraining equation (3.15). Then, compound the MMI_{res}.

Equation (3.22) specifies the protection criterion of the 87L(MMI-2), including the pickup and operating criteria [102]. The pickup criterion integrates the starting function and the phase selection, where the threshold is initialized as 0.5. After the pickup criterion is satisfied, the corresponding R_{MMI} needs to be solved furthermore. Once R_{MMI} meet(s) the operating criterion, the fault status can be detected.

$$\begin{cases} MMI_{diff} > 0.5 \\ R_{MMI} = \dfrac{MMI_{res}}{MMI_{diff}} < 1 \end{cases} \tag{3.22}$$

A same time interval as for (3.17) can be adopted for reliability consideration. The implementation of 87L(MMI-2) is finally given in the flowchart of Figure 3-21.

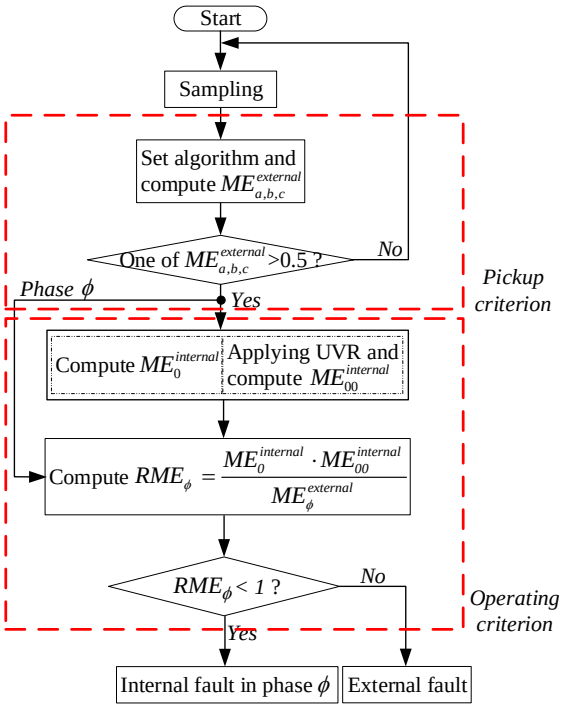

Figure 3-21 Flowchart of the 87L(MMI-2) [102]

3.3.3. CASE STUDY

In this section, the 87L(MMI-2) is validated in the test system of Figure 2-6. A 0.3 ms sampling period and 10ms data window are adopted.

Compared with 87L(MMI-1), 87L(MMI-2) is based on a similar model mapping principle to detect faults. The main difference is the selection of single earth modulus

for the computation of restraining quantity MMI_{res} due to the nonlinear FCG fault control. Thus, the influencing analysis of the DC offset, the power swing, and the CT saturation will not be repeated here.

This section mainly focuses on the influencing analysis of the various FCG fault controls, the flexible FCG operation, and the limited FCG fault contribution capability on the proposed 87L(MMI-2).

Scenario 1: Firstly, the impacts of the varying PEC fault controls are considered. For comparison purposes, the most severe scenario in Table 2-2 with the capacity ratio of SG to FCG equaling 240:60 MW is re-tested. In section 2.2.1, it is found that the 87L element in phase C will lose the sensitivity and fail to detect the fault under FCG fault control modes A and B, as displayed in Figure 2-11 (c) and Figure 2-12. Correspondingly, the simulation results of 87L(MMI-2) under these two fault control modes are displayed in Figure 3-22. In the figure, the left side subplot corresponds to the pickup criterion, in which the gray area indicates the pickup region. The right side subplot corresponds to the operating criterion, and the gray area denotes the operating region. For the case under control mode A in Figure 3-22 (a), MMI_{diff} in phases B and C enter the pickup region rapidly after the fault, meanwhile, R_{MMI} in phases B and C maintain in the operating region continuously. Thus, one knows that the 87L(MMI-2) detects the L-L fault BC successfully. So do the simulation results in Figure 3-22 (b), where FCG operates under mode B after the grid fault.

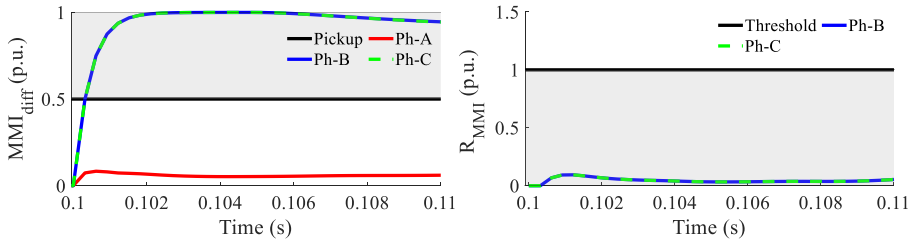

(a)

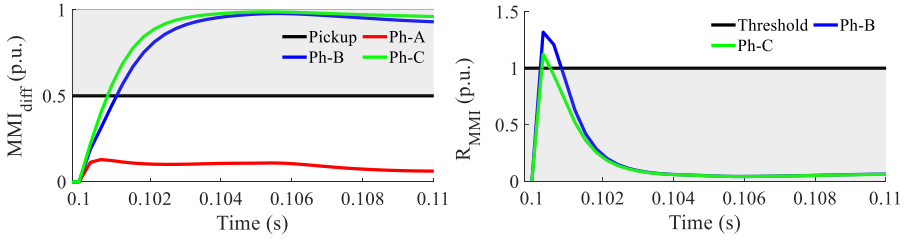

(b)

Figure 3-22 Performance of 87L(MMI-2) for bolted fault BC at point F1 (a) FCG operates at mode A (b) FCG operates at mode B

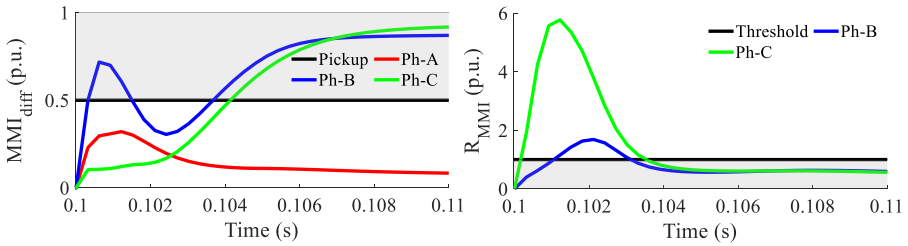

Figure 3-23 Performance of 87L(MMI-2) for bolted fault BC at point F1

Moreover, Figure 3-23 displays the result of 87L(MMI-2) for the same fault BC under fault control mode C. Comparing MMI_{diff} and R_{MMI} of 87L(MMI-2) under different fault control modes shown in Figures 3-22 and 3-23, 87L(MMI-2) shows an increased transient period when FCG changes the fault control mode from A to B then to C. This is because the post-fault current of FCG has the largest variation compared to the pre-fault load current under the fault control mode C. However, the steady-state plots of MMI_{diff} and R_{MMI} prove that the 87L(MMI-2) has good adaptability regardless of the FCG fault control modes.

Scenario 2: In section 2.2.1, it is pointed out that the injection of negative sequence current from the FCG-based plant can improve the sensitivity problem of 87L during the L-L fault to a certain degree. From another view, one can say the performance of 87L is prone to the PEC fault control. In this part, the study case in Figure 2-13 is re-tested and simulation results of 87L(MMI-2) are displayed in Figure 3-24.

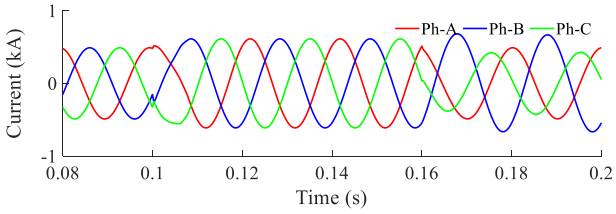

(a)

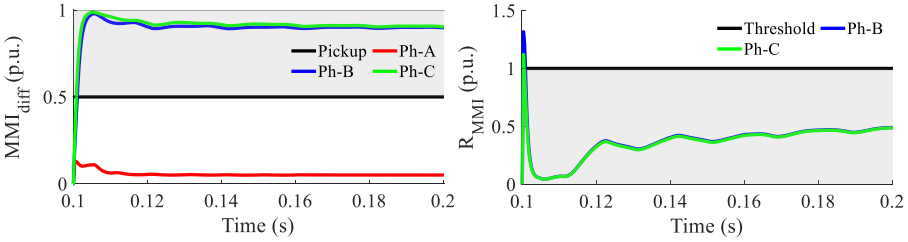

(b)

Figure 3-24 Influence of the extra negative sequence control on 87L(MMI-2) for bolted fault BC at point F1 (a) Instantaneous current at FCG side (b) Results of 87L(MMI-2)

In this case, a longer data window of 100 ms is adopted to show the result before and after the activation of negative sequence control. Figure 3-24 (a) displays the instantaneous currents of FCG-based plant. One can see the clear variation in the current curves after the activation of negative sequence control. From Figure 3-24 (b), one can see that MMI_{diff} (and R_{MMI}) in phases B and C continuously satisfy the pickup criterion (and the operating one) before and after the control variation. Results show that the injection of negative sequence current from FCG-based plant almost does not affect the 87L(MMI-2).

Scenario 3: The intermittent characteristics of renewable energies make the FCC have flexible outputs. Even worse, the overcurrent/under-voltage protective functions in the PEC control system usually respond to grid faults. All these can cause the relay devices equipped in the transmission system connecting FCG-based plant to suffer from a varying system loading. Thus, it is meaningful to investigate such effects on the protection system.

A step current output from FCG-based plant during grid fault, decreasing to the half of the initial value at 0.16 s, is simulated to verify the performance of 87L(MMI-2). Here, a L-G fault AG located at $F2$ (40 km away from FCG-based plant) and an external L-L-G fault BCG at $F3$ (middle point of $L_{3\text{-}4}$) are tested. Simulation results are displayed in Figures 3-25 and 3-26, respectively.

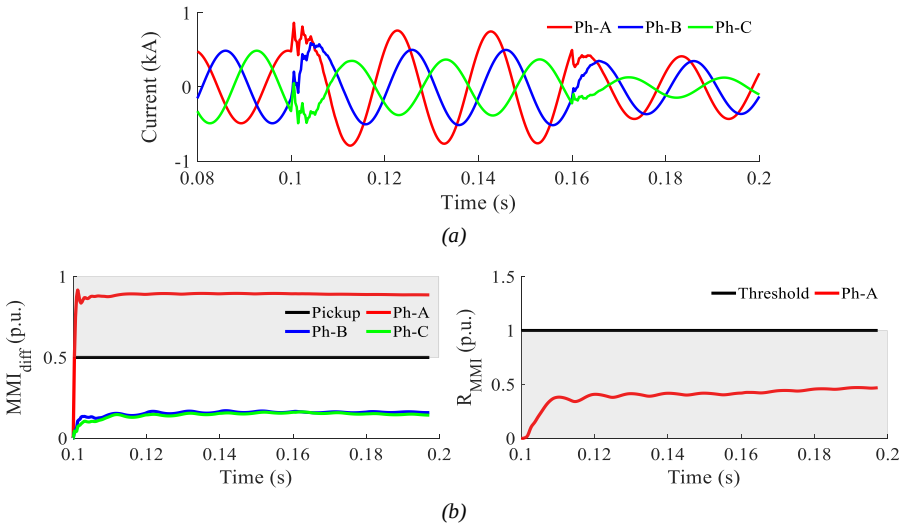

Figure 3-25 Influence of the FCG flexible operation on the 87L(MMI-2) for a L-G fault AG at F2. (a) Instantaneous current at FCG side (b) Results of 87L(MMI-2)

In Figures 3-25 (a) and 3-26 (a), FCG currents show the sharp variations at 0.16 s. However, the influence of the FCGs' step current variations on the indices MMI_{diff} and R_{MMI} is slight, as shown in Figures 3-25 (b) and 3-26 (b). Because the variation

of FCGs' current output does not affect the pre-defined model mapping relationships. For the external fault BCG in Figure 3-26 (b), none of MMI_{diff} in three phases enter the pickup region. Only the plot of pickup variables is given, while no operating variable R_{MMI} is calculated and plotted in this case.

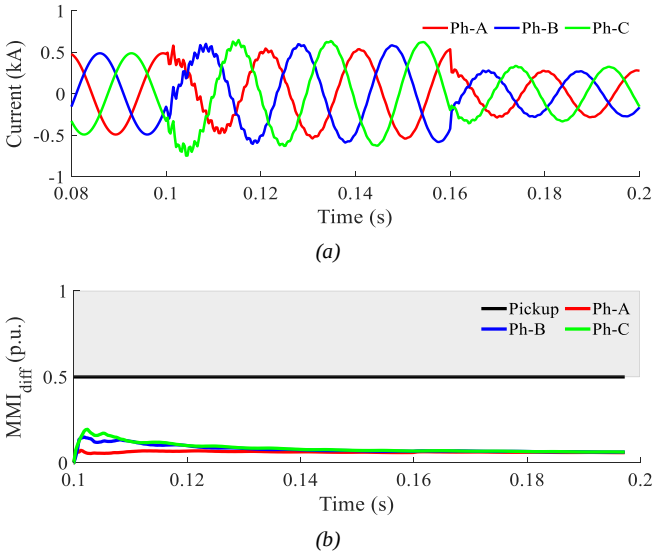

Figure 3-26 Influence of the FCG flexible operation on the 87L(MMI-2) for a L-L-G fault BCG at F3. (a) Instantaneous current at FCG side (b) Results of 87L(MMI-2)

Scenario 4: High fault resistance usually diminishes the magnitude of fault currents in the power system, especially during L-L (or 3PH) faults. This is more evident in the power system integrating FCG-based plant, due to the limited PEC short-circuit capacity in positive and negative sequence systems.

During high resistive L-L faults, the sequence elements (negative current-based one) of conventional 87L can take the place of phase elements to provide additional sensitivity. However, it cannot apply to the high resistive 3PH fault, since the FCG-based plant outputs balanced fault current.

This scenario tests a 3PH fault located at point $F1$. The fault resistance of 800 Ω is considered. In this case, FCG operates at fault control mode B after grid faults. For comparison purposes, simulation results of both the 87L and the 87L(MMI-2) are displayed in Figure 3-27. From the differential and restraining currents shown in Figure 3-27 (a), one can see that all three differential relays fail to clear the fault (as $I_{diff} < k_{res} I_{res}$). Figure 3-27 (b) depicts the result of 87L(MMI-2). In the figure, MMI_{diff} in three phases cross into the pickup region rapidly after the fault, while R_{MMI} in three phases stay in the operating region at the same time. Results show that the 87L(MMI-2) can still deal with this high resistive fault effectively.

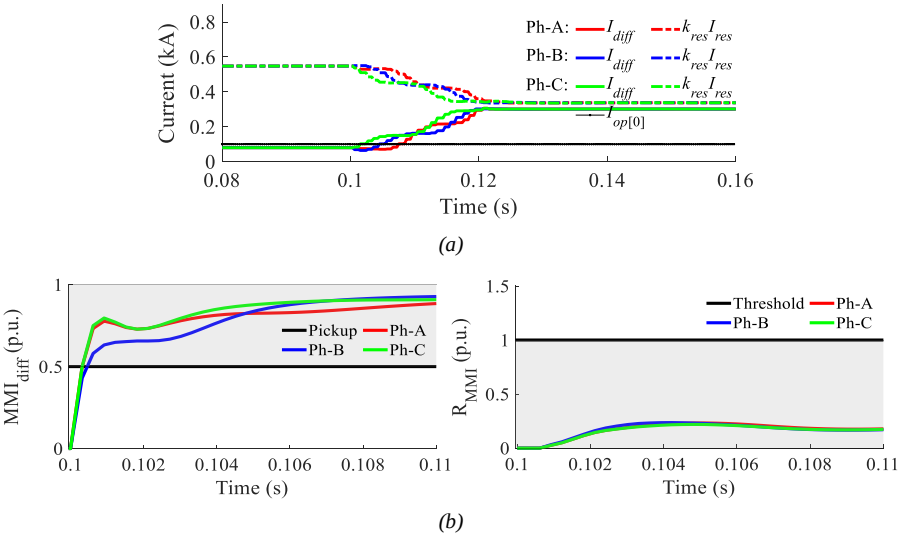

Figure 3-27 Influence of high resistive fault. (a) Results of 87L (b) Results of 87L(MMI-2).

Scenario 5: In this scenario, the 87L(MMI-2) is further evaluated in a meshed network. The test case in Figure 2-21 (c), bolted fault BC at F1 in the meshed network configuration, is re-tested. From the simulation results displayed in Figure 3-28, one can see that variables MMI_{diff} and R_{MMI} in phases B and C stabilize in the pickup region and operating region, respectively. 87L(MMI-2) can detect this internal fault occurring in the meshed network successfully.

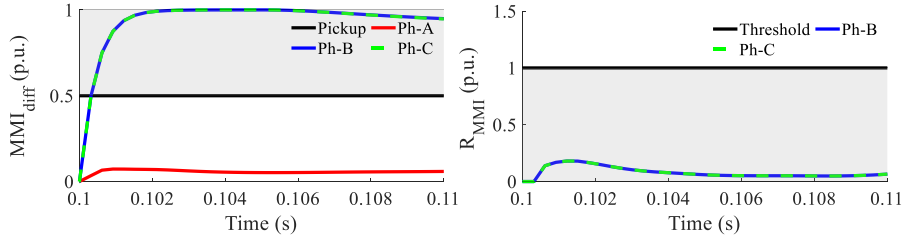

Figure 3-28 Performance of 87L(MMI-2) in meshed network for bolted fault BC at point F1

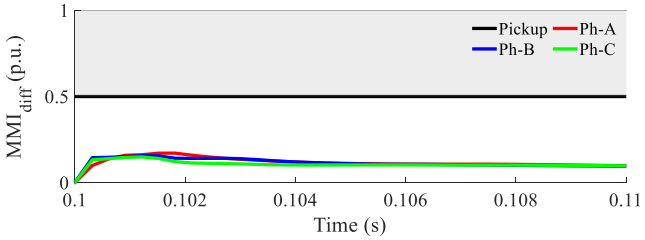

Figure 3-29 Performance of 87L(MMI-2) in meshed network for resistive fault AG at point F3 ($R_f = 100\Omega$)

Besides, the simulation results of 87L(MMI-2) for a resistive fault AG ($R_f = 100\ \Omega$) at F3 are given in Figure 3-29. Clearly, the pickup criterion is invalid in all three phases. 87L(MMI-2) can distinguish this external fault in the meshed network too.

3.4. DISCUSSION

After assessing the feasibility of compensated current-based differential principle in section 3.1, two kinds of improvements on the time-domain differential protections regarding different application backgrounds (i.e. SG-dominated power system and FCG plant-integrated power system) are discussed in sections 3.2 and 3.3, respectively. According to the comprehensive analysis and validation for the new time-domain differential protections, one can conclude the properties as follows:

First, these three differential approaches have excellent transient performance due to the direct application of the time-domain fault information [102, 109-110]. Take the comparative studies with the conventional 87L in section 3.3, for example. 87L(MMI-2) shows a faster convergence process generally.

Second, the compensated current-based differential equation has incorporated the capacitive influence of the line, making the new protections immune to the charging current. 87L(MMI-1) is proven sensitive enough in the tests of a cable system [110].

Third, the time-domain differential protection approaches detect the fault based on the model mapping index of the fault sampling to pre-defined fault models, rather than the comparison of electric quantity [102]. Thus, 87L(MMI-2) can effectively address the malfunction risk of the conventional 87L for L-L faults in the system connecting large-scale FCGs [102]. Besides, the fault resistance and the flexible operation of FCGs do not affect the fault component circuits. The 87L(MMI-2) can effectively deal with these fault conditions [102].

From the practical view, the newly proposed time-domain differential protection approaches only need simple computing resources to obtain the MMIs, being feasible [102]. Just like the travelling wave-based differential scheme, the two-sided currents and voltages require to be sampled synchronously [102]. For this, many advanced sampling and synchronization based on the modern communication technologies can be adopted, such as synchronization based on the channel time and the GPS [116]. In addition, the new time-domain approaches have a low sampling frequency requirement only [102].

Limitation statement:

The compensated current-based differential equation is deduced based on the time-domain computating method of Bergeron line model, which applies to a homogeneous line with the assumption of geometrical symmetry only. The non-homogeneous property (or geometrical asymmetry) in special transmission line is not in the scope of the proposed methods in this chapter.

CHAPTER 4. IMPEDANCE TILT ANGLE-BASED DISTANCE PROTECTION OF THE LINE EMANATING FROM FCG-BASED PLANT

In section 2.2.2 of chapter 2, it is pointed out that the distance protection equipped in the transmission line emanating from FCG-based plant suffers severe malfunction risks after the inception of resistive grid faults. Aiming at this relaying problem during resistive faults, the tilting feature of apparent impedance measured in distance relay is first analyzed, i.e. the impedance tilt angle (ITA). For improving the function of conventional distance protection, two kinds of countermeasures based on the ITA are presented in chapters 4 and 5.

In this chapter, a novel impedance tilt angle-based distance relaying scheme (ITA-21) is developed. The proposed ITA-21 detects the faults by comparing the tilting angles of apparent impedance relative to two line impedance positions, i.e. the fault point and the zone 1 set point.

4.1. BASIC PRINCIPLE

Re-considering the fault network shown in Figure 2-14, the apparent impedance in (2.20) is rewritten as,

$$Z_{app} = mZ + (1 + \frac{\dot{I}_r}{\dot{I}_s})R_f = mZ + \Delta Z \tag{4.1}$$

As mentioned in section 2.2.2, the tilting tendencies of apparent impedance during resistive grid faults (due to the modulating impedance ΔZ), relate to the angular difference between $\dot{I}_s$ and $\dot{I}_r$ determined by different Grid Codes. This demands to analyze the concrete problems in a concrete fault condition.

4.1.1. CLOCKWISE IMPEDANCE TILT (CWIT)

During grid faults, the active power output from FCGs is continuously desired for economic reasons by some transmission system operators, after the reactive power supporting is first satisfied, e.g. the definition of Danish and German Grid Codes. As

a result, the conventional distance relay (Con-21) at the power sending end tends to measure a reduced reactance, i.e. relay is at the risk of over-reach.

In this section, two ITA variables, i.e. θ_{Imp} and θ_{Imp}^{*}, are introduced to elaborate their qualitative relationships under different fault conditions. Firstly, θ_{Imp} and θ_{Imp}^{*} are defined as the tilting angles of Z_{app} to two line impedance at the fault point and the zone 1 set point, respectively. In detail, the tilting angle θ_{Imp} satisfies,

$$\theta_{Imp} = angle\left[\left(1+\frac{\dot{I}_r}{\dot{I}_s}\right)R_f\right] \tag{4.2}$$

Correspondingly, the tilting angle θ_{Imp}^{*} meets,

$$\begin{aligned}\theta_{Imp}^{*} &= angle\left(Z_{app} - Z_{Line}^{set}\right)\\ &= angle\left[(m-m_0)Z+\left(1+\frac{\dot{I}_r}{\dot{I}_s}\right)R_f\right]\end{aligned} \tag{4.3}$$

where $Z_{Line}^{set} = m_0 Z$ is the line impedance from the relay up to the zone 1 set point.

Figure 4-1 depicts the schematic representation of Z_{app} on impedance plane under the CWIT condition. Assume the counter-clockwise direction is positive in the complex plane. Comparing the ITAs in (4.2) and (4.3), one can see that the line impedance increment $(m-m_0)Z$ in (4.3) is ahead of the modulating impedance ΔZ during external faults, as $m > m_0$ is true. This always makes the tilting angle θ_{Imp}^{*} bigger than θ_{Imp}, as illustrated in Figure 4-1 (a)-(c). These three subplots correspond to three possible positions of Z_{app} relative to reactance element during external faults.

On the contrary, the line impedance decrement $(m-m_0)Z$ in (4.3) is behind the modulating impedance ΔZ during internal faults, since $m < m_0$ is true at this moment. This causes the tilting angle θ_{Imp}^{*} to be smaller than θ_{Imp} for internal faults, as illustrated in Figure 4-1 (d). In addition, one can infer that θ_{Imp}^{*} approximates to θ_{Imp} during boundary faults, as $m = m_0$, referring to Figure 4-1 (e).

To sum up, one has the angular relationship for internal (and boundary) faults as follows,

$$\theta_{Imp} \geq \theta_{Imp}^{*} \tag{4.4}$$

where $\theta_{Imp} = \theta_{Imp}^{*}$ represents the boundary faults.

Note that $\theta_{Imp} < 0$ is valid constantly during the CWIT condition.

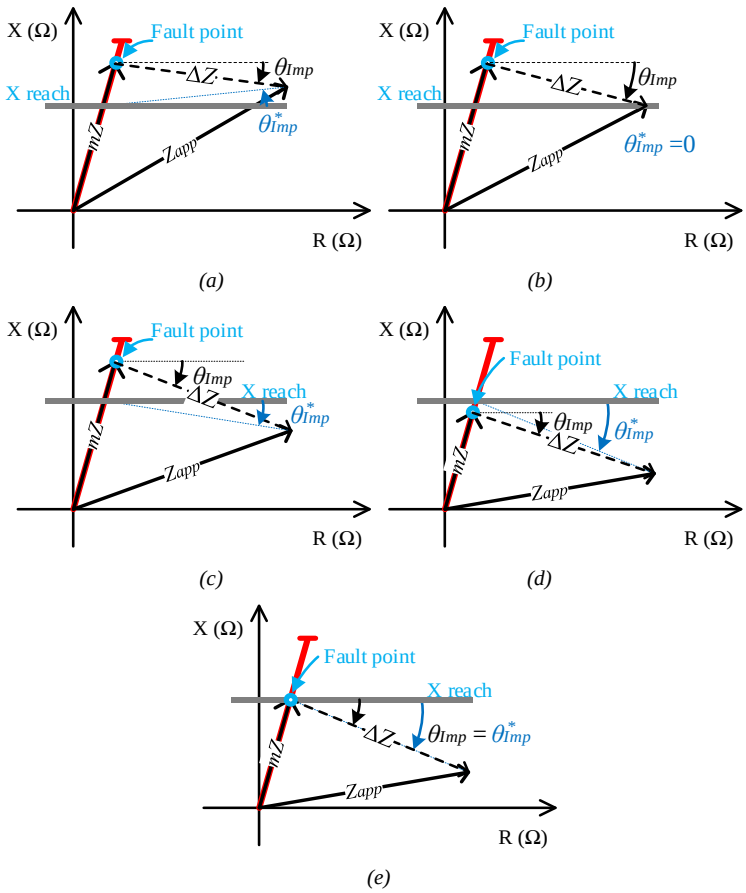

Figure 4-1 Schematic representations of apparent impedance on impedance plane under CWIT condition. (a) External fault situation 1 (b) External fault situation 2 (c) External fault situation 3 (d) Internal fault situation (e) Boundary fault situation

4.1.2. COUNTER-CLOCKWISE IMPEDANCE TILT (COUNTER-CWIT)

In general, counter-CWIT may occur when the active power output from FCG is limited (or even not required) in some special Grid Codes during grid faults. Relay is then at the risk of under-reach.

Under the counter-CWIT condition, the influences of line impedance variation $(m - m_0)Z$ on the quantitative relationships of θ^*_{Imp} to θ_{Imp} are in fact the same as the ones under the CWIT condition. This can be seen from the schematic representations of Z_{app} on impedance plane for the faults in forward direction, displayed in Figure 4-2. In the figure, subplots (a)-(c) correspond to three possible positions of Z_{app} relative

to reactance element during internal faults. Subplot (d) corresponds to the external fault situation, while subplot (e) corresponds to the boundary fault situation.

Clearly, (4.4) is also valid during internal (and boundary) faults under the counter-CWIT condition. Note that $\theta_{Imp} > 0$ is valid constantly under such condition.

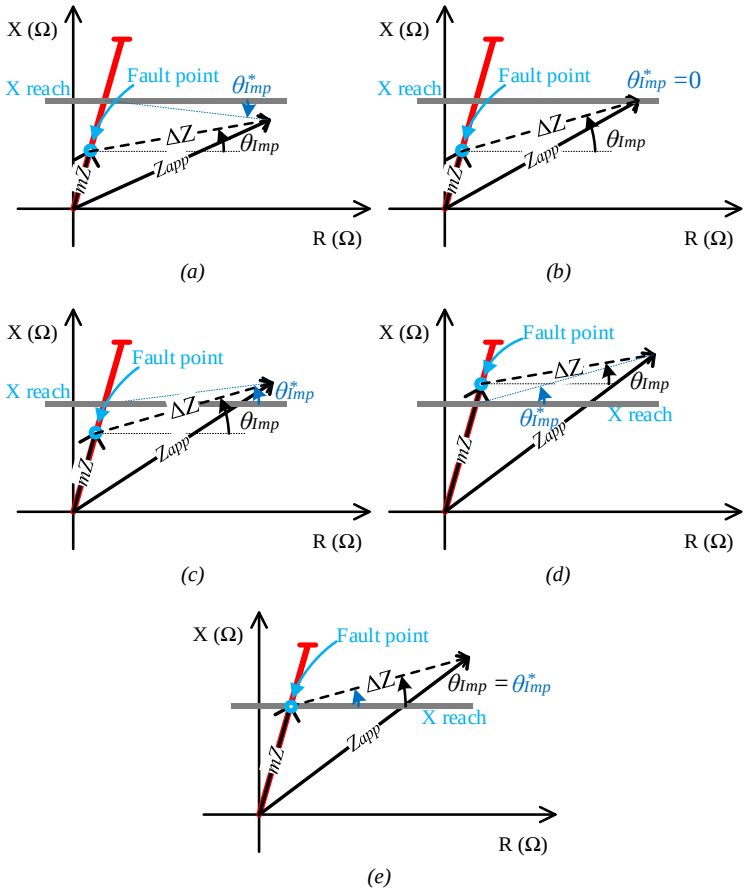

Figure 4-2 Schematic representations of apparent impedance on impedance plane under counter-CWIT condition. (a) Internal fault situation 1 (b) Internal fault situation 2 (c) Internal fault situation 3 (d) External fault situation (e) Boundary fault situation

4.1.3. NORMAL SITUATION

Moreover, if θ_{Imp} is detected staying in a small range (e.g. $\theta_{Imp} \in [-\zeta, \zeta]$), where ζ represents a tiny angle. The relay can be deemed to have no over- or under-reaching problem. The line impedance increment (or decrement) $(m - m_0)Z$ during external

(or internal) faults will respectively cause θ_{Imp}^{*} to be positive (or negative). From the schematic representations of Z_{app} on impedance plane under the normal condition given in Figure 4-3, one can see that (4.4) is still valid for internal (and boundary) faults under the normal condition.

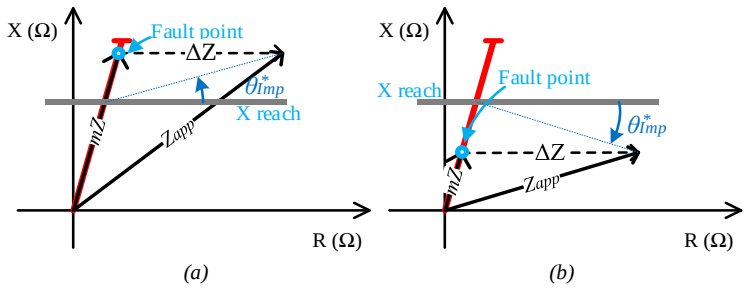

Figure 4-3 Schematic representations of apparent impedance on impedance plane under normal condition. (a) External fault situation (b) Internal fault situation

4.2. IMPLEMENTATION OF ITA-21

In section 4.1, the qualitative relationships between θ_{Imp}^{*} and θ_{Imp} are analyzed. The above analysis considers different tilting trends of apparent impedance during resistive grid faults, including CWIT, counter-CWIT, and normal conditions. This section first gives the complete protection criterion, followed by the detailed implementing process.

4.2.1. CRITERION ESTABLISHMENT

The protection criteria of ITA-21 for internal (and boundary) faults consist of the tilting direction criterion and the operating criterion, in detail,

$$\underbrace{\theta_{Imp}=\begin{cases}<-\zeta & , \text{ CWIT situation}\\ >\zeta & , \text{ counter-CWIT situation}\\ \subset[-\zeta,\zeta], & \text{normal situation}\end{cases}}_{Tilting\ \ direction\ \ criterion} \tag{4.5}$$

$$\underbrace{\theta_{diff}=\theta_{Imp}-\theta_{Imp}^{*}\geq 0}_{Operating\_Criterion} \tag{4.6}$$

In the above protection criteria, criterion (4.5), in fact, only indicates the impedance tilting tendencies, which is actually unnecessary to the implementation of the ITA-21 principle. Thus, ITA θ_{Imp} is not displayed separately in the following simulation

studies. In operating criterion (4.6), θ_{diff} is the deviation of θ_{Imp} to θ_{Imp}^{*}, named as DITA. By using criterion (4.6), all the internal (or boundary) faults can be correctly detected.

4.2.2. ESTIMATION OF THE ITAS

From the operating criterion (4.6), one can see that ITA-21 is based on the estimation of θ_{Imp} and θ_{Imp}^{*} during resistive grid faults. According to the definition of θ_{Imp}^{*} and θ_{Imp} in (4.2) and (4.3), one knows that θ_{Imp}^{*} is easy to be obtained during grid faults, as the impedance Z_{Line}^{set} and Z_{app} are known (or measurable). However, it is not true for θ_{Imp}. Since θ_{Imp} is affected by the remote current $\dot{I}_r$. As a result, the key of ITA-21 is to estimate θ_{Imp} with only the local fault information.

In a three-phase system, there are well-known formulas of apparent impedance in different fault loops. For L-G faults, e.g. fault AG, the apparent impedance (4.1) and the tilting angle (4.2) should be revised as,

$$Z_{AG} = mZ_1 + \frac{R_f \cdot \dot{I}_f}{\dot{I}_{sa} + K_0 \cdot \dot{I}_{0s}} \tag{4.7}$$

$$\theta_{AG} = angle\left(\frac{\dot{I}_f}{\dot{I}_{sa} + K_0 \dot{I}_{0s}} \right) \tag{4.8}$$

where $\dot{I}_{sa}$ and $K_0 = (Z_0 - Z_1)/Z_1$ are the fault current in phase A and the zero-sequence compensation factor, respectively.

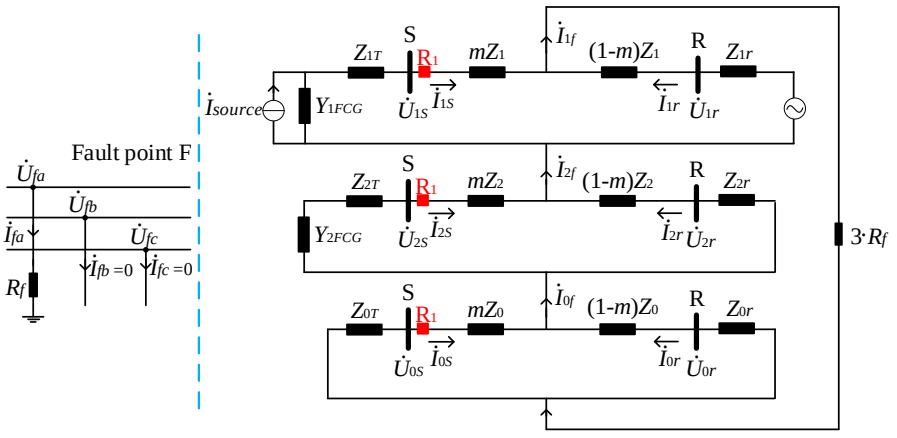

Figure 4-4 Resistive L-G fault AG. (a) Fault circuit at fault point (b) Sequence network connection [100]

To eliminate the influence of unknown quantity $\dot{I}_f$, one should first analyze the fault networks considering the FCG's short-circuit models derived in section 2.1 of chapter 2. Figure 4-4 depicts the equivalent circuit at fault point and the connection of sequence component networks during a resistive L-G fault AG. Z_{T} represents the impedance of the collector system (e.g. the step-up transformer).

From Figure 4-4, one can see that the fault currents flowing into fault point F satisfies [100],

$$\dot{I}_{1f} = \dot{I}_{2f} = \dot{I}_{0f} = \frac{\dot{I}_f}{3} \tag{4.9}$$

In addition, the negative and zero sequence component networks in Figure 4-4 (b) are the passive circuits [100]. Based on this, one can find the following current distribution relationships between the fault current $\dot{I}_s$ and $\dot{I}_f$ in these two sequence systems, which meets [100],

$$\dot{I}_{2s} = \dot{I}_{2f} \cdot D_2 , \quad D_2 = \frac{(1-m)Z_2 + Z_{2r}}{Z_{2T} + Z_2 + Z_{2r} + 1/Y_{2\mathrm{FCG}}} \tag{4.10}$$

$$\dot{I}_{0\mathrm{s}} = \dot{I}_{0f} \cdot D_0 , \quad D_0 = \frac{(1-m)Z_0 + Z_{0r}}{Z_{0T} + Z_0 + Z_{0r}} \tag{4.11}$$

where $D_{2,0}$ represent the current distribution factors in the negative and zero sequence circuits.

Substituting (4.9)-(4.11) into the impedance tilting angle equation (4.8), it yields,

$$\theta_{AG} = -angle\left\{\left[\frac{\dot{I}_{1s}}{\dot{I}_{0s}} + (1 + K_0)\right] \cdot D_0 + D_2\right\} \tag{4.12}$$

or

$$\theta_{AG} = -angle\left\{\left[\frac{\dot{I}_{1s} + \dot{I}_{2s}}{\dot{I}_{0s}} + (1 + K_0)\right] \cdot D_0\right\} \tag{4.13}$$

Note that the expressions of impedance tilting angle in (4.12) and (4.13) are equivalent inherently. The distinction focuses on the utilization of different current distribution relationships. Now, the impedance tilting angle during fault AG can be estimated with the measurable fault information of the relay only.

For L-L fault, e.g. fault BC, the impedance measurement equation is revised as,

$$Z_{BC} = mZ_1 + \frac{\dot{U}_{fbc}}{\dot{I}_{Sbc}} \tag{4.14}$$

Similar to Figure 4-4, the equivalent circuit at the fault point and the sequence network connection during a resistive L-L fault BC are shown in Figure 4-5.

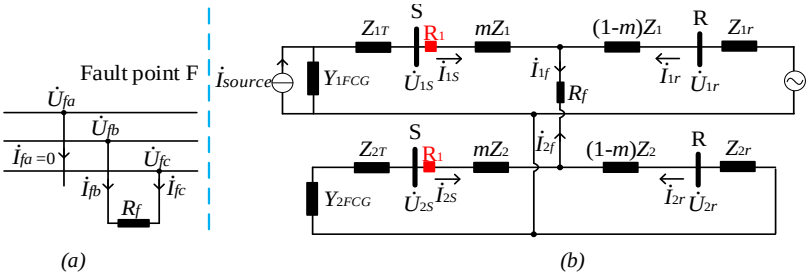

Figure 4-5 Resistive L-L fault BC. (a) Fault circuit at fault piont (b) Sequence network connection

From Figure 4-5, the boundary conditions of L-L fault BC, including the current $\dot{I}_{sbc}$ at relay point, the fault voltage $\dot{U}_{fbc}$, and fault current $\dot{I}_f$ at fault point, can be obtained as [100],

$$\dot{I}_{sbc} = \dot{I}_{sb} - \dot{I}_{sc} = (\alpha - \alpha^2) \cdot (\dot{I}_{2s} - \dot{I}_{1s}) \tag{4.15}$$

$$\dot{U}_{fbc} = \dot{I}_{fb} \cdot R_f = (\alpha^2 \cdot \dot{I}_{1f} + \alpha \cdot \dot{I}_{2f}) \cdot R_f \tag{4.16}$$

$$\dot{I}_{1f} + \dot{I}_{2f} = 0, \dot{I}_{0f} = 0 \tag{4.17}$$

where α has the same definition with the one in Figure 2-1.

Substituting (4.15)-(4.17) and the negative sequence current distribution relationship in (4.10) into (4.14), the ITA under the L-L fault BC can be expressed as,

$$\theta_{BC} = -angle\left[\left(1 - \frac{\dot{I}_{1s}}{\dot{I}_{2s}}\right) \cdot D_2\right] \tag{4.18}$$

For L-L-G fault, e.g. BCG, the impedance measurement equation (4.14) is also valid. Since the fault ring (the red curve) for fault BCG displayed in Figure 4-6 (a) is unified with that of L-L fault BC in Figure 4-5 (a). From Figure 4-6, one will obtain the following boundary conditions of a resistive L-L-G fault BCG [100],

$$\dot{U}_{fb} - \dot{I}_{fb} \cdot R_f = \dot{U}_{fc} - \dot{I}_{fc} \cdot R_f = \dot{I}_f \cdot R_g \tag{4.19}$$

$$\dot{I}_{fa} = \dot{I}_{1f} + \dot{I}_{2f} + \dot{I}_{0f} = 0 \tag{4.20}$$

From (4.14)-(4.15), (4.19)-(4.20), and the current distribution relationships in (4.10) and (4.11), the ITA for the L-L-G fault BCG can also be calculated,

$$\theta_{BCG} = -angle\left[\left(1-\frac{\dot{I}_{1s}}{\dot{I}_{2s}}\right)D_X^*\right], \qquad D_X^* = conjugate\left(\frac{2}{D_2}+\frac{\dot{I}_{0s}}{\dot{I}_{2s}\cdot D_0}\right) \tag{4.21}$$

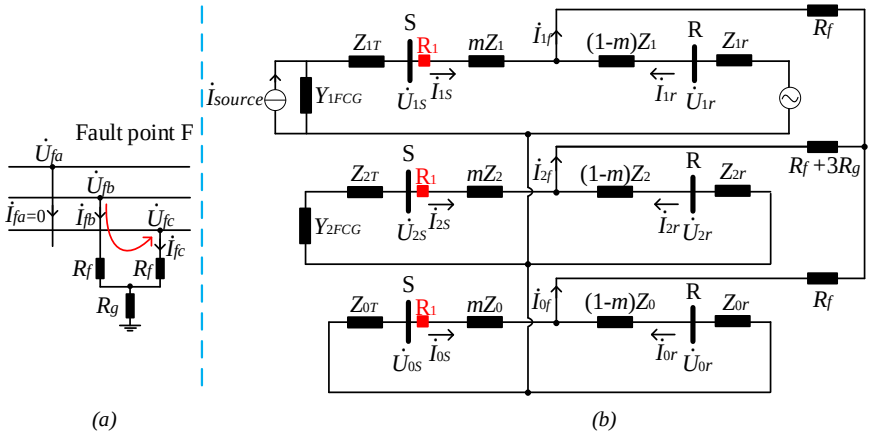

Figure 4-6 Resistive L-L-G fault BCG. (a) Fault circuit at fault piont (b) Sequence network connection

4.2.3. PROTECTION IMPLIMENTATION & PARAMETER INITIALIZATION

As the flowchart of ITA-21 displayed in Figure 4-7, the procedure in the detection of asymmetrical faults concludes five steps:

1) Fault detection from the start unit and fault phase selection in the distance relay.
2) If symmetrical faults occur, jump to step 5). Otherwise, set the ITA-21 scheme.
3) Compute the ITA θ_{Imp}^* by (4.3), and compute θ_{Imp} according to (4.12) (or (4.13)), (4.18), and (4.21).
4) Detect internal (or boundary) fault using operating criterion (4.6).
5) Run the conventional impedance-based distance protection.

In step 2), the ITA θ_{Imp} adopts the parameter m in the calculation of current distribution factors D_0 and D_2. However, the fault distance m is unknown.

Functionally, one knows that:

1) ITA-21 is used to detect the internal/external faults, rather than accurately calculate all fault positions on the line.
2) The high accuracy for the fault detection at the protective boundary can maintain the reliability of ITA-21.

From these considerations, m is set as the zone 1 length.

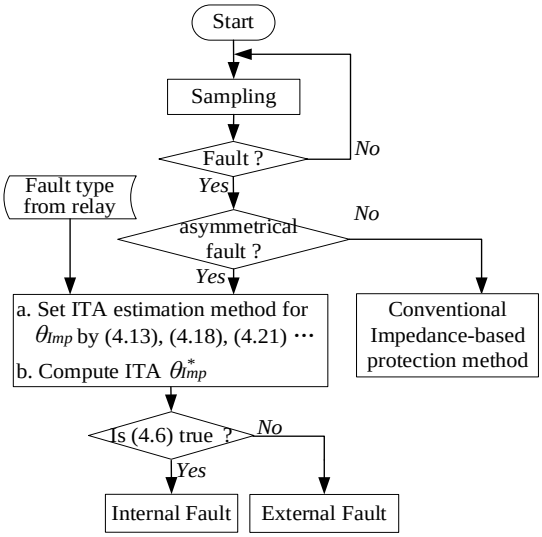

Figure 4-7 Flowchart of the proposed ITA-21 scheme.

4.3. CASE STUDY

The test system connecting FCG-based plant in Figure 4-8 is adopted for the simulation validation, where FCGs operate in the DSC strategy of Figure 2-2. As illustrated in Figure 4-8, zone 1 of relay R_1 covers 80% length of the protected line L1, while the zone 2 reaches 50% length of the downstream line L2-1. The extra link L2-2 is to simulate the meshed transmission network. Test system is modelled in DIgSILENT/ PowerFactory. In this software, the equivalent grid uses a model of a synchronous generator in simplified form for dynamic simulation [118]. Detailed parameters of the equivalent grid are listed in Table A-6. Parameters of other electrical components, e.g. transformer, transmission line are the same as in Figure 2-16. In the following simulations, the fault distance is the length of line from relay location to fault point (in per-unit value), where the base-value is the entire length of protected line, i.e. 50 km. In the test system, different fault positions, are considered. In detail,

1) $F1$ and $F2$ represent the internal fault positions, i.e. 0.1 p.u. and 0.7 p.u. away from terminal *S*.
2) $F3$ represents the zone 1 boundary fault position, i.e. 0.8 p.u. away from terminal *S*.
3) $F4$ and $F5$ are external fault positions, i.e. 0.9 p.u. and 1.0 p.u. away from terminal *S*.

4) $F6$ is another external fault position located on the downstream line (zone 2 end), i.e. 1.1 p.u. away from terminal *S*.

The voltage and current data at the relay terminal are sampled with a rate of 200 samples per cycle. The proposed algorithm is implemented in Matlab.

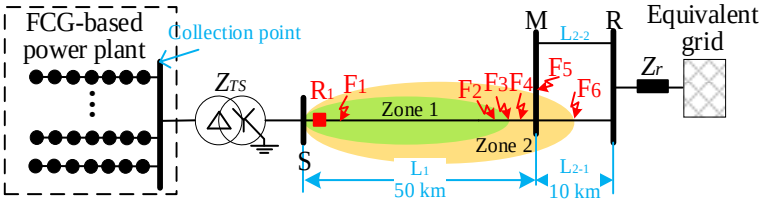

Figure 4-8 Test system connecting FCG-based plant

4.3.1. FAULT CONDITION OF CWIT

As mentioned in section 4.1.1, bulk active power generation from the FCG-based plant during grid faults can lead to the clockwise tilt of apparent impedance measured by the distance relay at the same side, which probably causes the relay over-reach. To simulate such fault conditions, the active current regulation of FCG follows (2.8) during faults, while the regulating parameters of the reactive current components as well as the outputting limits are given in Table 4-1.

TABLE 4-1 PARAMETERS OF THE CURRENT REGULATION FOR THE DSC DURING LVRT PEROID

Control Parameters	K_{v1}	K_{v2}	I_{qg}^{lim}	I_{g}^{lim}
Value (p.u.)	2.5	2	1	1.2

In the case of different fault conditions (i.e. fault position and fault resistance), the typical asymmetrical faults, e.g. L-G fault AG, L-L fault BC, and L-L-G fault BCG, are simulated (faults occur at 0.2 s). Table 4-2 compares the performances of the proposed ITA-21 to those of the Con-21. For the former, the steady-state DITA θ_{diff} is given, while the latter approach is elaborated by the measured fault distance.

Firstly, the local line faults are considered, i.e. the columns '$F1$~$F5$' in Table 4-2. Except for the fault BCG at $F1$ ($R_f = 20\ \Omega$), the rest fault distances measured by Con-21 are smaller than the real values at corresponding fault positions, threatening the reliability of Con-21 for remote faults. Specific to those faults occurring at $F3$, $F4$ and $F5$, measured fault distances are even smaller than the zone 1 length (0.8 p.u.), namely, Con-21 is at the risk of over-reach. In contrast to Con-21, the proposed ITA-21 performs the high reliability for all tested faults. For all external faults occurring at $F4$ and $F5$, θ_{diff} are negative. For all internal faults at $F1$ and $F2$, θ_{diff} are positive.

And, θ_{diff} tends to zero for boundary faults at $F3$. According to criterion (4.6), one knows that the fault status can be detected correctly. From the table, one can also see that the fault resistance can heavily affect the over-reaching level of Con-21. Generally speaking, the larger the fault resistance is, the worse the relay over-reach will occur. However, ITA-21 still performs enough reliability for those high resistive faults.

TABLE 4-2 COMPARISON OF ITA-21 WITH CON-21, IN THE CASE OF CWIT

Condition		**Methods**		**Fault point**					
Type	R_f/Ω			***F1***	***F2***	***F3***	***F4***	***F5***	***F6***
AG	5	Con-21	$dis.$	0.087	0.604	0.674	0.733	0.769	0.869
		ITA-21	θ_{diff}	1.306	0.186	-0.000	-0.134	-0.215	-0.348
	20	Con-21	$dis.$	0.050	0.409	0.429	0.422	0.374	0.362
		ITA-21	θ_{diff}	0.658	0.063	-0.000	-0.053	-0.097	-0.148
	50	Con-21	$dis.$	-0.036	0.156	0.143	0.108	0.044	0.008
		ITA-21	θ_{diff}	0.366	0.039	0.000	-0.037	-0.073	-0.106
	100	Con-21	$dis.$	-0.128	-0.039	-0.058	-0.092	-0.142	-0.171
		ITA-21	θ_{diff}	0.259	0.031	0.000	-0.031	-0.065	-0.091
BC	5	Con-21	$dis.$	-0.266	0.171	0.244	0.325	0.422	0.626
		ITA-21	θ_{diff}	0.617	0.085	0.001	-0.074	-0.136	-0.277
	10	Con-21	$dis.$	-0.330	0.229	0.346	0.376	0.370	0.420
		ITA-21	θ_{diff}	0.456	0.057	0.002	-0.050	-0.096	-0.177
	20	Con-21	$dis.$	-0.147	0.106	0.106	0.096	0.071	0.089
		ITA-21	θ_{diff}	0.320	0.042	0.001	-0.037	-0.073	-0.120
BCG	5	Con-21	$dis.$	-0.134	0.193	0.269	0.358	0.476	0.680
		ITA-21	θ_{diff}	0.698	0.084	0.001	-0.070	-0.128	-0.265
	20	Con-21	$dis.$	0.342	0.225	0.217	0.201	0.172	0.183
		ITA-21	θ_{diff}	0.321	0.037	0.001	-0.030	-0.059	-0.102
	50	Con-21	$dis.$	-0.170	-0.154	-0.160	-0.170	-0.185	-0.184
		ITA-21	θ_{diff}	0.213	0.026	0.001	-0.025	-0.052	-0.079
	100	Con-21	$dis.$	-0.409	-0.315	-0.310	-0.307	-0.308	-0.307
		ITA-21	θ_{diff}	0.179	0.024	0.000	-0.025	-0.053	-0.074

Intuitively, Figure 4-9 displays the dynamic results of both conventional and new proposed protection methods for different resistive fault AG, where the scenarios of R_f at $50\ \Omega$ and $100\ \Omega$ correspond to two of the tests in column '$F4$' of Table 4-2. Besides, a higher resistive fault scenario of R_f at $300\ \Omega$ is also included. The dynamic results accord with the above analysis on fault resistance. Besides, the proposed ITA-21 possesses a similar convergence speed with that of Con-21, which guarantees the feasibility of the new approach.

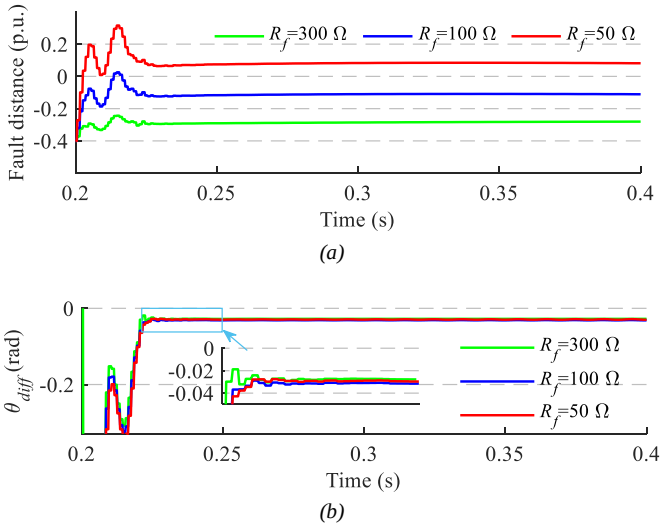

Figure 4-9 Fault AG located at F4, in the case of different fault resistances. (a) Measured fault distances of Con-21 (b) DITA θ_{diff}

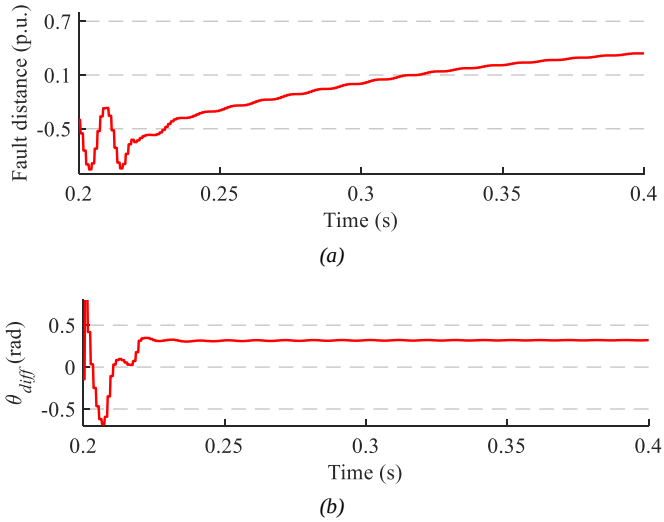

Figure 4-10 Fault BCG located at F1, in the case of R_f = 20Ω . (a) Measured fault distances of Con-21 (b) DITA θ_{diff}

Figure 4-10 depicts the dynamic results of two protection methods for fault BCG ($R_f = 20\ \Omega$) at $F1$, corresponding to the test in column '$F1$' of Table 4-2. In this test, the fault distance measured by Con-21 does not converge, and is finally larger than

the real fault distance. However, the new ITA-21 shows more reliable performance, as DITA θ_{diff} converges rapidly.

In the above content, mainly the local line faults are discussed. Simulation results prove that Con-21 is at the risk of malfunction during external faults due to the relay over-reach, however, the proposed ITA-21 can detect all local line faults properly. Speaking of the reliability of distance protection, except for reliably distinguishing the faults on the local line, the relay should not trip when external faults on the downstream line occur, either.

From the listed scenarios in column '$F6$' of Table 4-2, one can see that Con-21 similarly measures much short fault distances compared to the real distance of 1.1 p.u. at $F6$. Except for the fault AG ($R_f = 5\ \Omega$), the measured fault distances for other fault scenarios are all smaller than the zone 1 threshold 0.8 p.u., i.e. Con-21 faces the malfunction risk. However, the proposed ITA-21 is still proven to be effective to detect these external faults on the downstream line. As listed in column '$F6$', negative DITA θ_{diff} are calculated, finally. Take the scenarios of $R_f = 5\ \Omega$ in column '$F6$' of Table 4-2, for example. Figure 4-11 illustrates the dynamic results of both conventional and new protection methods for these three asymmetrical faults. Compared to Con-21, one can see that ITA-21 also performs excellent convergent process for these downstream line faults.

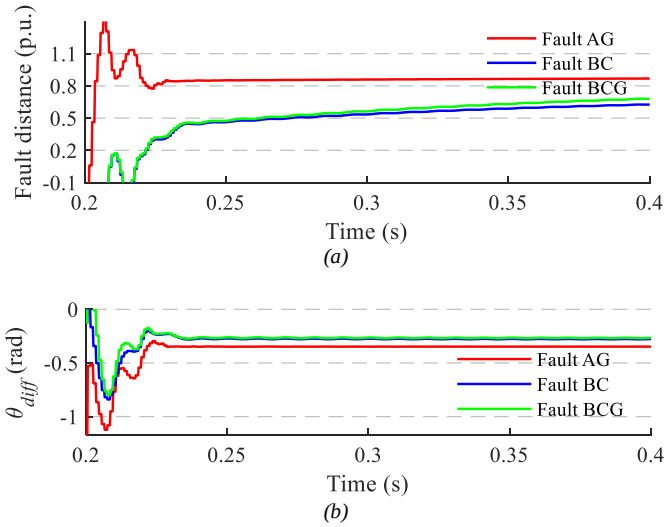

Figure 4-11 Different asymmetrical faults at F6, in the case of $R_f = 5\Omega$. (a) Measured fault distances of Con-21 (b) DITA θ_{diff}

From the above tests, one knows that the proposed ITA-21 can distinguish the internal and external faults reliably. The new protection method is unaffected under the CWIT condition.

4.3.2. FAULT CONDITION OF COUNTER-CWIT

As the counter-CWIT phenomenon discussed in section 4.1.2, Con-21 probably suffers the under-reaching risk when the active power generation from FCG-based plant has a tiny level during grid faults. To simulate such fault condition, a limiter for the active current output in the positive sequence control loop is added in the DSC system.

In detail, the following FCG regulation strategies are adopted in the study:

1) For L-G fault, e.g. fault AG, the active current output in the positive sequence loop is limited to 0.1 p.u., while it is limited to 0.3 p.u. for interphase faults, e.g. L-L fault BC and L-L-G fault BCG.
2) The regulation of the reactive current components are the same as that in section 4.3.1 (Table 4-1).

Since the zero-sequence current is dominant in the calculation of L-G apparent impedance, a smaller current limiter, in the case of L-G fault situation, is adopted compared to the L-L fault situation.

Under such FCG regulation strategies, Table 4-3 compares the performances of the proposed ITA-21 to that of Con-21, where different fault positions and fault resistances are considered. From Table 4-3, one can see that the fault distances measured by Con-21 are larger than the real values at corresponding fault positions, which probably affects the reliability of Con-21. Specific to certain scenarios of columns $F1$, $F2$ and $F3$ in Table 4-3, one can see that the measured fault distances can be larger than the zone 1 threshold 0.8 p.u., namely, Con-21 is at the risk of relay under-reach. In contrast to Con-21, the proposed ITA-21 performs high reliability for all tested faults, referring to criterion (4.6).

TABLE 4-3 COMPARISON OF ITA-21 WITH CON-21, IN THE CASE OF COUNTER-CWIT

Condition		**Methods**		**Fault point**					
Type	R_f/Ω			$F1$	$F2$	$F3$	$F4$	$F5$	$F6$
AG	5	Con-21	$dis.$	0.116	0.734	0.847	0.970	1.123	1.412
		ITA-21	θ_{diff}	1.372	0.166	0.000	-0.104	-0.157	-0.272
	10	Con-21	$dis.$	0.137	0.777	0.899	1.040	1.226	1.549
		ITA-21	θ_{diff}	0.994	0.083	0.000	-0.056	-0.090	-0.157
	20	Con-21	$dis.$	0.160	0.822	0.950	1.100	1.303	1.632
		ITA-21	θ_{diff}	0.571	0.043	-0.000	-0.032	-0.057	-0.098

BC	5	Con-21	$dis.$	0.116	0.834	0.985	1.160	1.368	1.671
		ITA-21	θ_{diff}	0.743	0.076	0.000	-0.059	-0.106	-0.232
	10	Con-21	$dis.$	0.359	1.262	1.448	1.651	1.872	2.146
		ITA-21	θ_{diff}	0.438	0.044	0.000	-0.034	-0.061	-0.129
	20	Con-21	$dis.$	0.918	1.732	1.841	1.920	1.947	2.080
		ITA-21	θ_{diff}	0.252	0.025	0.001	-0.021	-0.041	-0.080
BCG	5	Con-21	$dis.$	0.355	0.925	1.088	1.286	1.541	1.847
		ITA-21	θ_{diff}	0.821	0.072	0.000	-0.055	-0.093	-0.216
	10	Con-21	$dis.$	0.904	1.511	1.731	1.999	2.340	2.638
		ITA-21	θ_{diff}	0.431	0.038	0.000	-0.027	-0.045	-0.109
	20	Con-21	$dis.$	1.778	2.345	2.492	2.627	2.725	2.852
		ITA-21	θ_{diff}	0.223	0.019	0.001	-0.014	-0.026	-0.062

Considering the L-G fault AG occurring at point $F2$, Figure 4-12 depicts the dynamic results of both Con-21 and ITA-21. From Figure 4-12 (a), one can see that the fault distances measured by Con-21 converge to different steady-state values under different resistive fault conditions. In the case of $R_f = 20\ \Omega$, the fault distance is larger than the threshold 0.8 p.u., namely, an external fault is finally detected. The proposed ITA-21, by contrast, will stably detect as internal faults in all three scenarios, as depicted in Figure 4-12 (b).

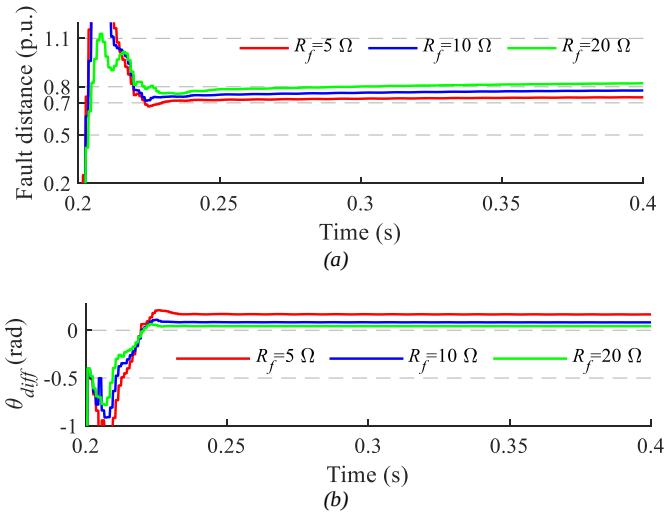

Figure 4-12 Fault AG located at F2, in the case of different fault resistances. (a) Measured fault distances of Con-21 (b) DITA θ_{diff}

Figure 4-13 corresponds to the tested fault BCG at point $F1$ in Table 4-3. Although the faults approach the relay location, Con-21 still faces the malfunction risk when R_f increases. Similarly, ITA-21 is still effective.

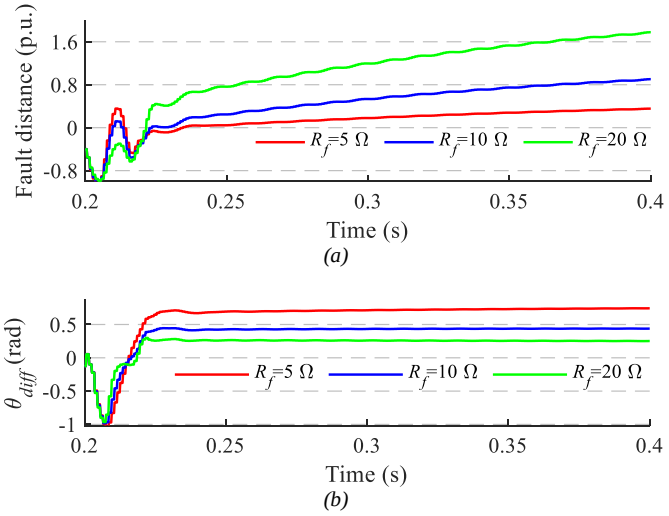

Figure 4-13 Fault BCG located at F1, in the case of different fault resistances. (a) Measured fault distances of Con-21 (b) DITA θ_{diff}

The above tests prove that ITA-21 is unaffected under the condition of counter-CWIT, either.

4.3.3. INFLUENCE OF BOLTED FAULTS

The above ITA-21 has the operating dead zone, due to the fact of ITA θ^*_{Imp} probably fluctuating during bolted boundary faults. For bolted faults, it is easy to see that the modulating impedance ΔZ tends to zero in theory (eq. (4.1)). In other words, distance relay measures the line impedance only. Thus, Con-21 is suggested within the dead zone. To detect the dead zone, a relative resistance-based method is introduced. As shown in Figure 4-14, the shaded area denotes the dead zone and the relative resistance-based criterion is expressed as,

$$\Delta R = real(Z_{app}) - \frac{imaginary(Z_{app})}{imaginary(Z)} real(Z) < R_{threshold} \tag{4.22}$$

where $R_{threshold}$ denotes the lower critical threshold.

Considering the boundary fault AG at $F3$ under CWIT condition, different small resistive scenarios are tested to elaborate the performance of relative resistance-based criterion. In Figure 4-15, the resistance variable ΔR shows clear increment against the

increasing fault resistance, proving the feasibility of the dead zone detecting criterion based on relative resistance.

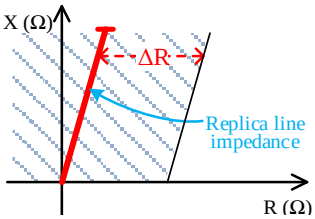

Figure 4-14 Graphical representation of dead zone in the impedance plane.

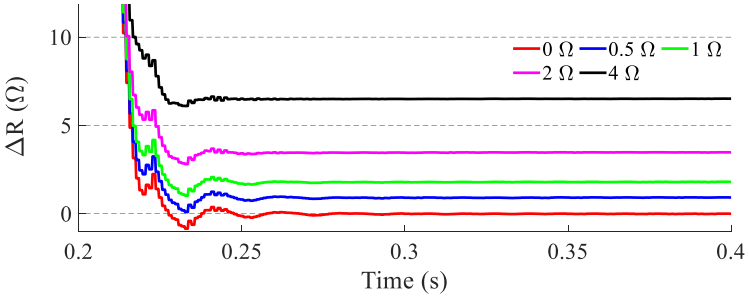

Figure 4-15 ΔR variation for fault AG located at F3 when fault resistance increases.

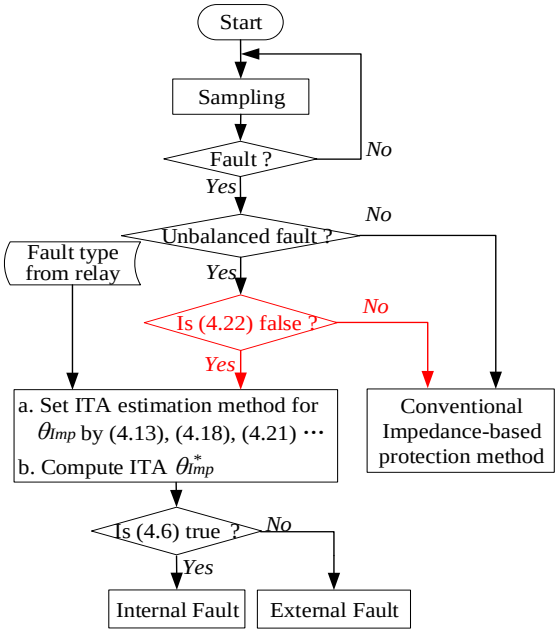

Figure 4-16 Flowchart of the proposed ITA-21 scheme

Considering the above dead zone issue, the flowchart of the ITA-21 scheme is revised as Figure 4-16. In detail, a new step is added after step 2) in the procedure of section 4.2.3,

Detect the dead zone. If criterion (4.22) is fulfilled, go to step 5). Otherwise, continue step 3) (same as before).

4.3.4. ADAPTABILITY FOR FCGS DEPLOYED WITH BCC

For the FCGs deployed with BCC strategy, ITA-21 is valid during L-G faults only. In the context of BCC method, FCG-based plant does not inject any negative sequence current during asymmetrical faults. Thus, one can directly revise the expression in (4.13) as [117],

$$\theta_{AG} = -\angle\left(\frac{\dot{I}_{1S}}{\dot{I}_{0S}} + (1 + K_0)\right) \cdot D_0 \tag{4.23}$$

For other asymmetrical faults (e.g. BC and BCG), ITA-21 cannot work, because the parameter D_2 is not applicable to the estimation of θ_{Imp}. To tackle such application limit, the estimating methods for fault current angle of $\dot{I}_f$ for fault BC and BCG mentioned in [86-87, 117] are adopted.

$$\theta_{BC} = \angle\frac{\dot{I}_{fbc}}{\dot{I}_{sbc}} = \angle\frac{\dot{I}_{1f} - \dot{I}_{2f}}{\dot{I}_{1s} - \dot{I}_{2s}} = \angle\frac{\dot{U}_{2f} \approx \dot{U}_{2s}}{\dot{I}_{1s} \cdot (Z_{1r} + (1-m)Z_1)} \tag{4.24}$$

$$\theta_{BCG} = \angle\frac{\dot{I}_{fb} + \dot{I}_{fc}}{\dot{I}_{sb} + \dot{I}_{sc} + 2k_0\dot{I}_{s0}} = \angle\frac{3\dot{I}_{0f}}{\dot{I}_{0s}(2+2K_0) - \dot{I}_{1s}} = -\angle\left((2 + 2K_0) - \frac{\dot{I}_{1s}}{\dot{I}_{0s}}\right) \cdot D_0 \tag{4.25}$$

By adopting (4.23) and the newly deduced (4.24)-(4.25), ITA-21 will be capable of dealing with the asymmetrical faults in the context of BCC strategy deployed in FCG-based plant. As mentioned at the end of section 2.1, if the negative sequence control loop is disabled, FCG will run in the BCC strategy. Here, parameter K_{v2} for the regulation of negative sequence current in Table 4-1 is simply set to zero.

Under such FCG regulation strategies, Table 4-4 compares the performances of ITA-21 to that of Con-21, under the CWIT condition. From Table 4-4, one can see that the measured fault distances by Con-21 are generally smaller than the real values, except for the fault BCG at point $F6$ ($R_f = 5\ \Omega$). Take all the faults AG and BC located at points $F3{\sim}F6$, for example. Since the measured fault distances are all smaller than the zone 1 length (0.8 p.u.), Con-21 always faces the over-reaching problem. For fault BCG, Con-21 is mainly at the over-reaching risk for the high resistive fault scenarios (i.e. $R_f = 100\ \Omega$). In contrast, ITA-21 shows excellent performance for all tested faults, referring to criterion (4.6). Figure 4-17 depicts the tested fault BCG at point $F6$ in Table 4-4.

The tests in this section proves the effectiveness of ITA-21 when the BCC strategy is deployed in the local FCG-based plant.

TABLE 4-4 COMPARISON OF ITA-21 WITH CON-21, IN THE PRESENCE OF BCC IN FCG

Condition		Methods		Fault point					
Type	R_f/Ω			***F1***	***F2***	***F3***	***F4***	***F5***	***F6***
AG	5	Con-21	$dis.$	0.075	0.574	0.637	0.683	0.699	0.785
		ITA-21	θ_{diff}	1.258	0.172	-0.000	-0.122	-0.195	-0.323
	100	Con-21	$dis.$	-0.183	-0.102	-0.121	-0.153	-0.200	-0.227
		ITA-21	θ_{diff}	0.249	0.030	-0.000	-0.030	-0.063	-0.088
BC	5	Con-21	$dis.$	-0.354	-0.075	-0.063	-0.067	-0.090	0.009
		ITA-21	θ_{diff}	0.554	0.075	0.000	-0.065	-0.119	-0.259
	20	Con-21	$dis.$	-0.847	-0.699	-0.686	-0.673	-0.656	-0.602
		ITA-21	θ_{diff}	0.259	0.033	0.000	-0.031	-0.062	-0.108
BCG	5	Con-21	$dis.$	0.099	0.686	0.780	0.872	0.960	1.126
		ITA-21	θ_{diff}	1.640	0.591	0.000	-0.389	-0.546	-0.758
	100	Con-21	$dis.$	0.088	0.423	0.435	0.422	0.367	0.337
		ITA-21	θ_{diff}	0.533	0.051	-0.000	-0.043	-0.081	-0.117

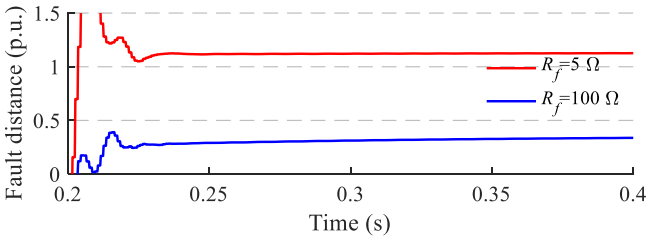

(a)

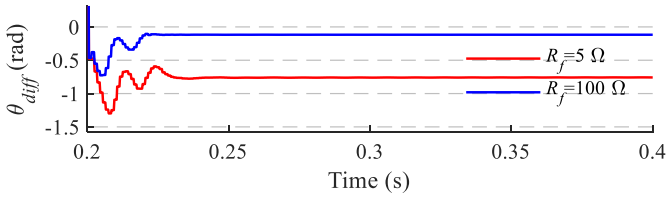

(b)

Figure 4-17 Fault BCG located at F6, in the case of different fault resistances. (a) Measured fault distances of Con-21 (b) DITA θ_{diff}

4.4. DISCUSSION

Aiming at the impedance tilt seen by Con-21 positioned at the FCG-based plant side during resistive grid faults in section 2.2.2, the concept of ITA is introduced, and its inherent features are first analyzed in this chapter. After that, an ITA-21 scheme is proposed and the effectiveness of the new protection method is elaborated by the study cases under the fault conditions of CWIT and counter-CWIT. Simulation results prove that ITA-21 is capable of protecting the transmission line emanating from the FCG-based plant. The **properties** of ITA-21 are concluded as:

1) ITA-21 adopts the inherent tilting features of apparent impedance to detect the grid faults, which shows no traditional over- or under-reaching problems faced by Con-21 method.
2) ITA-21 in fact works for the detection of resistive grid faults. For the operating dead zone issue when a bolted grid fault occurs, the resistance variable-based dead zone detection method is introduced to secure the operation of ITA-21.

In theory, the estimation of ITA θ_{Imp} includes: Step 1, substitute the positive sequence current component in the fault current $\dot{I}_f$ by the negative or zero sequence components of $\dot{I}_f$ based on the fault boundary conditions. Step 2, replace the negative or (and zero) sequence current component(s) in $\dot{I}_f$ with the sequence current component(s) at relay end by using the current distribution factors in negative or (and) zero sequence systems. Thus, the **application limits** of ITA-21 are,

1) ITA-21 cannot apply to the 3PH grid faults, since there is no valid distribution factor(s) (i.e. D_0 or D_2) to eliminate the influence of fault current $\dot{I}_f$ during such fault condition.
2) ITA-21 is not suitable for the L-G (or L-L-G) faults in the ungrounded medium (or low) voltage system, either. Because ITA-21 needs to adopt the current distribution factor in the zero-sequence loop to estimate ITA θ_{Imp} during these faults.

One thing should be mentioned, the selection of a constant parameter m representing the zone 1 length will lead to the estimation error of ITA θ_{Imp} for other fault positions. Since the new protection setting method in Chapter 5 also adopts the ITAs θ_{Imp} and θ_{Imp}^{*}, the qualitative analysis on the estimation error of θ_{Imp} will be given along in section 5.2.4.

CHAPTER 5. ADAPTIVE TILT SETTING OF THE POLYGONAL DISTANCE RELAY IN THE LINE EMANATING FROM FCG-BASED PLANT

Aiming at the same malfunction risk of distance protection in the transmission line emanating from FCG-based plant, a new adaptive zone top-line tilt setting scheme of distance protection with the application of ITA is presented in this chapter. Different from the ITA-21 scheme presented in chapter 4, the new tilt setting scheme works by active compensation for the influence caused by the impedance tilt.

5.1. TILT SETTING OF POLYGONAL ZONE TOP-LINE (PZTL)

In fact, because of the influence of load-transfer on the line, relay over-reach under the CWIT condition is frequent for the distance protection deployed at the power exporting end. The modern numerical distance relay (e.g. model 7SA522, 7SA6 from siemens) had incorporated the relevant tilt rules of polygonal zone (working for the top-line) to overcome such over-reaching problem in SG-dominated grid during resistive faults, up to maximum line loading [104]. In this chapter, the adaptability of the existing tilt setting method of PZTL is first analyzed.

5.1.1. EXISTING TILT SETTING METHOD OF PZTL

Since the existing tilt setting method of PZTL is based on a remote fault at the protected line end. One needs to reduce the network to a 'two-machine' system, firstly.

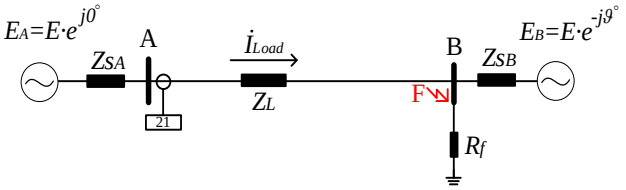

Figure 5-1 Transmission line with two side infeed

Take the L-G fault AG at terminal B in the system of Figure 5-1, for example. Reference [104] presents the derivation of apparent impedance seen at the relay location (terminal A) during L-G faults, but the final impedance expression is not simple in format. To facilitate the following adaptability analysis, the more universal derivation of the same apparent impedance from [82] is cited here. In contrast to [104],

both fault position and fault resistance are treated as variables in [82], so that the whole quadrilateral relay boundary can be determined. If the fault position at the end of protected line is considered only, the deduced apparent impedance in [82] will be equivalent to that in [104]. In detail,

The pre-fault load current and the phase A voltage at fault point respectively satisfies,

$$\begin{cases} \dot{I}_{Load} = \dfrac{E_A - E_B}{Z_{SA} + Z_L + Z_{SB}} \\ \dot{U}_{fa.pre} = E_A - \dot{I}_{Load}\left(Z_{SA1} + Z_{L1}\right) \end{cases} \tag{5.1}$$

where pre-fault potentials of the two-sided sources meet $E_B = E_A \cdot exp\left(-j \cdot \vartheta^{\circ}\right)$.

For L-G fault AG, based on the superposition principle and the symmetrical component method, the total current and the phase A voltage at relay location, as well as the current flowing into fault point are respectively,

$$\begin{cases} \dot{I}_{Aa} = \dot{I}_{fAa} + \dot{I}_{Load} \\ \dot{U}_{Aa} = \sum \dot{U}_{1,2,0A} = Z_L\left(\dot{I}_{1fA} + \dot{I}_{Load}\right) + Z_L \dot{I}_{2fA} + Z_{0L} \dot{I}_{0fA} + \dot{I}_f \cdot R_f \\ \dot{I}_{0f} = \dot{I}_{2f} = \dot{I}_{0f} = \dfrac{\dot{I}_f}{3} = \dfrac{\dot{U}_{fa.pre}}{Z_{sum} + 3R_f} \end{cases} \tag{5.2}$$

From (5.1) and (5.2), the L-G apparent impedance is further simplified as,

$$Z_{pha-E} = \frac{\dot{U}_{Aa}}{\dot{I}_{Aa} + 3k_0 \dot{I}_{0fA}} = Z_L + \Delta Z \tag{5.3}$$

where modulating impedance: $\Delta Z = \dfrac{3 \cdot R_f}{M_D + 2 \cdot M_1 + M_0(1 + 3 \cdot k_0)}$,

zero sequence compensation factor: $k_0 = \dfrac{Z_{0L} - Z_L}{3 \cdot Z_L}$,

distribution factor of component currents: $M_1 = \dfrac{\dot{I}_{1fA}(\dot{I}_{2fA})}{\dot{I}_{1f}} = \dfrac{Z_{SB}}{Z_{SA} + Z_L + Z_{SB}}$,

$M_0 = \dfrac{\dot{I}_{0fA}}{\dot{I}_{0f}} = \dfrac{Z_{0SB}}{Z_{0SA} + Z_{0L} + Z_{0SB}}$,

additional factor: $M_D = (3R_f + Z_{sum}) \dfrac{1 - e^{-j\vartheta}}{Z_{SB} + e^{-j\vartheta} \cdot (Z_{SA} + Z_L)}$,

sum of sequence impedance: $Z_{sum} = 2 \cdot \dfrac{(Z_{SA} + Z_L) \cdot Z_{SB}}{Z_{SA} + Z_L + Z_{SB}} + \dfrac{(Z_{0SA} + Z_{0L}) \cdot Z_{0SB}}{Z_{0SA} + Z_{0L} + Z_{0SB}}$,

Finally, the tilting angle can be determined as,

$$\alpha = angle(Z_{pha-E} - Z_L) = angle(\Delta Z) \tag{5.4}$$

Equation (5.4) indicates that, the modulating impedance ΔZ is the function of pre-fault transmission angle ϑ and fault resistance R_f. The tilt of PZTL can be then adjusted according to the angle calculated in (5.4) [104].

5.1.2. CHALLENGE ANALYSIS

The above tilt setting method of PZTL is built on the basis of two-sided infeeds being the equivalent Thevenin circuits, where the positive and negative sequence systems are deemed to be equivalent [117].

However, the modeling analysis of FCG in section 2.1 proves that FCG operates as the controlled current source when the outer loop controller is bypassed during grid faults [100]. The nonlinear control variation of PEC breaks the application premise of the superposition principle [117]. Neither can one find the current distribution factor in the positive sequence system [117]. In addition, the negative sequence impedance of FCG depends on the control parameter, which can be different from the positive sequence impedance during asymmetrical grid faults [117].

As a result, the above tilt setting method of PZTL is problematic for the distance relay on the line emanating from FCG-based plant. The newly adaptive tilt setting method of PZTL, suitable for the context of connecting FCG-based plant, is further studied in the following contents of this chapter.

5.1.3. ADAPTIVE TILT SETTING OF PZTL CONSIDERING FCG FAULT CONTROL

Actually, the tilting angle α in (5.4) reflects the angle of modulating impedance ΔZ, which is the same as the ITA θ_{Imp} defined in (4.2) of chapter 4. In contrast to α in (5.4), ITA θ_{Imp} is compatible with the FCG fault control, and suitable for all fault positions along the protected line (see the discussion regarding different asymmetrical grid faults in section 4.2.2).

Subsequently, one may reasonably infer that the influence of apparent impedance tilt can be avoided if the PZTL of distance relay tilts according to θ_{Imp}. Take the possible relay over-reach under the CWIT condition, for example. Figure 5-2 illustrates the representation of apparent impedance on complex plane during a possible external fault, in which the apparent impedance negatively tilts by an angle of θ_{Imp}, and locates in the protective zone under the initial (horizontal) condition of PZTL (see the dashed line marked in blue). If the PZTL adaptively tilts an angle of $\hat{\theta}_{Imp}$, e.g. set $\hat{\theta}_{Imp} = \theta_{Imp}$, the apparent impedance will correspondingly stay out of the protective zone (see the solid line marked in blue).

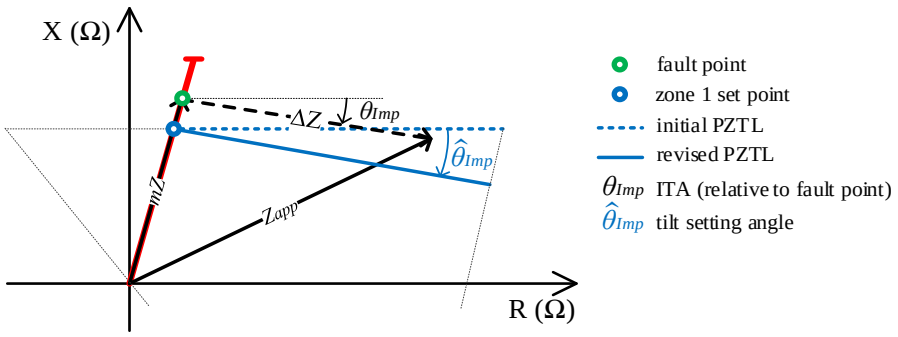

Figure 5-2 Graphical representation of adaptive tilting scheme of polygonal zone top-line

In addition, this angle θ_{Imp} can also reflect the tilting direction of apparent impedance (as it can be either positive or negative). Taking the counter-clockwise direction to be positive, θ_{Imp} will be positive under the condition of counter-CWIT. Under such condition, tilting the PZTL at this angle can also compensate for the possible under-reaching problem.

5.1.4. IMPLEMENTATION OF ADPATIVE TILT SCHEME OF PZTL

In practice, one do not need to adopt the new adaptive tilt setting scheme of PZTL for all faults, since only remote faults approaching the protective boundary may threaten the relay applying the initial (horizontal) PZTL setting [117]. For other fault positions, the initial (horizontal) reactance element setting does not affect the fault detection.

To improve the efficiency of the new setting scheme, one can activate the tilt setting of PZTL in certain risk areas only [117]. To do this, one need to identify the risk areas regarding different impedance tilt conditions, and build proper pickup criterions. Figure 5-3 illustrates the representations of apparent impedance on complex plane during different faults that may lead to the malfunction of distance relay.

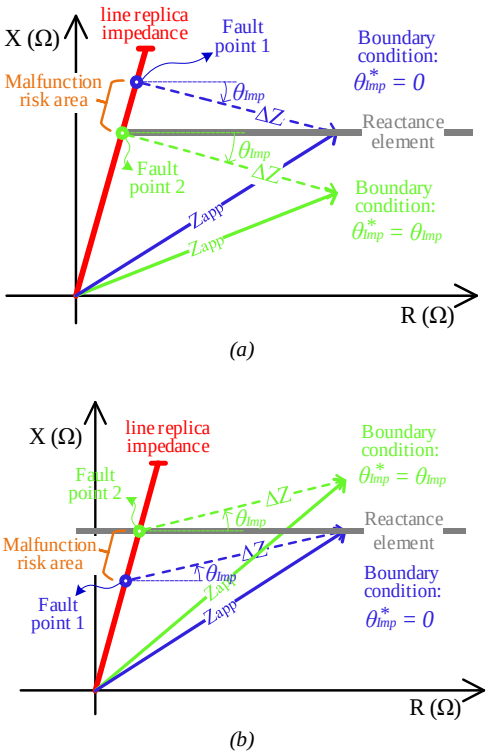

Figure 5-3 Malfunction risk areas under different impedance tilt conditions. (a) Under CWIT condition (b) Under counter-CWIT condition

In Figure 4-1, different representations of Z_{app} on impedance plane have been illustrated in the condition of CWIT. Based on this, one can clarify the possible external faults that may compromise the security of distance relay, as shown in Figure 5-3 (a). In the figure, two boundary conditions in the possible risk area are plotted. The condition marked in green denotes the fault located at the end of zone 1, while the one marked in blue denotes the external fault, i.e. apparent impedance locates on the reactance element. According to the qualitative angular relationship of θ_{Imp} to θ^*_{Imp}, the pickup criterion for the tilt setting of PZTL under the condition of CWIT is formulated as [117],

$$\theta_{Imp} \le \theta^*_{Imp} < 0 \tag{5.5}$$

Similarly, from the different representations of Z_{app} on impedance plane in Figure 4-2 under the counter-CWIT condition, one can also clarify the possible internal faults that may threaten the security of distance relay, as shown in Figure 5-3 (b). The boundary condition marked in green also denotes the fault located at the end of zone 1, however, the one marked in blue denotes the internal fault, i.e. apparent impedance

locates on the reactance element. Under such condition, the pickup criterion for the tilt setting of PZTL under the condition of counter-CWIT is formulated as [117],

$$\theta_{Imp} \geq \theta_{Imp}^{*} > 0 \tag{5.6}$$

Combining the pickup criteria in (5.5) and (5.6) with the dead zone detection of (4.22) in chapter 4, the implementing procedure of the adaptive tilt setting scheme of PZTL is illustrated in the flowchart of Figure 5-4. ζ has the same definition as that in (4.5).

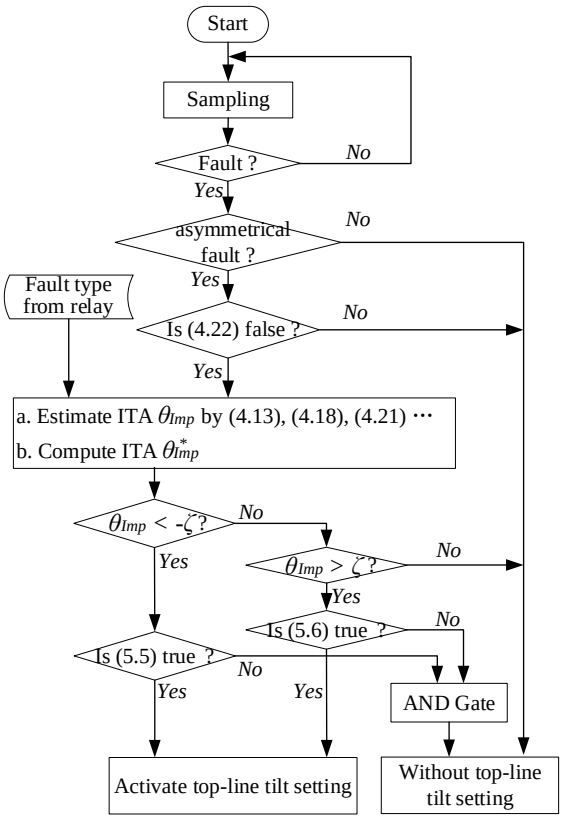

Figure 5-4 Flowchart of the adaptive tilt setting scheme of PZTL [117]

In detail, the implementing procedure concludes the following six steps:

1) Detect fault by start unit and select fault phase in the directional element.
2) If symmetrical fault is detected, jump to step 6). Otherwise, run the dead zone detection.
3) If the dead zone is detected, jump to step 6). Otherwise, estimate both θ_{Imp} and θ_{Imp}^{*}.

4) Judge the tilting direction of apparent impedance, if the normal condition is detected (referring to (4.5)), jump to 6). Otherwise, judge the pickup criterion (5.5) (or (5.6)).
5) If one of the pickup criteria for PZTL tilt setting is satisfied, tilt the PZTL by an angle $\hat{\theta}_{Imp}$ (i.e. $\hat{\theta}_{Imp} = \theta_{Imp}$).
6) Otherwise, adopt the horizontal PZTL setting.

For the calculation of θ_{Imp} in step 3), the parameter *m* included in current distribution factors D_0 and D_2 is initialized as the zone 1 length, keeping the same to that in the previous chapter.

Based on the above analysis, the dynamic performance of the adaptive tilt setting scheme of PZTL is investigated in the following section.

5.2. CASE STUDY

The transmission system emanating from FCG-based plant given in Figure 4-8 is adopted for the simulation validation. System configuration and detailed parameters are the same as before in section 4.3.

The adaptive tilt setting scheme of PZTL proposed in this chapter is based on the ITA θ_{Imp}, which is a critical angular variable in the ITA-21 in chapter 4. Thus, the fault scenarios in section 4.3 are not re-tested here, but further elaboration is given for specific fault scenarios from the perspective of the new approach of this chapter.

5.2.1. COMPENSATION OF RELAY OVER-REACH

Firstly, the performance of the adaptive tilt setting scheme of PZTL in the condition of CWIT is investigated (referring to the operation condition of FCG mentioned in section 4.3.1).

In Table 4-2, except for the fault BCG at $F1$ ($R_f = 20\ \Omega$), Con-21 always measures shorter fault distances for other fault scenarios (than their real distances), among which Con-21 is even at the risk of malfunction due to the relay over-reach for the faults located at $F3$~$F6$. In what follows, several fault scenarios in columns '$F3$~$F6$' of Table 4-2 are first discussed in detail.

Take the study for L-G fault AG located at $F4$ in Figure 4-9, for example. Figure 5-5 displays the simulation results of the adaptive tilt setting scheme of PZTL. From the dynamic curves of ITA θ_{Imp} and θ_{Imp}^{*} displayed in Figure 5-5 (a), one knows that the

pickup criterion (5.5) under the condition of CWIT is satisfied rapidly, regardless of the different R_f conditions. Correspondingly, the trajectories of measured impedance by relay R_1 are displayed in Figure 5-5 (b). Except for the initial PZTL, the revised PZTLs based on the steady-state θ_{Imp} under different R_f conditions are also plotted in Figure 5-5 (b). Clearly, relay R_1 will mal-operate due to the fact of over-reach if R_1 adopts the initial PZTL setting. However, the problem can be avoided if the revised PZTL setting is adopted. At the same time, one can also see that the adaptive tilt setting scheme of PZTL can effectively handle the high resistive fault condition.

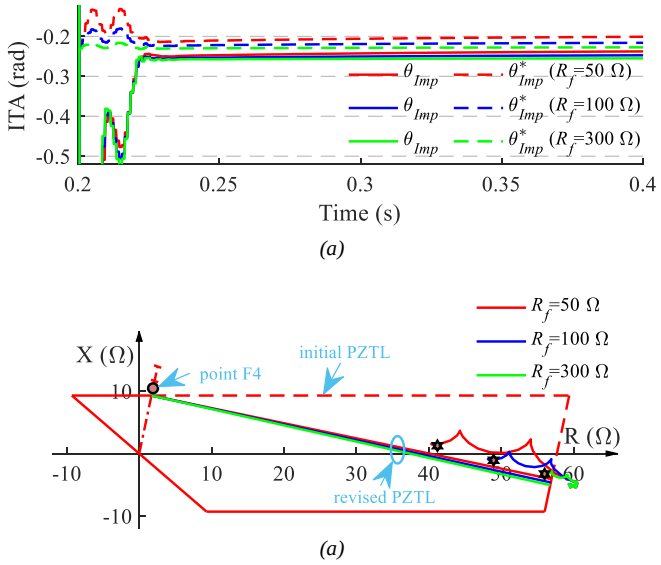

Figure 5-5 Fault AG at point F4, in the case of different fault resistances. (a) Dynamic ITAs (b) Impedance trajectories of Z_{app}^{AG}

One thing should be mentioned is that, the adaptive tilt setting scheme of PZTL is a kind of 'online' impedance tilt compensation method, which requires adjusting the PZTL tilt continuously during fault periods. The unstable compensation of the adaptive tilt setting scheme of PZTL probably causes the malfunction of the relay too. To better illustrate the dynamic performance of the adaptive tilt setting method of PZTL, one can examine the DITA θ_{diff} defined in (4.6). In fact, θ_{diff} reveals the convergence property of the new tilt setting method. As shown in Figure 4-9 (b), one can see that the DITA θ_{diff} under three resistive fault conditions gradually stabilize onto certain negative values after a short transient fluctuation. This proves that the compensation of the adaptive tilt setting scheme of PZTL for impedance tilt converges to be stable rapidly. Besides, the DITAs of other tested fault scenarios in chapter 4 also show a similar convergence property, which will be no longer discussed in the following simulation studies.

Under the CWIT condition, zone 1 element may also 'see' zone 2 faults on the down-stream line as internal faults. Here, two resistive faults ($R_f = 5\ \Omega$) located at the end of zone 2 are simulated, as displayed in Figure 5-6. For fault AG, θ^*_{Imp} stabilizes to be positive after the fault transient fluctuation, dissatisfying the pickup criterion (5.5) under the condition of CWIT, as depicted in Figure 5-6 (a). It means that the distance relay is capable of detecting this external fault under the initial PZTL condition. In Figure 5-6 (b), the location of apparent impedance for fault AG accords with the above analysis. Inversely, pickup criterion (5.5) is satisfied during the tested fault BCG (see the dynamic ITA curves in Figure 5-6 (a)). Correspondingly, one can see that the external fault BCG can be identified correctly when adopting the revised PZTL, as depicted in Figure 5-6 (b).

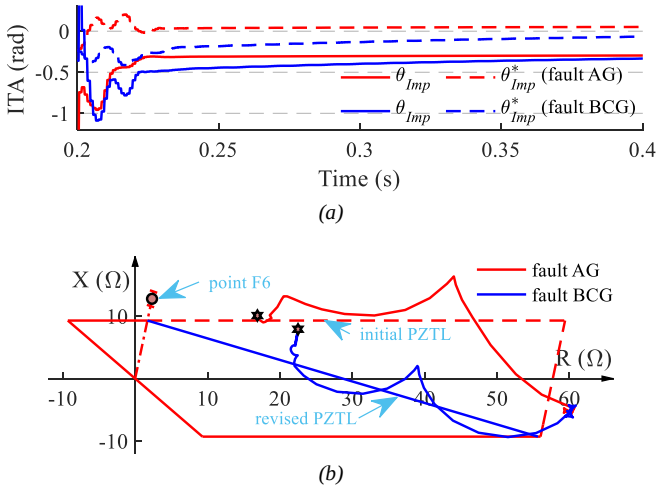

Figure 5-6 Fault AG and BCG at point F6, $R_f = 5\Omega$. (a) Dynamic ITAs (b) Impedance trajectories of Z^{AG}_{app} and Z^{BCG}_{app}

Actually, the detection accuracy of distance protection for boundary faults determines its reliability. In the below case, the L-L fault BC located at $F3$, i.e. protective boundary, is studied and results are displayed in Figure 5-7.

From Figure 5-7 (a), one can first see that the pickup criterion (5.5) under the CWIT condition is satisfied during the fault steady state. Correspondingly, the impedance trajectory of L-L apparent impedance Z^{BC}_{app} in the impedance plane is displayed in Figure 5-7 (b), where the apparent impedance locates below the initial PZTL but on the revised PZTL. Based on this, one knows that the boundary fault can be detected correctly. In other words, the adaptive tilt setting of PZTL can maintain the high reliability of distance protection effectively.

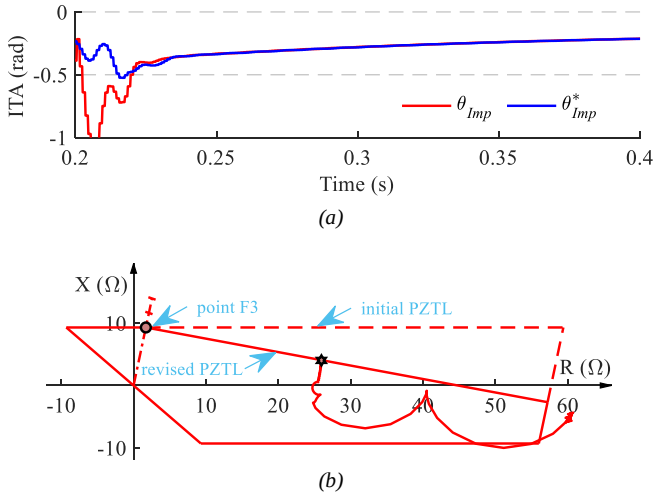

Figure 5-7 Fault BC at point F3, $R_f = 10\Omega$. (a) Dynamic ITAs (b) Impedance trajectory of Z_{app}^{BC}

Except for the above discussed scenarios in Figure 5-5 ~ Figure 5-7, the effectiveness of the adaptive tilt setting of PZTL can also be seen from the rest fault scenarios in columns '$F3 \sim F6$' of Table 4-2. As listed, the calculated negative (or zero) θ_{diff} indicate that the pickup criterion (5.5) is satisfied. Under such condition, the PZTL needs to tilt at $\hat{\theta}_{Imp}$, representing the effective compensation for real tilt of apparent impedance at θ^*_{Imp} (due to the fact of $\hat{\theta}_{Imp} = \theta_{Imp} \leq \theta^*_{Imp} < 0$).

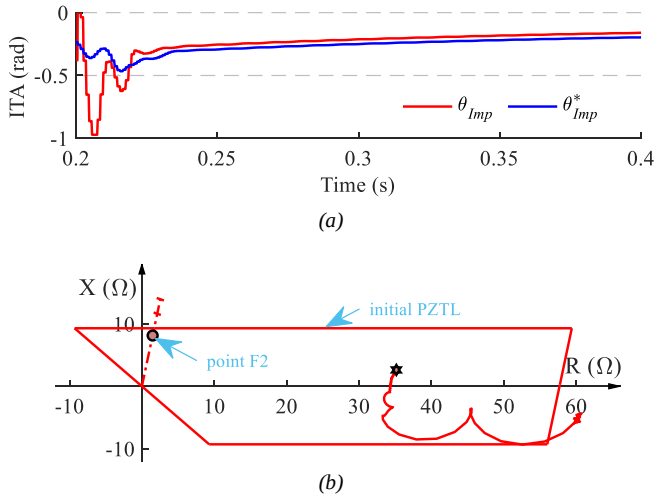

Figure 5-8 Fault BCG at point F2, $R_f = 20\Omega$. (a) Dynamic ITAs (b) Impedance trajectory of Z_{app}^{BCG}

According to the clarification for risk area under the CWIT condition in section 5.1.4, one knows that the internal fault will not cause the malfunction of distance relay adopting initial PZTL setting. This is evident for the fault scenarios in columns '$F1 \sim F2$' of Table 4-2, where the calculated positive θ_{diff} indicate that the pickup criterion (5.5) under the CWIT condition is not satisfied. Taking the scenario of L-L-G fault BCG located at $F2$ ($R_f = 20\ \Omega$) as an example, the dynamic performance of the adaptive tilt setting of PZTL is verified. As displayed in Figure 5-8 (a), θ_{Imp} is larger than θ_{Imp}^* after the initial fault transient, dissatisfying the pickup criterion (5.5) under the CWIT condition. In Figure 5-8 (b), the impedance trajectory converges into the protective zone under the initial PZTL setting.

In addition, the performance of the adaptive tilt setting of PZTL is further investigated when FCGs deploy the BCC strategy, referring to the operation condition of FCG mentioned in section 4.3.4.

As listed in Table 4-4, Con-21 measures shorter fault distances in almost all fault scenarios. Taking the scenario of L-L-G fault BCG located at $F5$ of Table 4-4 as an example, the dynamic performance of the adaptive tilt setting of PZTL is verified. As displayed in Figure 5-9 (a), for the scenario of $R_f = 5\ \Omega$, θ_{Imp}^* converges to be larger than zero rapidly, dissatisfying the pickup criterion (5.5) under the CWIT condition. Correspondingly, this external fault can be correctly clarified under the initial PZTL setting (see the impedance trajectory in Figure 5-9 (b)). In contrast, for the larger resistive scenario of $R_f = 100\ \Omega$, θ_{Imp} and θ_{Imp}^* rapidly converge and satisfy the pickup criterion (5.5) under the CWIT condition (see Figure 5-9 (a)). In Figure 5-9 (b), one can see that this external fault will be correctly identified by adopting the revised PZTL setting.

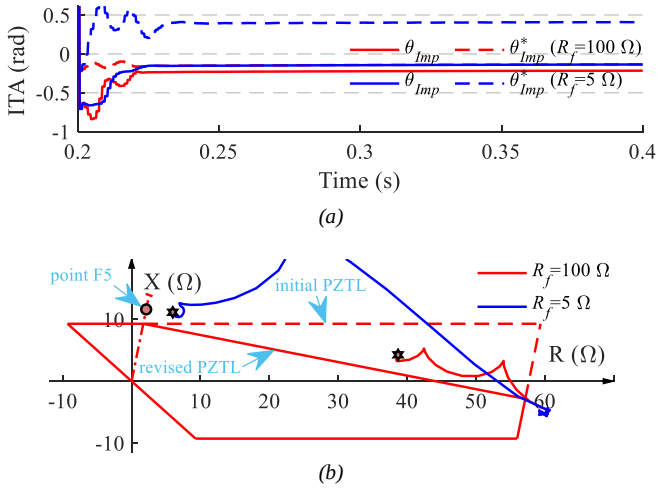

Figure 5-9 Fault BCG at point F5, in the case of different fault resistances. (a) Dynamic ITAs (b) Impedance trajectories of Z_{app}^{BCG}

From the above simulation study, one knows that the adaptive tilt setting of PZTL can effectively compensate for the relay over-reach in the condition of CWIT.

5.2.2. COMPENSATION OF RELAY UNDER-REACH

In this subsection, the performance of the adaptive tilt setting scheme of PZTL in the condition of counter-CWIT is investigated. Detailed regulation strategies of current limiter in the FCG controller to simulate the condition of counter-CWIT are the same as those mentioned in section 4.3.2.

In contrast to the above CWIT condition in section 5.2.1, distance relay is probably at the under-reaching risk during internal faults in the condition of counter-CWIT, especially for those faults approaching the protective boundary (see the corresponding analysis of risk area in section 5.1.4). This has been discussed in Table 4-3 via a series of fault scenarios. In what follows, several fault scenarios in columns '$F1$~$F3$' of Table 4-3 are re-considered to elaborate the effectiveness of the adaptive tilt setting of PZTL in detail.

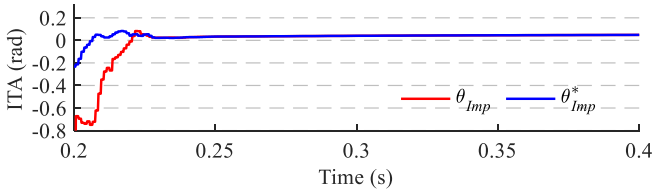

(a)

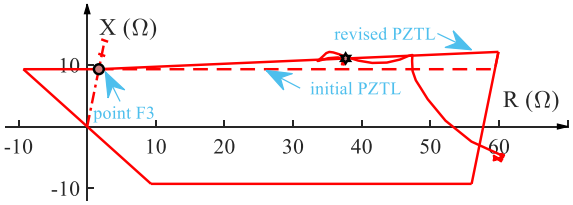

(b)

Figure 5-10 Fault AG at point F3, $R_f = 20\Omega$. (a) Dynamic ITAs (b) Impedance trajectory of Z_{app}^{AG}

Figure 5-10 displays the simulation results for fault AG located at $F3$, $R_f = 20\ \Omega$. In Figure 5-10 (a), θ_{Imp} and θ^*_{Imp} converge to be positive and overlap with each other after the transient fluctuation, which meets the pickup criterion (5.6) under the counter-CWIT condition. Meanwhile, one can see that the boundary fault is initially 'seen' as an external fault under the initial PZTL condition (see the apparent

impedance location in Figure 5-10 (b)). However, it will be detected correctly with the adoption of the revised PZTL setting.

In addition, the simulation results for two fault BC occurring at $F1$ and $F2$ ($R_f = 10\ \Omega$) are compared in Figure 5-11. As depicted in Figure 5-11 (a), for fault BC at point $F1$, θ^*_{Imp} maintains to be negative in fault steady state, which does not satisfy the pickup criterion (5.6) under the counter-CWIT condition. Thus, the fault can be correctly detected under the initial PZTL condition (see the apparent impedance for fault BC at point $F1$ in Figure 5-11 (b)). However, for fault BC at point $F2$, θ_{Imp} and θ^*_{Imp} converge to the relatively steady states (being positive) after the transient fluctuation, which satisfies the pickup criterion (5.6). From the corresponding impedance trajectory plotted in Figure 5-11 (b), one can see that the adaptive tilt setting of PZTL can effectively compensate for the under-reaching problem. Under the revised PZTL setting, the internal fault will be correctly detected.

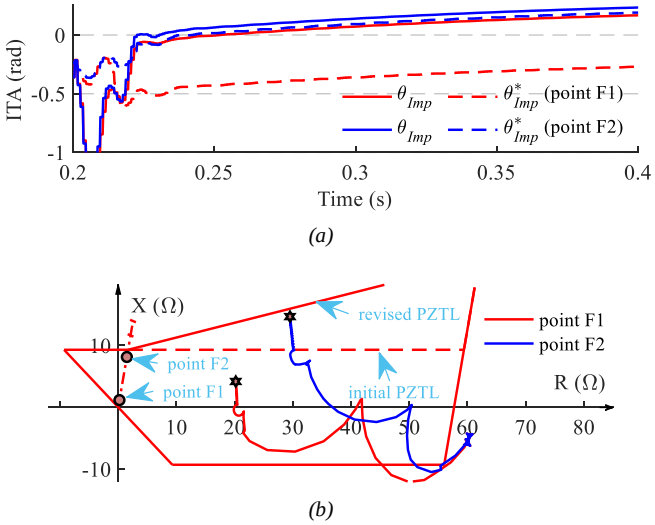

Figure 5-11 Different internal fault BC, $R_f = 10\Omega$. (a) Dynamic ITAs (b) Impedance trajectory of Z^{BC}_{app}

For those external fault scenarios in columns '$F4 \sim F6$' of Table 4-3, the calculated negative θ_{diff} indicate the pickup criterion (5.6) being not satisfied. Thus, the counter-CWIT does not affect the distance relay adopting the initial ZPTL setting. This will not be further discussed in detail.

5.2.3. INFLUENCE OF THE INTERMITTENT CHARACTERISTICS OF FCG-BASED PLANT

As we know that, the FCG-based plant may perform intermittent characteristics of generation. Under such background, one may infer that the transmission system emanating from the FCG-based plant probably undergoes varying loading condition. Thus, it is meaningful to take such influence into consideration for protection design. In this section, the factor of unstable wind speed for wind power is taken, for example.

In contrast to the variation of wind speed, the response of turbine is relatively slow [117]. In the view of protection system, mainly a short period after faults is concerned, i.e. dozens to hundreds of milliseconds. For the variation of wind speed in such a small interval, the turbine can be deemed to response in constant or at most in ramp [117]. To better illustrate such impacts, the factor of wind speed is separately analyzed from three aspects.

A. Influence of different capacities of the local FCG-based plant

First analyze the influence of different capacities of local FCG-based plant on the adaptive tilt setting scheme of PZTL. This can be seen as the different pre-fault loading conditions due to the different wind speed.

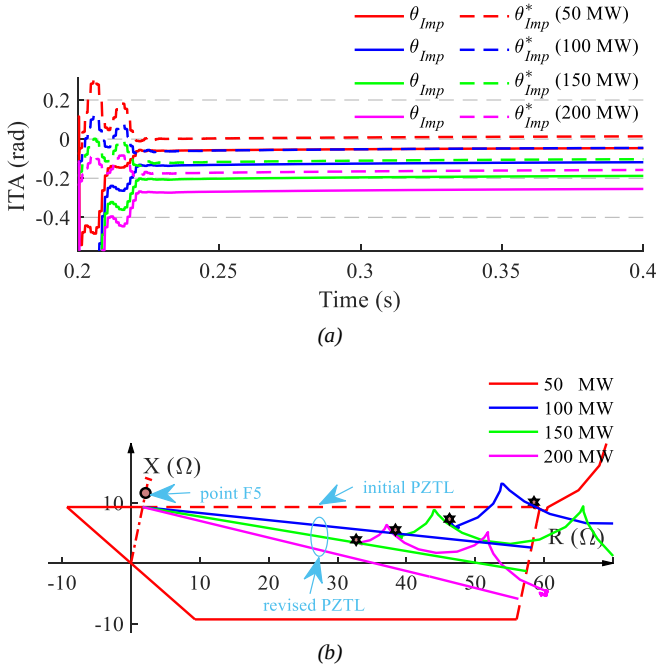

Figure 5-12 Fault AG at point F5, $R_f = 20\Omega$. (a) Dynamic ITAs (b) Impedance trajectories of Z_{app}^{AG}

Take the fault condition of CWIT, for example. Figure 5-12 illustrates the simulation results of a L-G fault AG located at $F5$, $R_f = 20\ \Omega$. Comparing the ITA results in Figure 5-12 (a), one can see that θ_{Imp} and θ_{Imp}^* dissatisfy the pickup criterion (5.5) only when the capacity of FCG-based plant is 50 MW. In this case, one can see that the external fault can be correctly detected under the initial PZTL setting (see the corresponding impedance trajectory presented in Figure 5-12 (b)). For the other three capacity scenarios, the pickup criterion (5.5) is always fulfilled and the adaptive tilt setting of PZTL needs to be in use to compensate for the over-reaching issues. By adopting the revised PZTL, the apparent impedance locate out of the protective zone finally (see the impedance trajectories of these three scenarios displayed in Figure 5-12 (b)).

The above studies prove that the adaptive tilt setting scheme of PZTL is unaffected by the variation of pre-fault FCG-based plant capacity [117].

B. Influence of wind speed variation during faults

In this section, the focus is the influence of varying wind speed during grid faults. Under the severe condition, this will lead to the variation of active power generation in ramp. To observe the effect of varying active current output, an internal fault BCG located at $F2$, $R_f = 10\ \Omega$, is simulated. Fault occurs at 0.2s, and the active current (positive sequence component) of FCG initially maintains at 1 p.u., which begins to ramp down at 0.3s and stabilizes to 0.4 p.u. at 0.306s. This can be seen from the variation of PCC voltage as well as reference currents, as depicted in Figure 5-13 (a).

First consider the fault condition before active current ramping down. As shown in Figure 5-13 (b), θ_{Imp} and θ_{Imp}^* converge to relatively steady states (being negative) after a short transient fluctuation, and θ_{Imp} maintains larger than θ_{Imp}^*. This fulfills neither the pickup criterion (5.5) nor the criterion (5.6), meaning the internal fault can be detected correctly under the initial PZTL setting. This can be seen from Figure 5-13 (c), where the apparent impedance (square mark) stabilizes within the protective zone. After 0.3s, the active current of FCG gradually ramps down to 0.4 p.u. Under such fault condition, one can see that θ_{Imp} and θ_{Imp}^* converge to newly steady states in Figure 5-13 (b). The angular results satisfy the pickup criterion (5.6) of counter-CWIT condition. Correspondingly, in Figure 5-13 (c), one can see that the steady-state apparent impedance (hexagram mark) locates out of the protective zone under the initial PZTL setting. However, it is in the protective zone under the revised PZTL setting.

This study proves that the adaptive tilt setting of PZTL is adaptive to the variation of wind speed during faults.

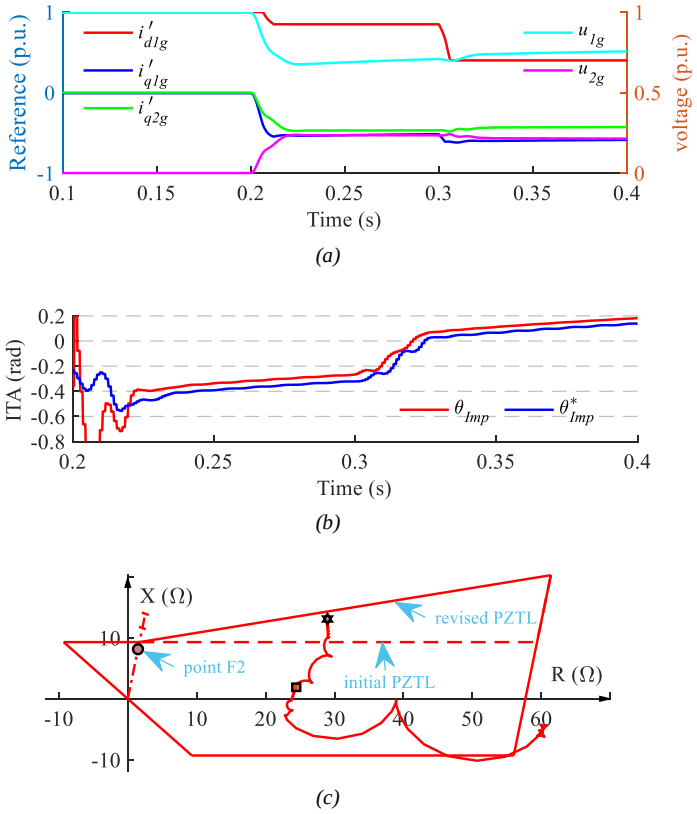

Figure 5-13 Fault BCG at point F2, $R_f = 10\Omega$. (a) Control variables (b) Dynamic ITAs (c) Impedance trajectory of Z_{app}^{BCG}

What is worth mentioning, the above analysis applies to the crowbar effects. After grid faults, the crowbar circuit is expected to dissipate those excessive active power from the wind turbine, which is to limit the speed-up of the wind turbine and the converters' DC over-voltage. For the effect of change in crowbar resistance, one can infer that the GSC mainly undergoes a varying DC power, i.e. the varying active current output.

C. Influence of partial FCGs off-grid during faults

In the third aspect, the influence of varying FCGs being in service during grid faults is analyzed. Take the off-grid of partial FCGs, for example. The inception of L-L fault BC (at point *F*4) is at 0.2 s. Besides, half FCGs are off-grid after 0.3 s, simulating the possible abnormal operation of FCG-based plant due to the low voltage (or overcurrent) during grid faults [117].

Figure 5-14 (a) displays the variation of instantaneous current at FCG-based plant side. Under such condition, the pickup criterion (5.5) is always valid, as depicted in Figure 5-14 (b). Even though the abnormal operation of FCG-based plant brings in a certain fluctuation to θ_{Imp} and θ^*_{Imp} and leads them to tend to newly relative-steady states. The impedance trajectory, covering the abnormal operation of FCG-based plant, is further plotted in Figure 5-14 (c). In the subplot (c), steady-state apparent impedance measured by the relay at phases of before and after the abnormal operation are marked in square and hexagram, respectively. Correspondingly, the revised PZTL at these two phases are highlighted as 'old' and 'new'. From subplot (c), one can see that the external fault can be detected correctly. In other words, the adaptive tilt setting of PZTL can adapt to such abnormal operation of FCG-based plant.

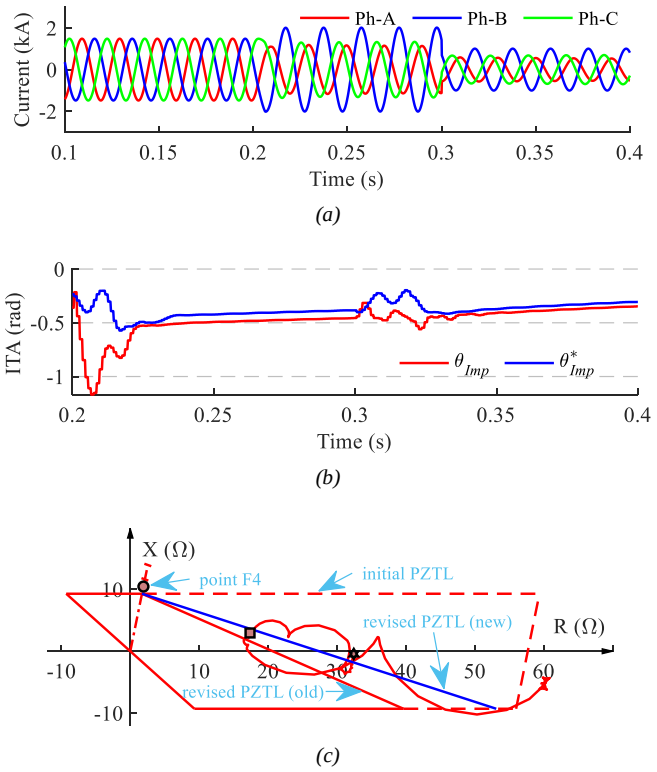

Figure 5-14 Fault BC at point F4, $R_f = 5\Omega$. (a) Current measurement (b) Dynamic ITAs (c) Impedance trajectory of Z^{BC}_{app}

From the above three aspects, one can conclude that the adaptive tilt setting scheme of PZTL is unaffected by the intermittent generation characteristics of the local FCG-based plant [117].

5.2.4. ERROR ANALYSIS

For both the adaptive tilt setting of PZTL in this chapter and the ITA-21 scheme in the previous chapter, the accuracy of estimated ITA θ_{Imp} is always a critical factor. Since a constant parameter m is in use to initialize the current distribution factors in ITA estimation, the error characteristics of θ_{Imp} are comprehensively analyzed in this section.

A. Local line faults

Scenario 1: For the parameter initialization in use, $D_{0,2}|_{m=m_{[0]}}$ ($m_{[0]} = 0.8$ indicates the zone 1 length), θ_{Imp} is accurate for boundary faults only. Because $m_{[0]}$ equals the real fault distance at the moment. In contrast to the boundary faults, θ_{Imp} will include a certain error when faults occur at other positions due to the difference of $m_{[0]}$ to real fault distance. Take, for example, the L-G fault AG. Define the angles of $D_0|_{m=m_{[0]}}$ and $D_0|_{m=real\_fault\_distance}$ as θ_{D_0} and $\theta^*_{D_0}$, respectively. At the fault steady-state, (4.13) can be revised as (5.8) [117],

$$\theta_{AG} = -angle\left\{\left[\frac{\dot{I}_{1S}+\dot{I}_{2S}}{\dot{I}_{0S}}+(1+K_0)\right]\cdot D_0\Big|_{m=real\_fault\_distance}\right\}+\delta_{D_0} \tag{5.8}$$

where δ_{D_0} is the angular error, meeting $\delta_{D_0} = (\theta^*_{D_0} - \theta_{D_0})$.

Before analyzing the error characteristics of δ_{D_0} against the parameter m, another key factor (the equivalent remote source impedance) that can also affect the angle of D_0 must be considered (see the numerator of (4.10), meaning Z_r here). This is because the X/R ratio of equivalent remote source impedance, i.e. the impedance angle, is possibly different in different network conditions. Take the in-feeds from extra high voltage systems, for example. The X/R ratio can be large, i.e. the X-component is dominant. Otherwise, if the high (or medium) voltage lines are dominant in the remote source impedance, the R-component is no longer ignorable. Table 5-1 lists the typical X/R parameters of equivalent source in transmission system.

TABLE 5-1 TYPICAL PARAMETERS OF SCOURCE IMPEDANCE AT DIFFERENT VOLTAGE LEVELS [104]

Voltage Level	X/R	Impedance angle
380 kV	8-10	82.8º-84.3º
220 kV	5-8	78.7º-82.8º
110 kV	3-5	71.6º-78.7º

Considering the typical impedance angle of 110 kV over-head-line being around 79º [104] (the impedance angle of line listed in Table B.2 is at 79.6º), the varying angular conditions of remote source impedance, i.e. 71.6º to 78.7º, but the same in magnitude,

are used to evaluate the influence (Figure 5-15). Note that, the source impedance angle at 75.96º is the one used in previous tests.

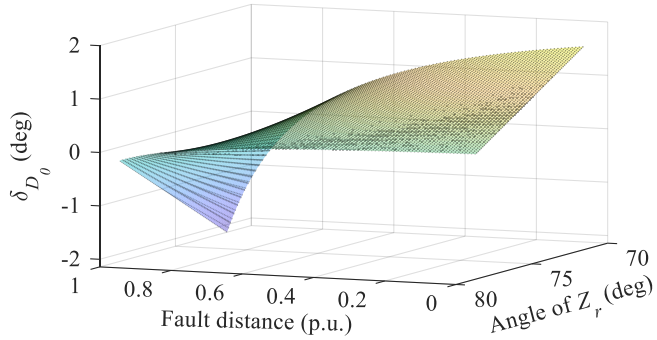

Figure 5-15 Variation of δ_{D_0} for different fault positions, in the case of varying remote source impedance angles

From Figure 5-15, one can see that δ_{D_0} follows monotonic decreasing properties against the increased m from 0 to 1. And it is zero in the case of $m = m_{[0]}$. Besides, the larger the angular deviation of source impedance to line impedance is, the sharper the gradient of δ_{D_0} is.

Subsequently, one can conclude the error characteristics of θ_{Imp} against parameter m, in the above case of a smaller remote source impedance angle than that of line.

1) If $m < m_{[0]}$, θ_{Imp} shows a slightly positive angular error, which can be seen as under-compensating for the impedance tilt.
2) If $m = m_{[0]}$, θ_{Imp} shows the highest estimating accuracy.
3) If $m > m_{[0]}$, θ_{Imp} shows a slightly negative angular error, which can be oppositely seen as over-compensating for the impedance tilt.

The above-discussed over-compensation (or under-compensation) during the internal (or external) faults has a certain influence on the adaptive tilt setting of PZTL. This can be seen from the following ITA results of fault AG under the source impedance angular condition at 75.96º in Figure 5-16.

In the figure, except for the θ_{Imp} based on $D_0|_{m=[m_0]}$ and $D_0|_{m=real\ fault\ distance}$, θ^*_{Imp} against the varying fault distance is also displayed. Clearly, the relative angles of θ_{Imp} ($D_0|_{m=[m_0]}$) to θ^*_{Imp} for all internal and external faults are slightly enlarged. This actually improves the reliability of the adaptive tilt setting of PZTL, which is unaffected by the fault resistance.

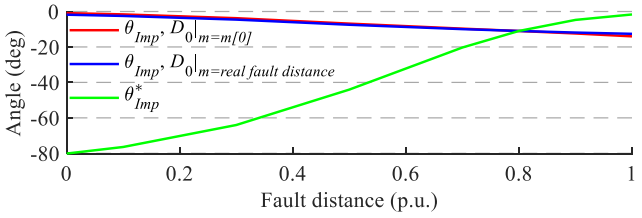

(a)

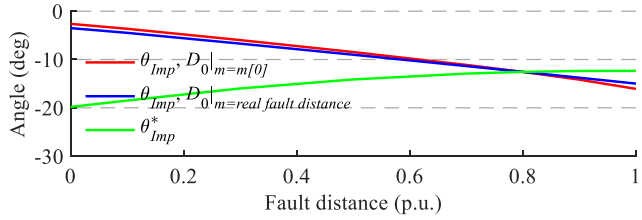

(b)

Figure 5-16 Variation of ITAs for fault AG at different fault positions, in the case of remote source impedance angle at 75.96º. (a) $R_f = 5\Omega$ *(b)* $R_f = 100\Omega$

Scenario 2: Table 5-2 lists a set of sequence impedance parameters of 220 kV transmission line. The corresponding line impedance angles are also around 79º. In contrast to the situation of 110 kV line condition, one can infer that the error characteristics of δ_{D_0} is different, since the line impedance angle is within the typical angular range of source impedance at 220 kV voltage level (Table 5-1).

TABLE 5-2 IMPEDANCE PARAMETERS OF 220 KV TRANSMISSION LINE IN PER KM [124]

Category	'1,2' sequence	'0' sequence
Sequence impedance	0.2412+1.2696j	0.7237+3.8088j

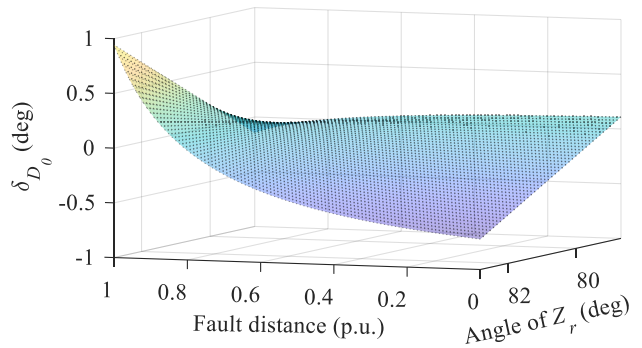

Figure 5-17 Variation of δ_{D_0} *for different fault positions, in the case of varying remote source impedance angle (220 kV system)*

By reconfiguring the test system in Figure 4-8 as a 220 kV system, the error characteristics of δ_{D_0} are analyze in the same way, as displayed in Figure 5-17. In the figure, one can see that δ_{D_0} also follows monotonic properties against the increased *m* from 0 to 1. It monotonically increases, in the case of a larger remote source impedance angle than line one. However, it monotonically decreases, in the case of a smaller remote source impedance angle than line one.

What interesting is that δ_{D_0} maintains zero if the remote source impedance angle equals that of the line (79.2º). This is because the remote source impedance can be replaced by the line impedance multiplying a real coefficient under such condition. Following this, the angle of D_0 is no longer affected by the parameter *m* -related item in numerator of (4.10).

Here, one can conclude the error characteristics of θ_{Imp} against parameter m from three source impedance conditions [117]:

Condition 1: in the case of a smaller remote source impedance angle than that of line

1) See the conclusion in *Scenario 1*.

Condition 2: in the case of remote source impedance angle equaling that of line

1) θ_{Imp} shows the high estimation accuracy for all faults along the protected line.

Condition 3: in the case of a larger remote source impedance angle than that of line

1) If $m < m_{[0]}$, θ_{Imp} shows a slightly negative angular error, which can be seen as over-compensating for the impedance tilt.
2) If $m = m_{[0]}$, θ_{Imp} shows the highest estimation accuracy.
3) If $m > m_{[0]}$, θ_{Imp} shows a slightly positive angular error, which can be oppositely seen as under-compensating for the impedance tilt.

The influence of the error characteristics of θ_{Imp} under '*condition 1*' on the adaptive tilt setting of PZTL has been analyzed in *Scenario 1*, which will not be repeated here.

Referring to '*condition 2*', the corresponding conclusion is further revealed by the ITA results for fault AG under the source impedance angular condition at 79.24º, as depicted in Figure 5-18. In this test, take the fault AG as an example, $R_f = 20\ \Omega$. Different to the error tendency under '*condition 1*', θ_{Imp} based on $D_0|_{m=[m_0]}$ and $D_0|_{m=real\ fault\ distance}$ overlaps with each other in the figure, meeting the conclusion of '*condition 2*'.

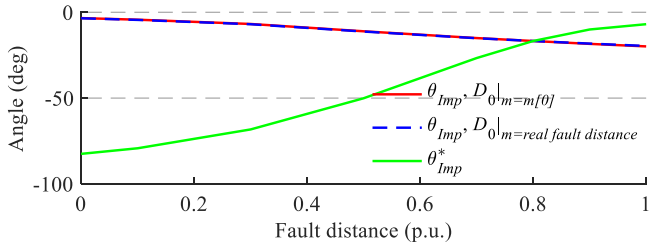

Figure 5-18 Variation of ITAs for fault AG at different fault positions (R_f = 20Ω), in the case of remote source impedance angle at 79.24º.

Furthermore, test how error characteristics of θ_{Imp}, regarding '*condition 3*', would affect the adaptive tilt setting of PZTL.

One thing is that current distribution factor D_2 follows similar error characteristics to D_0 under the same angular condition of source impedance [117]. Define the angles of $D_2|_{m=m_{[0]}}$ and $D_2|_{m=real\_fault\_distance}$ as θ_{D_2} and $\theta^*_{D_2}$, respectively. For L-L fault, e.g. fault BC, (4.18) is revised as,

$$\theta_{BC} = -Angle\left\{\left(1-\frac{\dot{I}_{S1}}{\dot{I}_{S2}}\right)\cdot D_2\big|_{m=real\_fault\_distance}\right\}+\delta_{D_2} \tag{5.9}$$

where $\delta_{D_2} = (\theta^*_{D_2} - \theta_{D_2})$ represents the angular error.

Figure 5-19 reveals the ITA results for fault BC under the source impedance angular condition at 82.8º. As shown in the figure, the relative angles of θ_{Imp} ($D_2|_{m=[m_0]}$) to θ^*_{Imp} for all faults along the protected line are slightly narrowed down. Besides, the error of estimated θ_{Imp} is often small (In practical transmission system, the angular difference of source impedance to the line one is inconspicuous). Combining the fact that the adaptive tilt setting of PZTL is activated within the malfunction risk area located at a certain range around zone 1 set point only, one can infer that the adaptive tilt setting of PZTL has enough operating safety margin for faults along the protected line.

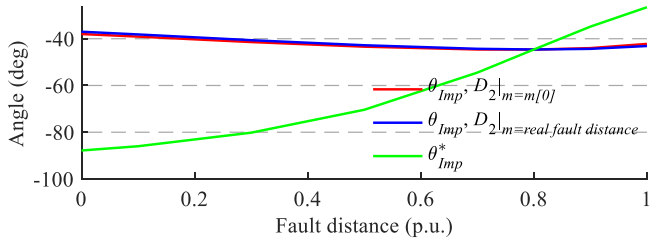

Figure 5-19 Variation of ITAs for fault BC at different fault positions (R_f =10Ω), in the case of remote source impedance angle at 82.8º.

B. Downstream line faults

The above error analysis focuses on the faults located at the protected line. However, the error characteristics of θ_{Imp} are resulted from different causes during downstream line faults, since the intermediate in-feed is the critical factor here. Considering the downstream line fault in the test system of Figure 4-8, the single-line fault network is marked as Figure 5-20, where Z_{L1} and $Z_{L2-1.f}$ are the impedance of local line and downstream line (up to the fault point). $\dot{I}_{im}$ is the current component of intermediate in-feed. Other variables have the same definition with those in Figure 2-14.

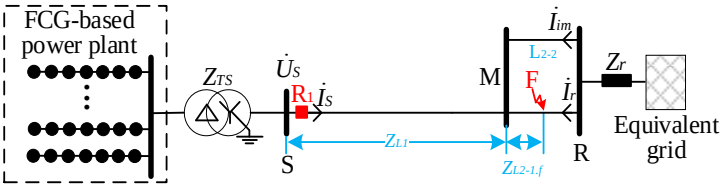

Figure 5-20 Single-line fault network of Figure 4-8, in the case of downstream line fault

From Figure 5-20, one can re-write the apparent impedance of (2.20) as [117],

$$\begin{aligned} Z_{app} &= \frac{\dot{U}_s}{\dot{I}_s} = Z_{L1} + Z_{L2-1.f} \cdot \frac{\dot{I}_{im} + \dot{I}_s}{\dot{I}_s} + R_f \cdot \frac{\dot{I}_{im} + \dot{I}_s + \dot{I}_r}{\dot{I}_s} \\ &= Z_{L1} + Z_{L2-1.f} + Z_{L2-1.f} \cdot \frac{\dot{I}_{im}}{\dot{I}_s} + R_f \cdot \frac{\dot{I}_{im} + \dot{I}_s + \dot{I}_r}{\dot{I}_s} \\ &= Z_{L1} + Z_{L2-1.f} + \underbrace{\Delta Z_{im} + \Delta Z}_{virtual\_increment} \end{aligned} \tag{5.10}$$

Different to (2.20), a new impedance component due to the intermediate in-feed is included in the virtual increment. Under such condition, since the PZTL tilt at $angle(\Delta Z)$ is still adopted rather than the real value $angle(\Delta Z_{im} + \Delta Z)$, there will exist a certain deviation [117]. This is analyzed based on the magnitude of R_f in detail.

Scenario 1 [117]: For a fault with tiny R_f, since $|\Delta Z|$ is inconspicuous in magnitude, one knows that $angle(\Delta Z_{im} + \Delta Z) \approx angle(\Delta Z_{im})$. Bearing the fact of $\dot{I}_{im}$ sharing the same source with $\dot{I}_r$, one can further deduce the following inequality,

$$\begin{aligned} angle\left(\Delta Z_{im} + \Delta Z\right) \approx angle\left(\Delta Z_{im}\right) &= angle\left(\frac{\dot{I}_{im}}{\dot{I}_s}\right) + angle\left(Z_L\right) \\ \gg angle\left(\frac{\dot{I}_{im}}{\dot{I}_s}\right) &\approx angle\left(\frac{\dot{I}_{im} + \dot{I}_r}{\dot{I}_s}\right) \end{aligned} \tag{5.11}$$

To facilitate the analysis, assume the grid strength being much stronger than FCG-based plant. Under such condition, (5.11) can be further deduced as,

$$\begin{aligned} angle\left(\Delta Z_{im}+\Delta Z\right) &\approx angle\left(\Delta Z_{im}\right)=angle\left(\frac{\dot{I}_{im}}{\dot{I}_s}\right)+angle\left(Z_L\right)\gg angle\left(\frac{\dot{I}_{im}}{\dot{I}_s}\right) \\ &\approx angle\left(\frac{\dot{I}_{im}+\dot{I}_r}{\dot{I}_s}\right)\approx angle\left(\frac{\dot{I}_{im}+\dot{I}_r+\dot{I}_s}{\dot{I}_s}\right)=angle\left(\Delta Z\right) \end{aligned} \quad (5.12)$$

Equation (5.12) indicates that the adopted PZTL tilt at $angle(\Delta Z)$ will be much smaller than the real value $angle(\Delta Z_{im}+\Delta Z)$.

Scenario 2 [117]: For extremely high resistive fault, since $|\Delta Z| \gg |\Delta Z_{im}|$ is true, one knows that $angle(\Delta Z_{im}+\Delta Z) \approx angle(\Delta Z)$. Under such condition, one can infer that the effects of intermediate in-feed on the adopted PZTL tilt at $angle(\Delta Z)$ can be ignored.

To better observe the error characteristics of θ_{Imp} resulted from intermediate in-feed, two downstream line faults, i.e. fault AG at point $F6$, with different fault resistance are compared. Impedance trajectories for both the tests are plotted in Figure 5-21.

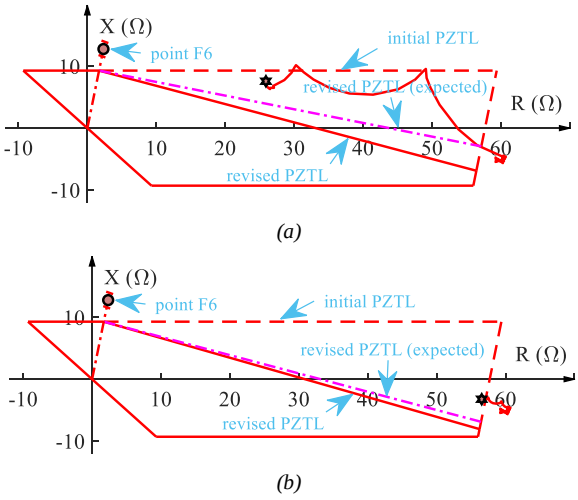

Figure 5-21 Impedance trajectories of Z_{app}^{AG} for fault AG at point F6. (a) R_f =10Ω (b) R_f = 200Ω

In the figure, except for the revised PZTL based on θ_{Imp}, the one based on the real value $angle(\Delta Z_{im}+\Delta Z)$ is also given (highlighted using 'expected'). Take the fault scenario of $R_f = 10\ \Omega$ in Figure 5-21 (a), for example. By comparing the PZTLs, one knows that θ_{Imp} is smaller than the real tilting angle $angle(\Delta Z_{im}+\Delta Z)$. This applies to another resistive fault too. In terms of distance relay, such error characteristics

during downstream line faults in turn enhance the relay reliability. For both fault scenarios, the revised PZTL adopting θ_{Imp} can compensate for the over-reaching problem, and the external faults can be identified correctly.

In the view of fault resistance, one can also see that the deviation of θ_{Imp} to $angle(\Delta Z_{im} + \Delta Z)$ reduced clearly along with the increase of R_f from $10\ \Omega$ to $200\ \Omega$. In other words, the impact of intermediate in-feed decreases. The phenomena shown in the figure accord with the above error characteristics.

Based on the qualitative error analysis and case studies in this section, one knows that the proposed tilt setting method of PZTL can effectively compensate for the influence caused by the apparent impedance tilt for all the forward faults [117].

The above error analysis also applies to the ITA-21 in chapter 4.

5.3. DISCUSSION

Focusing on the same apparent impedance tilt caused relaying problem for distance protection, in this chapter, the adaptive tilt setting scheme of PZTL is developed to protect the transmission line connecting FCG-based plant. Similar to chapter 4, the new protection setting method is also validated based on the simulation study in both the fault conditions of CWIT and counter-CWIT. Simulation results prove that the adaptive tilt setting of PZTL is capable of handling the faults in the outgoing system of FCG-based plant. The detailed **properties** of the adaptive tilt setting of PZTL are outlined as:

1) The adaptive tilt setting of PZTL compensates for the influence caused by apparent impedance tilt, i.e. tilting the PZTL (polygonal relay characteristic) an angle θ_{Imp}. This is effective to either the over-reaching problem under the condition of CWIT or the under-reaching one under the counter-CWIT condition.
2) Benefiting from the risk area division, the adaptive tilt setting of PZTL is only activated under certain conditions, improving its reliability and efficiency.
3) Simulation study proves that the adaptive tilt setting of PZTL is robust to the possible intermittent characteristics of the FCG-based plant.
4) It is indicated that the error characteristics of adaptive tilt setting of PZTL have different dominant causes during local line and downstream line faults. For local line faults, it is resulted from the difference of X/R ratio between the line and the equivalent external source [117]. Considering the homogeneity (or homogeneity-like) property of transmission grid in practice, the difference of these two X/R ratio is slight, guaranteeing the reliability of the adaptive tilt setting of PZTL. For downstream line faults, the intermediate in-feed is the critical factor of the error characteristics in the adaptive tilt setting of PZTL [117]. Qualitative error analysis proves that such error in turn brings in the positive effects on the reliability of the adaptive tilt setting of PZTL.

Limitation statement:

Similar to ITA-21, the adaptive tilt setting of PZTL is not suitable for the symmetrical grid faults, neither can it be applied to the L-G (or L-L-G) faults in a system without grounding connections [117].

CHAPTER 6. PROTECTION COMPATI-BLE FAULT REGULATION OF FCG DURING ASYMMETRICAL GRID FAULTS

For the same malfunction issues of distance protection deployed in the line emanating from FCG-based plant after grid faults, two kinds of countermeasures have been discussed in chapters 4 and 5. Both of them solve the relay malfunction issue from the protection side. In view of the FCG control, the relay malfunction relates to the specified fault control rules in different grid codes. Considering the fully controllable characteristics of PEC, the FCG (PEC) control-based solution compatible with the protection demand is also possible.

6.1. BASIC PRINCIPLE AND ITS FEASIBILITY

Considering the fault network of Figure 2-14, the expression of the apparent impedance in (2.20) is rewritten as,

$$Z_{apparent} = \frac{\dot{U}_s}{\dot{I}_s} = mZ_1 + R_f\left(1 + \frac{\dot{I}_r}{\dot{I}_s}\right) \tag{6.1}$$

The malfunction problem of distance relay discussed in chapters 4 and 5 can be attributed to the unfocused active power delivery from FCG-based plant during grid faults. In other words, the FCG side current $\dot{I}_s$ can lag (or lead) the remote infeed $\dot{I}_r$, which causes the relay to over-reach (or under-reach).

6.1.1. INFLUENCE OF CURRENT CONTROL ANGLE

First, the influences of different current regulating requirements on the relay's performance are investigated in the test system connecting FCG-based plant of Figure 2-16. The BCC method is deployed in the FCG control system. Under such a control method, FCG outputs positive sequence current only. The fault current $\dot{I}_{1g}$ of PEC in (2.5) can be further re-written as,

$$\begin{aligned}\dot{I}_{1g} &= \left(I''_{d1g} + j \cdot I''_{q1g}\right) exp\left[j \cdot angle\left(\dot{V}_{1g}\right)\right] \\ &= \sqrt{{I''_{d1g}}^2 + {I''_{q1g}}^2} \cdot exp\left[j \cdot \left(angle\left(\dot{V}_{1g}\right) + atan\left(\frac{I''_{q1g}}{I''_{d1g}}\right)\right)\right]\end{aligned} \tag{6.2}$$

In (6.2), $atan\left(I''_{q1g}/I''_{d1g}\right)$ is the current reference angle specified by Grid Codes, which meets $atan\left(I''_{q1g}/I''_{d1g}\right) \in [0°, -90°]$ in theory.

Take a 10 Ω resistive L-G fault AG located at $F2$, for example. A varying control trajectory shown in Figure 6-1 is tested, where the current references I''_{dq1g} accord with the path from A to C. Under such a condition, the current reference angle decreases from 0° to −90°. It has considered both the current limit I_g^{lim} of PEC and the maximum reactive current limit (assuming the $|I''_{q1g}|$ of horizontal line BC) to a specific PCC voltage sag.

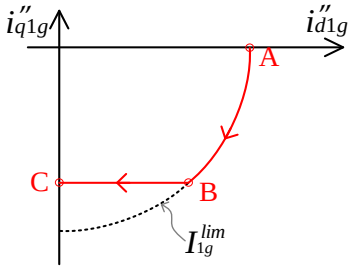

Figure 6-1 Vector diagram of the current references in rotating reference frame.

Figure 6-2 depicts the variation of apparent impedance corresponding to the control trajectory displayed in Figure 6-1. In the figure, the red line represents the line impedance, while zone 1 reach of the distance relay (solid blue line) covers 80% of the line. The internal fault AG locates at 70% line length from the relay. It can be seen that the imaginary part of the apparent impedance (solid black curve marked with '◦') seen by the relay increases when the current reference angle decreases.

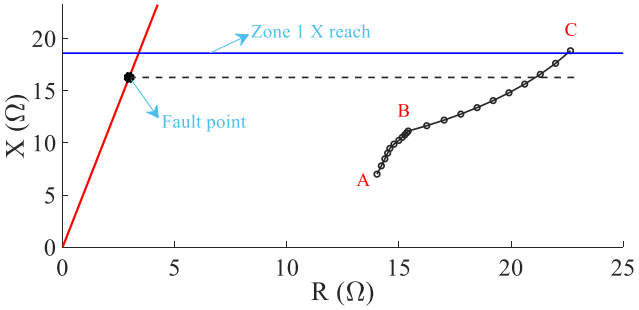

Figure 6-2 Relationship between the relay measured impedance and the varying current control angle.

On the other hand, the varying trajectory of the apparent impedance intersects with the real fault position (dashed black line) at a certain point between operation points B and C, where the distance relay can see an accurate fault position in the X-direction.

Bearing this in mind, one knows that the relay over- or under-reaching problem will not happen if the current $\dot{I}_s$ at the FCG-based plant side can be adjusted to stay in phase with $\dot{I}_r$, referring to (6.1). This is possible from the perspective of FCG since the phase angle of the positive sequence current in (6.2), $atan\left(I''_{q1g}/I''_{d1g}\right)$, is adjustable. Therefore, the control function can be determined as,

$$angle\left(1+\frac{\dot{I}_r}{\dot{I}_s}\right)=0 \tag{6.3}$$

6.2. MODIFIED MODELING ANALYSIS OF FCG CONSIDERING THE TARGET OF PROTECTION COMPATIBLE CONTROL

In this chapter, based on the configuration of the PEC interface shown in Figure 2-2, the short-circuit model in section 2.1.2 is first revised considering the target of protection compatible control.

During grid faults, the top priority is still the reactive current outputs for purpose of the voltage recovery. Thus, the initial reactive current references I'_{q1g} and I'_{q2g}, as well as the revision formula about the current limit in $q-axis$ maintain the same as (2.7), (2.8), and, (2.5). Besides, suppose for a moment that the expected positive sequence current control angle of PEC is θ_{ref} [100]. The initial active current reference I'_{d1g} in $d-axis$ is then expressed as [100],

$$I'_{d1g}=I''_{q1g}\times cot\left(\theta_{ref}\right) \tag{6.4}$$

Referring to the total PEC current limit I_g^{lim}, the reactive current references I''_{qg} in $q-axis$ and the active current references I'_{d1g} is further revised as [100],

$$\begin{cases} I'''_{q1g}=min\left(I''_{q1g},I''_{q1g}/M_1\right) \\ I'''_{q2g}=min\left(I''_{q2g},I''_{q2g}/M_1\right), M_1=\dfrac{\sqrt{\left(I'_{d1g}\right)^2+\left(\left|I''_{q1g}\right|+\left|I''_{q2g}\right|\right)^2}}{I_{qg}^{lim}} \\ I'''_{d1g}=min\left(I'_{d1g},I'_{d1g}/M_1\right) \end{cases} \tag{6.5}$$

Using (2.7), (2.8), (6.4) and (6.5), the current output of FCG in (2.2) and (2.3) can be simplified as the follows [100],

$$\dot{I}_{1g}=\dot{I}'_{source}-Y'_{1FCG}\cdot\dot{V}_{1g} \tag{6.6}$$

$$\dot{I}_{2g}=Y'_{2FCG}\cdot\dot{V}_{2g} \tag{6.7}$$

where $\dot{I}'_{source}$, Y'_{1FCG} and Y'_{2FCG} have the same definitions with those in section 2.1.2 of chapter 2. And, they satisfy,

$$\begin{cases} \dot{I}'_{source} = -\dfrac{K_{V1}\cdot\left(cot\left(\theta_{ref}\right)+1\cdot j\right)}{M'\cdot M'_1}\cdot exp\left[\, j\cdot angle\left(\dot{V}_{1g}\right)\right] \\ Y'_{1FCG} = \dfrac{K_{V1}\cdot\left(1-j\cdot cot\left(\theta_{ref}\right)\right)}{j\cdot M'\cdot M'_1}, Y'_{2FCG} = j\cdot\dfrac{K_{V2}}{M'\cdot M'_1} \end{cases}, M'_1 = max\left(1, M_1\right) \quad (6.8)$$

So far, one can see that the short-circuit models of FCG, when considering the protection compatible control target, keep the same circuit structures as to Figure 2-3, but with different equivalent parameters.

6.3. PROTECTION COMPATIBLE FAULT REGULATION (PCFR)

From (6.3), one can see that the control function is to achieve the convergent target of ITA in (4.2) approaching zero.

In section 6.2, the modeling analysis of FCG proves that the incorporation of the protection compatible control affects the sequence model parameters rather than the model structure. Bearing this in mind, one can infer that the tilt angles of measured impedance at relay location for different asymmetrical faults have the same expressions as those given in (4.13), (4.18), and (4.21).

In addition, the positive sequence current measured at the relay location can be further written as (6.9), if combining the current control angle θ_{ref} of PCFR.

$$\dot{I}_{1S} = \left|\dot{I}_{1S}\right|\cdot exp\left[\, j\cdot\left(\theta_{ref} + angle\left(\dot{U}_{1S}\right)\right)\right] \quad (6.9)$$

where $|\cdot|$ calculates the magnitude of a phasor quantity.

Substituting (6.9) into (4.13), (4.18), and (4.21), the control function in (6.3) for different asymmetrical grid faults, e.g. L-G fault AG, L-L fault BC and L-L-G fault BCG, can be respectively revised as,

$$angle\left\{\left[\frac{\left|\dot{I}_{1S}\right|\cdot exp\left[\, j\cdot angle\left(\dot{U}_{1S}\right)\right]}{\dot{I}_{0S}} exp\left(\, j\cdot\theta_{ref}\right) + \frac{\dot{I}_{2S}}{\dot{I}_{0S}} + (1+K_0)\right]\cdot D_0\right\} = 0 \quad (6.10)$$

$$angle\left\{\left[1-\frac{\left|\dot{I}_{1S}\right|\cdot exp\left[j\cdot angle\left(\dot{U}_{1S}\right)\right]}{\dot{I}_{2S}}exp\left(j\cdot\theta_{ref}\right)\right]\cdot D_2\right\}=0 \tag{6.11}$$

$$angle\left\{\left[1-\frac{\left|\dot{I}_{1S}\right|\cdot exp\left[j\cdot angle\left(\dot{U}_{1S}\right)\right]}{\dot{I}_{2S}}exp\left(j\cdot\theta_{ref}\right)\right]\cdot D_X^*\right\}=0 \tag{6.12}$$

From (6.10)-(6.12), the expected current control angle θ_{ref} can be solved with the local fault information at the relay end only.

Figure 6-3 illustrates the detailed flowchart of the proposed PCFR method. In detail, the implementation procedure concludes four steps:

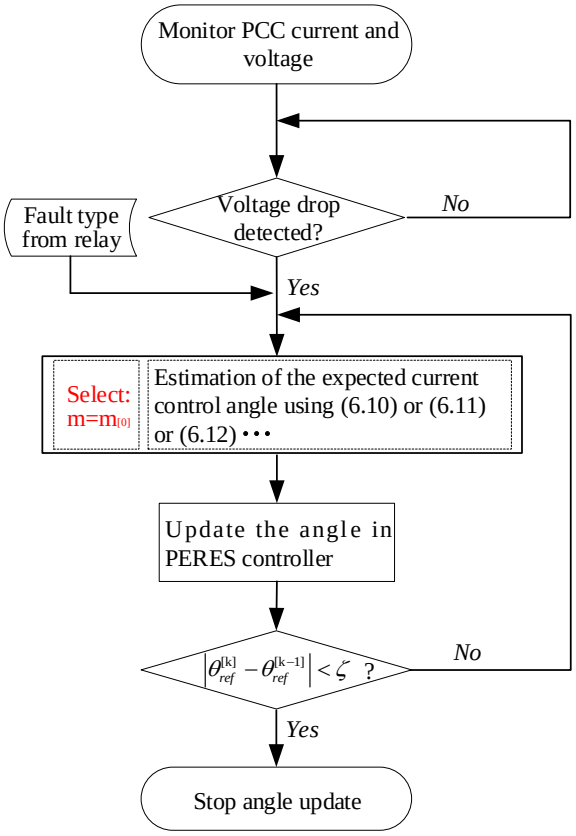

Figure 6-3 Flowchart of the PCFR method

1) Monitor the PCC voltage and current. If the voltage drop is detected, wait for the fault selection outlet from the phase selection unit of the vicinal distance relay.
2) If balanced faults occur, jump to step 4). Otherwise, start the estimation of the expected current control angle.
3) Update the control angle in the current controller, and detect the terminating criterion ($\left|\theta_{ref}^{[k]}-\theta_{ref}^{[k-1]}\right|<\zeta$ lasting for 1 ms). If the terminating criterion is not satisfied, jump to step 2).
4) Otherwise, stop the update of the current control angle.

6.4. CASE STUDY

In this section, different simulation methods are studied to verify the effectiveness of the proposed PCFR method for the auxiliary protection ability in the transmission system connecting FCG-based plant.

6.4.1. FEASIBILITY EVALUATION

TABLE 6-1 COMPARISON OF THE MEASURED FAULT DISTANCES OF RELAY R_1 UNDER DIFFERENT FCG FAULT CONTROLS

Fault point	Real value/p.u.	R_f/Ω	Fault type	Normal method	PCFR method
$F1$	0.1	10	AG	0.0836	0.1342
			BC	-0.2019	0.1446
			BCG	-0.2092	0.1563
		20	AG	0.0810	0.1381
			BC	-0.1926	0.1664
			BCG	-0.0183	0.1611
$F2$	0.7	10	AG	0.5168	0.7082
			BC	0.1794	0.7047
			BCG	0.3617	0.7110
		20	AG	0.4502	0.7040
			BC	0.2501	0.7009
			BCG	0.2887	0.7044
$F3$	0.8	10	AG	0.5252	0.7939
			BC	0.2109	0.8104
			BCG	0.2862	0.8101
		20	AG	0.4573	0.7769
			BC	0.2968	0.8098
			BCG	0.4029	0.8153
$F4$	0.9	10	AG	0.5299	0.8744
			BC	0.2458	0.8770
			BCG	0.4727	0.8804
		20	AG	0.4263	0.8669
			BC	0.4433	0.8661
			BCG	0.3728	0.8558

*Note: Normal method—normal LVRT control method.

Firstly, simulation studies based on the DIgSILENT/PowerFactory model of Figure 2-16 are given. Table 6-1 compares the fault distances measured by the relay R_1, where the FCG-based plant operates in the normal LVRT control method and the PCFR method, respectively.

In the table, relay R_1 shows poor measurement accuracy in the fault distance when the normal LVRT control is used in the FCG-based plant. For the remote faults located at point $F4$, the relay R_1 will mal-operate due to the severe over-reaching problems. In contrast, relay R_1 performs clearly improved measurement accuracy with the collaboration of the PCFR method [100].

6.4.2. OPAL-RT PLATFORM SIMULATION

In this section, the real-time simulation platform from Opal-RT is adopted to assess the proposed PCFR method dynamically. The RT-LAB is the model-based software package in the simulation system platform, used for the hardware-in-the-loop verification, the rapid control systems design and test, as well as the protection systems, etc. [119].

Since RT-Lab fully combines the powerful simulation software Matlab/Simulink, one can use Simulink as a platform for system-level design and simulation. Being different from the non-real-time simulation under Simulink based on the Windows operation system, Redhawk and QNX operating systems are commonly selected to implement the real-time Application for Opal-RT.

After the simulation model is first built in Simulink, one needs to divide the complex model into multiple top-level subsystems such as the console subsystem, the main computing subsystem, and the auxiliary computing subsystem according to the number of host computers and target computers. All top-level subsystems must be named with a prefix to distinguish their functions.

The naming prefix of the console subsystem is "SC_", which is the subsystem running on the host computer, including all simulation modules of acquiring and monitoring data (oscilloscope, manual switch, column workspace, print block, etc.). The naming prefix of the main computing subsystem is "SM_", running on a certain target computer and containing the computing nodes of the model. The naming prefix of the auxiliary computing subsystem is "SS_", which also runs on the target computer. The data exchange between the console and other subsystems is through Ethernet in the asynchronous operation mode, while the data exchange between the main computing subsystem and the auxiliary computing subsystem is based on the FireWire, being synchronous. One simulation model can only have one console subsystem and one main computing subsystem but can have multiple auxiliary computing subsystems.

However, the number of auxiliary computing subsystems is limited by the target computer and the number of its central processing units, that is, the total number of computing subsystems must not be larger than the total central processing units in the target computer. In this chapter, the 220 kV test model is encapsulated into one main computing subsystem and one console subsystem, as depicted in Figure 6-4. X/R ratio of the equivalent source is set as 8 (see voltage level of 220 kV in Table 5-1). The line parameters in per km listed in Table 5-2 are used in this model.

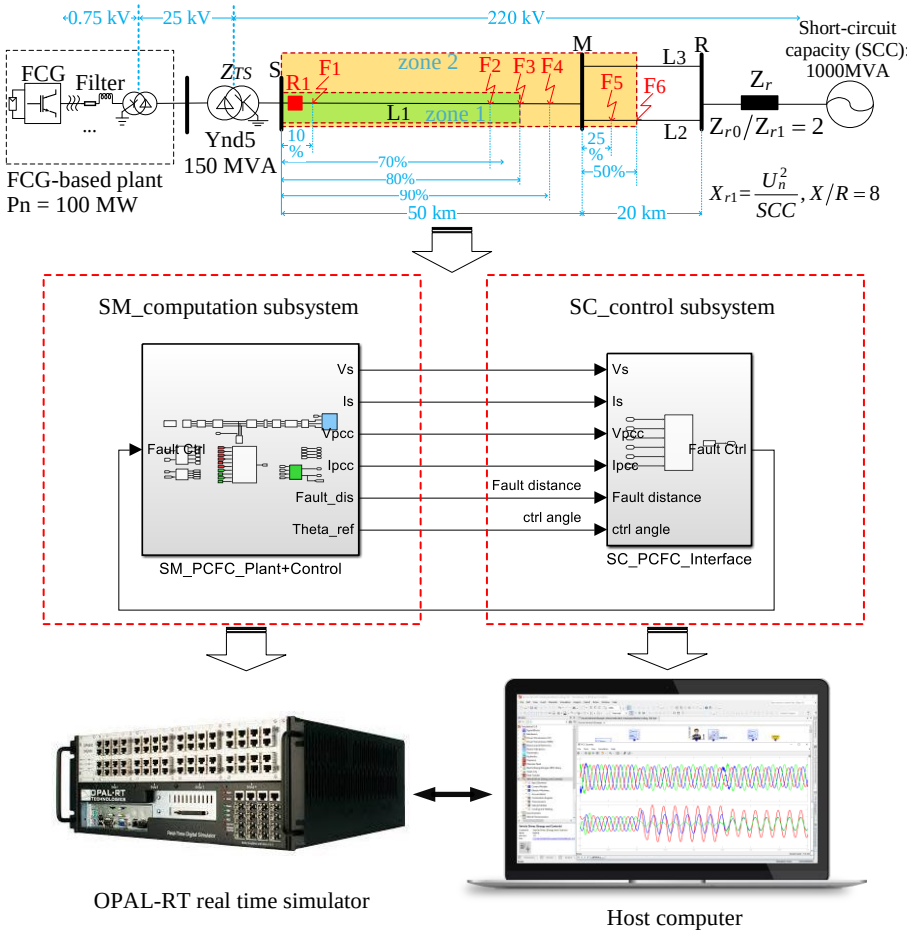

Figure 6-4 Block diagram of Simulink model after segmentation.

A. Normal FCG operation

The proposed fault control method has a fast regulation rate. This can be seen from the dynamic results for the fault AG ($R_f = 50\ \Omega$) located at $F4$, as displayed in Figure 6-5. For this fault, it occurs at 0.105 s. The proposed PCFR method is activated at 0.25

s, while the FCG operates in the normal LVRT method before this time [100]. From the current phasor plots shown in Figure 6-5 (a), one can see that the PCFR method mainly regulates the positive sequence current of FCG. In Figure 6-5 (b), the control angle decreases from a non-zero value to zero rapidly after 0.25 s, indicating that the PCFR achieves the steady-state control target of (6.10) after a short adjusting period. In addition, the fault distance measured by the relay R_1 during the fault AG is depicted in Figure 6-5 (c). The fault distance measurement converges from the initial steady-state value (around 0.62 p.u. under the normal LVRT) to a new steady state, while the new value is much closer to its real value of 0.9 p.u..

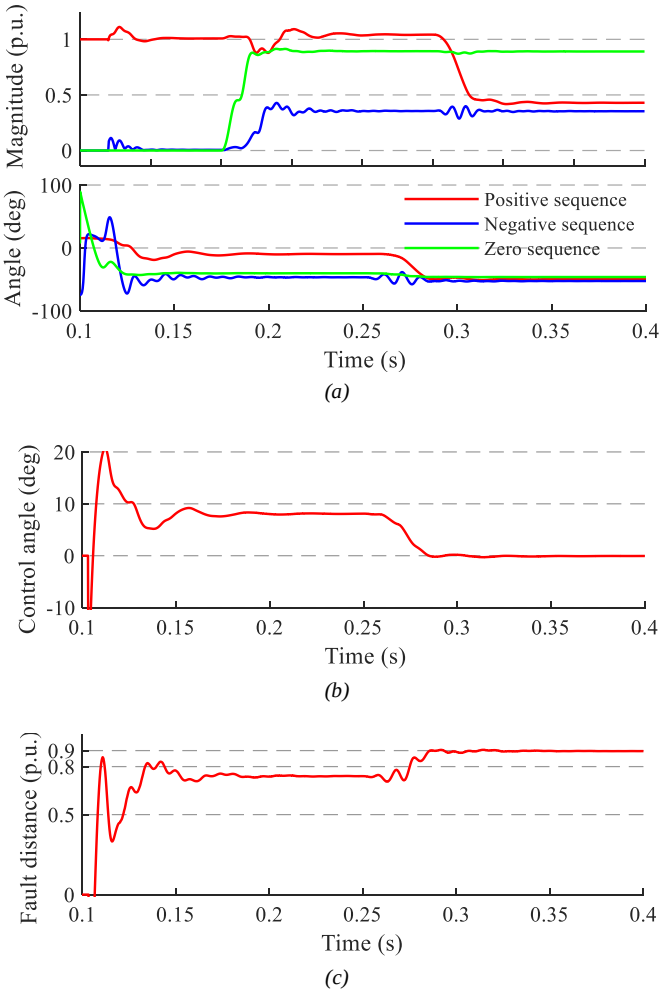

Figure 6-5 Dynamic performance of PCFR during fault AG at point F4, $R_f = 50\Omega$. (a) Sequence currents at FCG side (b) Dynamic control angle (c) Measured fault distance

Meanwhile, the same fault AG located at $F4$ with different fault resistances, e.g. $R_f = 10\ \Omega, 50\ \Omega, 100\ \Omega$, are tested for the comparison purpose. Faults in these cases all occur at 0.105 s and the PCFR method is activated at 0.25 s.

As shown in Figure 6-6 (a), the control angles under the tested three resistive faults all start to converge to zero after the PCFR is activated at 0.25 s. Under normal LVRT control mode, the larger the fault resistance is, the shorter the fault distance measured by relay R_1 is, as depicted in Figure 6-6 (b). At the same time, one can see that the relay even faces the over-reaching problem during those two faults with larger fault resistance, i.e. $50\ \Omega$ and $100\ \Omega$. However, the measured fault distances show highly improved accuracy under PCFR mode, compared with the initial distance measurements.

This case proves that the proposed PCFR method performs excellent robustness to fault resistance.

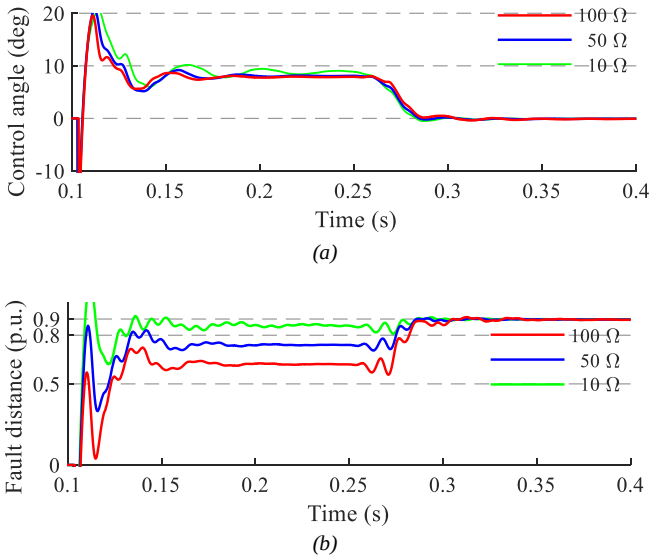

Figure 6-6 Dynamic performance of PCFR during different resistive fault AG at point F4. (a) Dynamic control angle (b) Measured fault distances

Except for the above tested L-G fault, a L-L-G fault BCG located at $F4$ ($R_f = 20\ \Omega$) and a L-L fault BC located at $F3$ ($R_f = 10\ \Omega$) are also tested, and the simulation results are displayed in Figure 6-7 and 6-8 respectively. From Figures 6-7 and 6-8, one can see that the control angles gradually converge to zero after the FCG control is switched to PCFR at 0.25 s. For both the fault scenarios, relay R_1 always 'sees' the accurate fault distances finally.

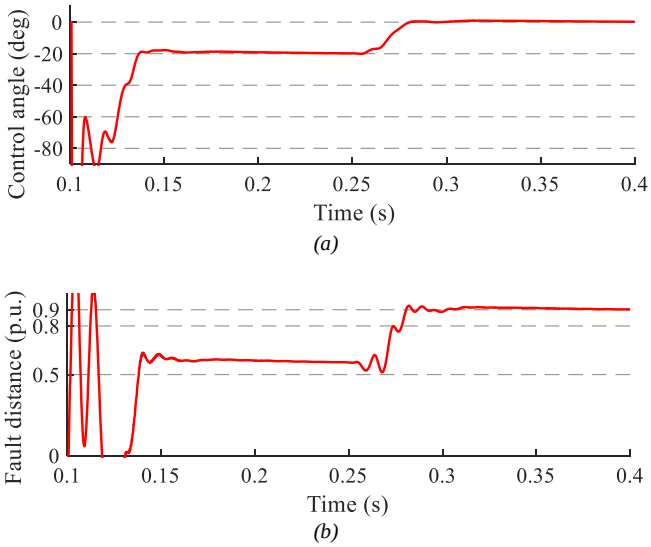

Figure 6-7 Dynamic performance of PCFR during fault BCG at point F4, $R_f = 20\Omega$. (a) Dynamic control angle (b) Measured fault distance

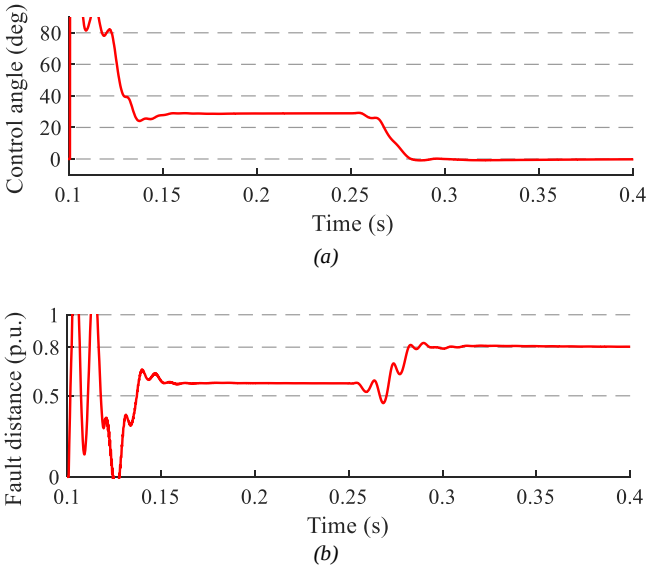

Figure 6-8 Dynamic performance of PCFR during fault BC at point F3, $R_f = 10\Omega$. (a) Dynamic control angle (b) Measured fault distance

In addition, a downstream line fault BC located at *F*5 is tested to see the performance of the PCFR method. In Figure 6-9 (a), the control angle is regulated towards zero

rapidly after the PCFR is activated at 0.25 s. Correspondingly, the measured fault distance is initially 0.8 p.u., namely, a boundary fault is initially 'seen'. However, it finally stabilizes around 1.33 p.u., as displayed in Figure 6-9 (b).

As depicted in Figure 6-4, the real fault distance for the fault position of $F5$ is 1.1 p.u. Although the finally measured fault distance indicates that an external fault will be detected, however, the measured fault distance is relatively larger than its real value. Here, one can at least see that such measurement error of the fault distance during the downstream line fault does not bring in the malfunction risk for the distance relay. In fact, this measuring error is caused by the effects of intermediate in-feed, which is discussed in section 6.4.3-C in detail.

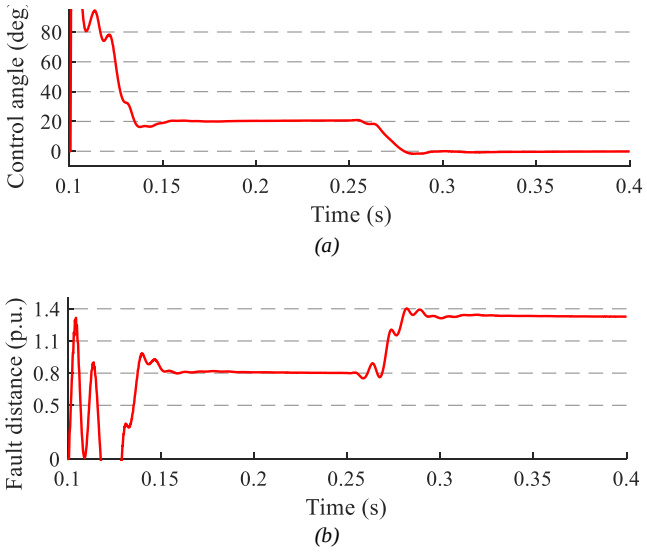

Figure 6-9 Dynamic performance of PCFR during a zone 2 fault BC at point F5, $R_f = 20\Omega$. (a) Dynamic control angle (b) Measured fault distance

B. Flexible FCG operation

As mentioned in section 1.3.1, the PEC devices are weak to handle the severe fault system condition. One of the typical scenarios is that the in-service under-voltage and overcurrent fault limits to protect PECs can lead to varying operations of FCG-based plant. In this subsection, the effects of flexible operations of FCG-based plant on the proposed PCFR method are further investigated.

Take the L-L-G fault BCG located at $F3$ ($R_f = 50\ \Omega$), for example. The detailed FCG operating event is described as follows:

1) Fault occurs at 0.102 s, and PCFR is activated at 0.25 s.
2) Half of the generating units in the FCG plant are tripped at 0.38 s.

Simulation results are given in Figure 6-10. During the normal LVRT control period, the fault distance measured by relay is lower than the threshold of zone 1 (0.8 p.u.). After 0.25 s, one can see that the control angle is regulated to zero and the measured fault distance converges to its real value of 0.8 p.u. Subsequently, half of FCG units are tripped at 0.38 s, which leads to the decrease of PCC currents, as depicted in Figure 6-10 (c). This brings in the obvious fluctuations in control angle and the measured fault distance. However, these two quantities stabilize at the same position after short adjustments. Dynamic results prove the robustness of PCFR to the flexible operation of FCG plant [100].

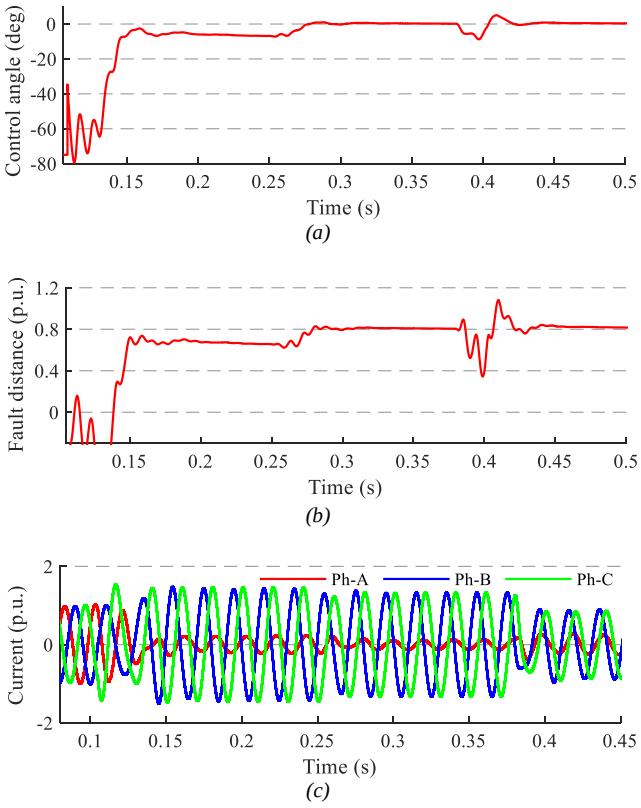

Figure 6-10 Dynamic performance of PCFR for fault BCG at point F3 ($R_f = 50\Omega$), in the case of flexible FCG operation. (a) Dynamic control angle (b) Measured fault distance (c) Instantaneous PCC currents

In addition, the robustness of the PCFR method is also tested via a L-L fault BC located at point $F3$ ($R_f = 15\ \Omega$), as shown in Figure 6-11. Clearly, the new method is also effective to improve the relay performance and is unaffected by the flexible operation of FCG-based plant, as depicted in Figure 6-11 (a), (b). In this test, one can see that the fault current through PCC decreases a lot, if comparing Figure 6-11 (c) to Figure 6-10 (c). This is due to the missing of zero-sequence current during the L-L fault.

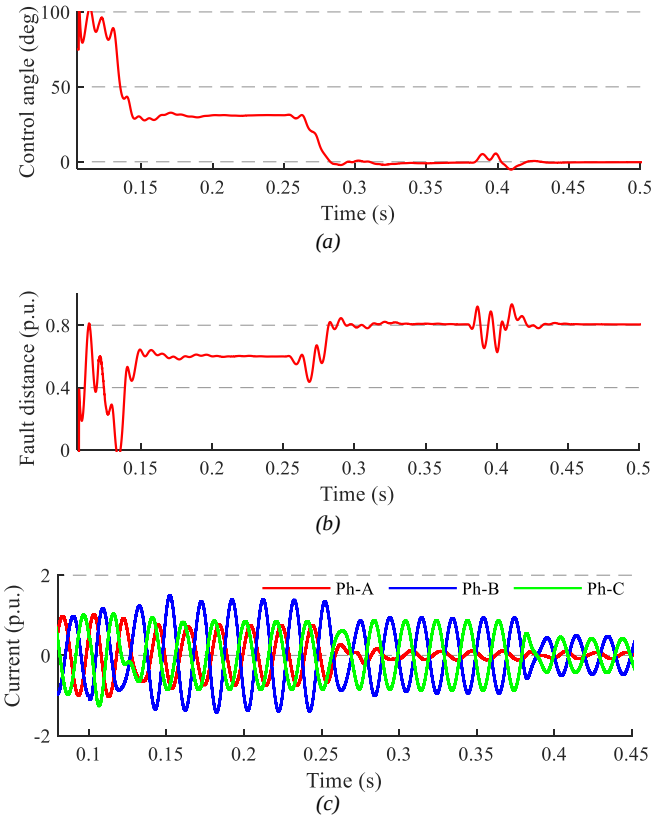

Figure 6-11 Dynamic performance of PCFR for fault BC at point F3 (R_f =15Ω) with the consideration of flexible FCG operation. (a) Dynamic control angle (b) Measured fault distance (c) Instantaneous currents at FCG side

C. BCC strategy in FCG

In section 4.3.4, the estimation for the ITA (i.e. θ_{Imp}) in the presence of BCC strategy has been revised. Following the derivations of angular reference θ_{ref} of positive sequence current regarding the FCG's DSC strategy (eq. (6.9)~(6.12)), one can also

obtain the corresponding angular reference θ_{ref} by substituting (6.9) into (4.23)~(4.25) for the deployment of BCC strategy in FCGs. This will not be further discussed here.

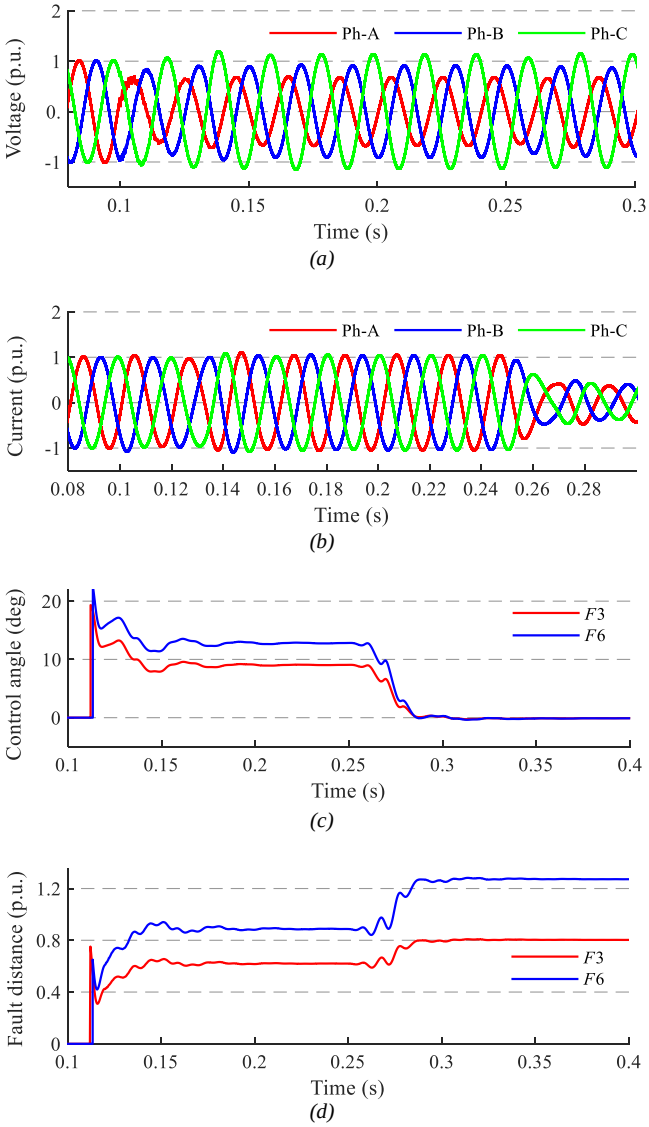

Figure 6-12 Dynamic performance of PCFR for fault AG at different points ($R_f = 50\Omega$), in the presence of BCC strategy in FCGs. (a) PCC voltage (b) Current of FCG-based plant at low voltage side (c) Dynamic control angle (b) Measured fault distance

Take the L-G fault AG ($R_f = 50\,\Omega$) occurring at $F3$ and $F6$, for example. The proposed PCFR is validated here, and simulation results are displayed in Figure 6-12. Subplots (a) and (b) are the instantaneous PCC voltage and FCGs' current (at low voltage side) for the fault condition at point $F3$. Clearly, one can see that the FCGs only output the positive sequence current, regardless of the unbalanced PCC voltage after fault occurs (at 0.1s). And, one can also see the current variation after the FCG control switching from normal LVRT to PCFR at 0.25s. Correspondingly, for the fault at point $F3$, the control angle is adjusted to zero rapidly and the measured fault distance increase from an initial value (around 0.6 p.u.) to an accurate one (0.8 p.u.), as depicted in subplots (c) and (d). This boundary fault will be correctly detected by relay. Beasides, for the external fault at $F6$, one can also see the effectiveness of proposed PCFR from the variations of control angle and measured fault distance depicted in subplots (c) and (d).

6.4.3. INFLUENCE OF PARAMETER M SELECTION

According to the error characteristics of estimated ITA (i.e. θ_{Imp}) in section 5.2.4 of chapter 5, one may infer that the proposed PCFR will also cause a certain influence on distance relay regarding the measurement of fault distance. Similarly, the error properties of proposed PCFR are organized in the view of local line faults and downstream line faults, separately.

A. Local line faults

In the studies of sections 6.4.1 and 6.4.2, a constant m representing the zone 1 length is in use to initialize the current distribution factors for the fault control method. Using the definitions in section 5.2.4-A, the relative effects of the initialization using a constant parameter *m* on the PCFR method are analyzed here. Take the L-G fault AG, for example. At the control steady-state, if the PCFR achieves the control target (6.10), one has,

$$angle\left\{\left[\frac{\dot{I}_{1S}+\dot{I}_{2S}}{\dot{I}_{0S}}+(1+K_0)\right]\cdot D_0\big|_{m=real\_fault\_distance}\right\}-\delta_{D_0}=0 \tag{6.13}$$

For the source impedance condition of $X/R = 8$ in this chapter, the angular error δ_{D_0} can be deemed as a monotonically increasing function of fault distance *m* (Figure 5-16). At the fault point where $m = m_{[0]}$, it crosses 0. This in turn brings in the error of apparent reactance, meeting a monotonically decreasing property [100]. On the complex plane, one knows that the error of apparent reactance is inversely proportional to the sine function of δ_{D_0} (since δ_{D_0} locates in the denominator of R_f-related modulating impedance item). On the other hand, δ_{D_0} generally varies in a small range (referring to the analysis at the end of section 5.2.4-A), meaning

$sin(\delta_{D_0}) \approx \delta_{D_0}$ is valid. Thus, one may infer that the apparent reactance error, i.e. the error of measured fault distance, has a tiny magnitude. And, one can conclude:

1) For internal faults, $m < m_{[0]}$, measured fault distances will be slightly larger than the corresponding real fault distances.
2) For boundary faults, $m = m_{[0]}$, measured fault distances have the highest accuracy.
3) For external faults, $m > m_{[0]}$, measured fault distances will be slightly smaller than their real values.

This can be seen from the following test scenario of L-G fault AG ($R_f = 100\ \Omega$), where several fault positions along the local line, i.e. 0.1 p.u., 0.5 p.u., 0.7 p.u., and 1 p.u., are considered. Here, all faults occur at 0.105 s, and PCFR is activated at 0.25 s. The measured fault distances are depicted in Figure 6-13.

In the figure, the measured fault distances marked in solid correspond to the condition of constant m initialization, which accords with the above error analysis. In addition, one can see that the slight error of measured fault distances does not affect the distance relay to detect faults.

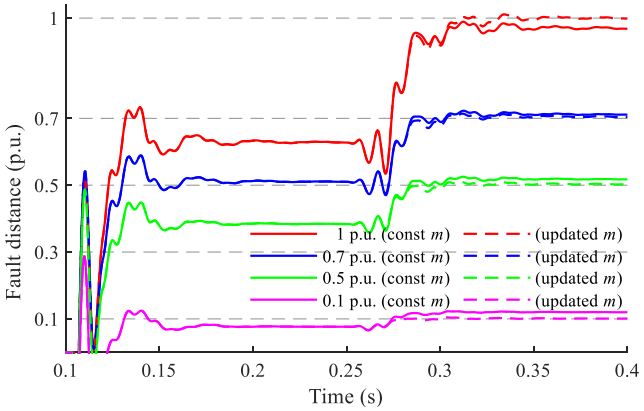

Figure 6-13 Comparison of measured fault distances for L-G fault AG at different positions.

B. Improvement

Actually, one can update the parameter m used in the current distribution factors with the calculated value in the previous step. The flowchart of the varying parameter m based PCFR is given in Figure 6-14.

To validate the varying parameter m based PCFR method, the fault scenarios in Figure 6-13 are re-tested, and the measured fault distances are plotted in the same

figure (see the dashed distance curves). From the figure, one can see that the difference occurs after the PCFR is activated. Compared to the measured fault distances in the case of constant m based PCFR, the steady-state measurements in the case of varying m based PCFR show the improved accuracy, while both the dynamic processes are similar. This is true for all the tests at different fault positions.

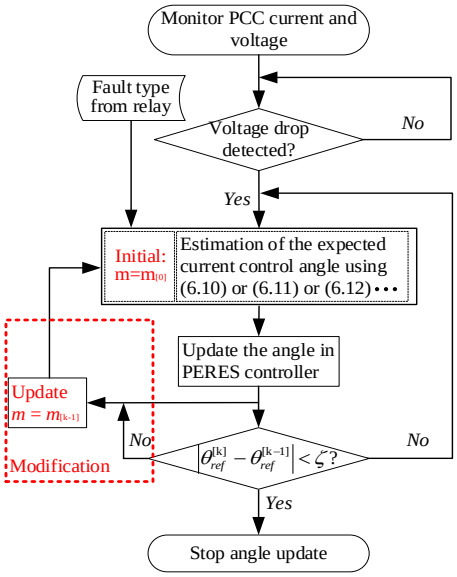

Figure 6-14 Flowchat of the varying parameter m based PCFR method.

One thing should be mentioned is that, a limiter of 1 p.u. is needed when updating the parameter *m*, since the above improvement is expected valid for local line faults only.

C. Downstream line faults

As discussed in the section 5.2.4-B of chapter 5, the intermediate in-feed is the critical factor that will affect the real tilt of apparent impedance during downstream line faults. Similarly, the influence of intermediate in-feed on the PCFR method is qualitatively analyzed. Following the same definitions in section 5.2.4-B, the angular inequality (5.12) of small resistive fault is re-written as,

$$\begin{aligned} angle\left(\Delta Z_{im}+\Delta Z\right) &\approx angle\left(\Delta Z_{im}\right)=angle\left(\frac{\dot{I}_{im}}{\dot{I}_s}\right)+angle\left(Z_L\right)\gg angle\left(\frac{\dot{I}_{im}}{\dot{I}_s}\right) \\ &\approx angle\left(\frac{\dot{I}_{im}+\dot{I}_r}{\dot{I}_s}\right)\approx angle\left(\frac{\dot{I}_{im}+\dot{I}_r+\dot{I}_s}{\dot{I}_s}\right)=angle\left(\Delta Z\right) \end{aligned} \quad (6.14)$$

As concluded in section 5.2.4-B, $angle(\Delta Z)$ is much smaller than $angle(\Delta Z_{im} + \Delta Z)$ under such small resistive fault condition. Assume that the control target (6.3) is achieved after the regulation of PCFR enters the steady state, meaning $angle(\Delta Z)$ approaching zero. From (6.14), one may then infer $angle(\Delta Z_{im} + \Delta Z)$ representing the real tilt of apparent impedance is larger than zero. In other words, the relay will 'see' further fault distance than the real distance value. This can be seen from the previously tested L-L fault BC on the downstream line (Figure 6-9).

However, if considering a fault with fault resistance being large enough, the real tilt of apparent impedance will approach zero after the regulation of PCFR enters the steady state, since $angle(\Delta Z) \approx angle(\Delta Z_{im} + \Delta Z)$. Under such condition, the effect of intermediate in-feed tends to disappear.

In a word, the smaller the fault resistance is, the heavier the effect of intermediate in-feed is. This is further proven in the following test, where two resistive fault AG located at $F6$ are compared. In Figure 6-15 (a), the control angles for both the resistive fault scenarios approach towards zero rapidly after the PCFR is activated at 0.25 s. Under such condition, measured fault distances stabilizes at different values, as shown in Figure 6-15 (b). Comparatively speaking, relay measures further fault distance in the fault scenario of $R_f = 10\,\Omega$, showing bigger measurement error. (For fault position $F6$, the real fault distance is 1.2 p.u.).

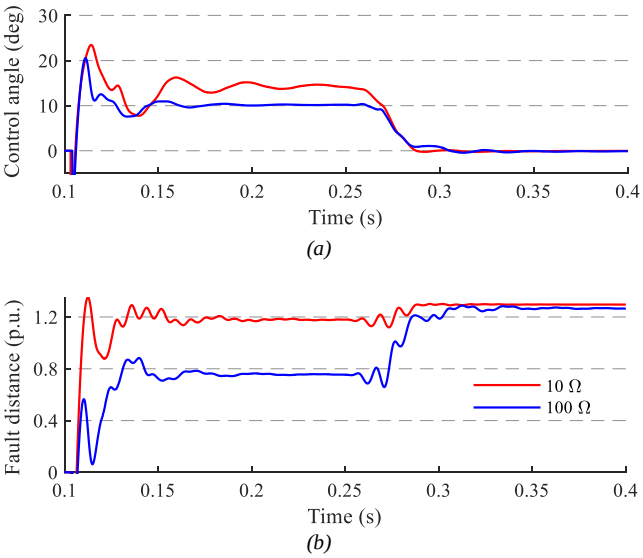

Figure 6-15 Dynamic performance of PCFR during a downstream line fault AG at point F6. (a) Dynamic control angles (b) Measured fault distances

6.5. DISCUSSION

In this chapter, the PCFR method for FCG is designed with the combination of the demands of vicinal distance protection. The PCFR method regulates the positive sequence current angle of FCG in the rotating reference frame after grid faults, working for the reduction of the relay's measurement error on fault distance [100]. One can outline the **properties** of the proposed PCFR method for FCG as follows:

1) Benefiting from the proposed PCFR method, distance protection shows high measurement accuracy on fault distance during the grid faults (occurring in the local line), improving the relay reliability effectively [100]. And,
2) This is more prominent for the varying parameter based PCFR method.
3) For downstream line faults, the inherent error characteristics resulted from the intermediate in-feed can lead to the enlargement of measured fault distances (especially for small resistive faults). Such effects in fact equate to the enhancement of relay reliability, which is similar to the ITA-21 in Chapter 4 and the proposed tilt setting method of PZTL in Chapter 5.
4) In this chapter, PCFR is implemented on the premise of having known the equivalent impedance of the external grid. So does the ITA-21 in Chapter 4 and the proposed tilt setting method of PZTL in Chapter 5. Thus, the first step to implement these new protection/control methods is the reduction of the system emanating from FCG-based plant into a "two machine" configuration. Based on this, the equivalent sequence parameters of the external source should be estimated. For this, the estimation method based on the short-circuit power of in-feed networks has been mentioned in [104]. In addition, many reported grid impedance monitoring methods applicable to the power system integrating FCGs can also guarantee feasibility [120-121].
5) Moreover, the fault type is assumed to be known. For this, the communication link between the FCG control system and the vicinal protection devices is needed. Otherwise, the FCG control system needs to integrate the function of fault phase selector. Many new fault classifier methods suitable for the FCG-integrated system are available [122-123].

Limitation statement:

PCFR adopts the current distribution factors in the zero or (and) negative sequence fault loop(s) in the regulation process. As a result, it is invalid for L-G (or L-L-G) faults in the system without grounding connections. So do the 3PH grid faults, where it remains an open-circuit condition in the FCG plant side negative-sequence circuit [100]. This is also similar to the ITA-21 in Chapter 4 and the proposed tilt setting method of PZTL in Chapter 5.

CHAPTER 7. CONCLUSIONS AND FUTURE WORK

Protective relaying determines whether to isolate the faulty electrical component by sensing fault characteristics. However, one of the evident features in modern power systems is the large-scale integration of NSGs, resulting in the drastic change of fault characteristics compared with the SG-dominated system. Looking back, the thesis studied the protective issues induced by the presence of FCG-based plant in transmission networks, which follows three steps, i.e. analysis of FCG's short-circuit model(s), challenge assessment on conventional network protections (i.e. line current differential protection and distance protection), and developments of novel protection/control schemes. Now, I will summarize where I believe the work contributes and where it is falling short.

In the first step, the deduced short-circuit models of FCG follow the typical fault control rules during LVRT, which helps to assess the influence of diverse FCG controls on the conventional network protections. More importantly, the derivated models effectively support the developments of the distance protection-related novel schemes in below. Since the thesis concerns the protective issues in the transmission network only, considering the fault regulation rules of FCG during LVRT period in the modeling is reasonable. However, the short-circuit models may not be the same for the FCG integrated in distribution networks or micro-grids due to the possibly different regulation rules.

In the second step, the challenges of conventional network protections in the power network connecting FCG-based plants are assessed in the Chapter 2. In detail,

- In the presence of BCC strategy, FCG fault control probably leads to the sensitivity problem of line current differential protection, especially during L-L grid faults. This is because of the evidently different current components sensed by 87L. Such relay sensitivity highly relates to the regulation of FCG's active current in positive sequence system. Simulation analysis proves that the reduction of positive sequence active current from FCGs during faults can improve the relay sensitivity.
- Distance protection in the line emanating from the FCG-based plant probably faces the reliability problems, known as relay over- or under-reach. Such relay reliability issues, resulted from the measured 'virtual' reactance, critically depend on two factors. 1) The control angle of FCG's positive sequence current, i.e. $atan\left(\frac{I''_{q1g}}{I''_{d1g}}\right)$, determines the direction of 'virtual' reactance, which further causes different 'reach' problem of relay against

different fault positions. 2) Fault resistance is proportional to this 'virtual' reactance in magnitude.

In this step, I just adopt several (but typical) simulation scenarios to catch a glimpse of the existing protective challenges, due to the limited space. The diversity of existing relays and the other functional elements in these relays are not considered.

In the third step, some new contributions, e.g. novel differential protection scheme, the improvements of distance protection, and the upgrade of FCG control, are presented based on the protective challenges analyzed in the previous step (Chapters 3-6).

Based on the sensitivity consideration of the conventional current comparison-based differential protection, a novel compensated current-based differential principle in time-domain is presented in Chapter 3. To enhance the reliability of the new differential principle, the restraining equation is introduced, which is subsequently refined for the application in power grids connecting FCG-based plant. Simulation studies validate the robustness of the new differential protection scheme to the diverse control of FCG. This benefits from the idea of fault detection by the mapping index of fault sampling to network model. In this part, what is overlooked is the possibility of non-homogeneous (or geometrical asymmetry) transmission system configuration.

To tackle the reliability problem of distance protection in the transmission line connecting FCG-based plant, two different protective solutions for the resistive grid faults are proposed in Chapters 4 and 5, respectively. The similarity of these two solutions is that the FCG control-caused tilting characteristics of relay's apparent impedance are combined with the protection design.

- In Chapter 4, the proposed impedance tilt angle-based distance protection directly adopts the different tilting tendencies of apparent impedance during internal and external faults. Such tilting tendencies of apparent impedance follow a constant regularity and are unaffected by the FCG control in nature.
- In Chapter 5, an adaptive tilt setting scheme for the polygonal distance relay is presented. In contrast to the method of Chapter 4, the tilting angle of apparent impedance is used as a reference to adjust the polygonal zone top-line. Thus, the adaptive zone tilt method of PZTL can be deemed as an 'active' approach for the compensation of possible relay over- or under-reach.

In fact, both the new methods are specially developed as supplementary functions of the conventional distance protection, so that the possible relay reliability issue (over- or under-reach) can be dealt with. Simulation studies validate these two protective solutions from different aspects, including the effectiveness to different tendencies of impedance tilt, the adaptability to possibly different deployments of FCG control

strategy, the robustness to the intermittent characteristics of FCG, and the qualitative error analysis to the intermediate in-feed and to the different R/X ratios of external grid. For the application in transmission level, these two solutions fall short of handling the symmetrical grid faults.

In addition, benefiting from the analysis on the over- or under-reaching problem of distance relay against the control angle of FCG's positive sequence current in Chapter 2, a novel FCG fault control is proposed in Chapter 6. The designed FCG control method balances the operating objective of FCG fault control (i.e. the reactive current regulating rules) with the objective of minimizing error of reactance measurement in distance protection. In the effectiveness validation, except for the simulation study in DIgSILENT/PowerFactory, the dynamic performance of the proposed FCG fault control is also evaluated by performing the real-time simulation in Opal-RT platform. The obtained results further validate its authenticity. One application premise is that the FCG control system needs information about the fault type. This can be solved by either communicating with the local distance protection or deploying the fault classifier in itself. For application in transmission level, the novel FCG fault control cannot deal with the symmetrical faults, either.

The future work can be drawn as, but not limited to, the following aspects:

- ✓ The generic extension of the modeling analysis for distributed FCG in distribution level (or micro-grid) can be one of the research topic.

- ✓ The non-homogeneous (or geometrical asymmetry) configuration in the modern transmission system is a practical issue, e.g. some offshore wind parks are often connected to the over-head line dominated main grid through underground cables. Thus, the limitation of the proposed compensated current-based differential protection scheme in such hybrid system condition needs to be considered further.

- ✓ In addition, some improvements for the developed distance protection-related solutions in chapters 4, 5, and 6 are also necessary. For example,

    - The application limits to symmetrical faults in transmission level.
    - More complicated application scenes, e.g. ring bus-bar, double-circuit line, series-compensated lines, etc., should be taken into consideration.
    - Compute efficiency and stability of these new approaches also need further validation in the prototype-based test level with optimal testing methods.
    - The extension for the distributed FCG installation in distribution networks.

LITERATURE LIST

[1] ENTSO-E for the Research, Development & Innovation Roadmap 2020-2030.

[2] ENTSO-E Vision 2030: The ratio of non-synchronous (power electronics) generation to total generation in 2030 will vary from 25% for the Nordic area to around 50% for Continental Europe, the Baltic area, Great Britain, and Ireland.

[3] Denmark's integrated national energy and climate plan, Dannish Ministry of Climate, Energy and Utilities, Dec., 2019.

[4] Y. Sun, Z. Wang, C. Long, G. Li, D. Xia and Y. Li, "Method for Power Flow Controller Location-Allocation and Optimized Flow Control method of Meshed DC Grid," *2019 4th IEEE Workshop on the Electronic Grid (eGRID)*, 2019, pp. 1-6.

[5] P. Li, W. Sheng and Q. Duan, "Optimal Power Flow Calculation Method for AC/DC Hybrid Distribution Network Based on Power Router," *2021 6th Asia Conference on Power and Electrical Engineering (ACPEE)*, pp. 1694-1699, 2021.

[6] K. Zhou, Q. Jin, Z. Lan, C. Tu, M. Guo and G. Liu, "The study of power electronic transformer on power flow control and voltage regulation in DC micro-grid," *2015 5th International Conference on Electric Utility Deregulation and Restructuring and Power Technologies (DRPT)*, pp. 2166-2172, 2015.

[7] X. Xu, Y. Jia, Z. Xu and J. Li, "Optimal Unified Power Flow Controller Planning in Transmission Grids with Uncertainty Consideration," *2020 IEEE/IAS Industrial and Commercial Power System Asia (I&CPS Asia)*, pp. 1689-1695, 2020.

[8] M. Herrmann and L. Hofmann, "Ensuring Short-term Voltage Stability in Extensive Grids With High Power Electronic Penetration by Applying Grid Forming Controls," *2020 International Conference on Smart Grids and Energy Systems (SGES)*, pp. 24-29, 2020.

[9] M. A. Garnica López, J. L. García de Vicuña, J. Miret, M. Castilla and R. Guzmán, "Control Strategy for Grid-Connected Three-Phase Inverters During Voltage Sags to Meet Grid Codes and to Maximize Power Delivery Capability," *IEEE Transactions on Power Electronics*, vol. 33, no. 11, pp. 9360-9374, Nov. 2018.

[10] J. Fang, H. Li, Y. Tang and F. Blaabjerg, "On the Inertia of Future More-Electronics Power Systems," *in IEEE Journal of Emerging and Selected Topics in Power Electronics*, vol. 7, no. 4, pp. 2130-2146, Dec. 2019.

[11] K. A. Kumar, P. Kushwaha, V. Prakash, R. Bhakar, H. Tiwari and K. G. Sharma, "Inertia Emulation Trends in Low Carbon Power System," *2019 8th International Conference on Power Systems (ICPS)*, pp. 1-6, 2019.

[12] V. Telukunta, J. Pradhan, A. Agrawal, et.al. "Protection challenges under bulk penetration of renewable energy resources in power systems: A review," *CSEE Journal of Power and Energy Systems*, vol. 3, no. 4, pp: 365-379, 2017.

[13] J. Yang, J. E. Fletcher, and J. O Reilly, "Short-Circuit and Ground Fault Analyses and Location in VSC-Based DC Network Cables," *IEEE Transactions on Industrial Electronics*, vol. 59, no. 10, pp. 3827 3837, Oct. 2012.

[14] J. Keller and B. Kroposki, Understanding Fault Characteristics of Inverter-Based Distributed Energy Resources, National Renewable Energy Laboratory (NREL), NREL/TP-550-46698, 2010.

[15] X. Li, Y. Lu, T. Huang, "Impact of the DFIG-Based Wind Farm Connection on the Fault Component-Based Directional Relay and a Mitigation Countermeasure", *Energies*, vol. 13, no.17, 4414, 2020.

[16] C. Wang, G. Song, Y. Chi, et al. "Fault characteristics analysis of wind power system," *Automation of Electric Power Systems*, vol. 39, no. 21, pp. 52-58, 2015. (In Chinese)

[17] X. Tian, G. Li, Y. Chi, W. Wang, H. Tang and X. Li, "Voltage phase angle jump characteristic of DFIGs in case of weak grid connection and grid fault," in Journal of Modern Power Systems and Clean Energy, vol. 4, no. 2, pp. 256-264, April 2016, doi: 10.1007/s40565-015-0181-4.

[18] R. Li, C. Booth, A. Dyśko, A. Roscoe, H. Urdal and J. Zhu, "A systematic evaluation of network protection responses in future converter-dominated power systems," *13th International Conference on Development in Power System Protection 2016 (DPSP)*, pp. 1-7, 2016.

[19] H. H. Zeineldin, Y. A. R. Mohamed, V. Khadkikar, and V. Ravikumar Pandi, "A protection coordination index for evaluating distributed generation impacts on protection for meshed distribution systems," *IEEE Transactions on Smart Grid*, vol. 4, no. 3, pp. 1523–1532, Sep. 2013.

[20] S. M. Brahma and A. A. Girgis, "Development of adaptive protection scheme for distribution systems with high penetration of distributed generation," *IEEE Transactions on Power Delivery*, vol. 19, no. 1, pp. 56–63, Jan. 2004.

[21] B. Li, J. He, Y. Feng, et al., "Key techniques for protection of multi-terminal flexible DC grid", *Automation of Electric Power Systems*, 2016, vol. 40, no. 21, pp. 2-12, 2016. (In Chinese)

[22] J. Qin, M. Saeedifard, A. Rockhill, et al., "Hybrid design of modular multi-level converters for HVDC systems based on various submodule circuits", *IEEE Transactions on Power Delivery*, vol. 30, no. 1, pp. 385-394, 2015.

[23] X. Fang, C. Chen, Z. Wang, J. Xiong, K. Zhang, "An Improved Modular Multilevel Converter with DC Fault Blocking Capability Based on Half-Bridge Submodules and H-Bridge Circuit", *IEEE Transactions on power delivery*, vol. 35, pp. 2682-2691, 2020.

[24] Y. Pang, G. Ma, X. Liu, X. Xu, X. Zhang, "A new MMC sub-module topology with DC fault blocking capability and capacitor voltage self-balancing capability", *Energies*, vol. 14, no. 12, 3049, 2021.

[25] J. Sun, M. Li, Z. Zhang, et al., "Renewable energy transmission by HVDC across the continent: system challenges and opportunities," *CSEE Journal of Power and Energy Systems*, vol. 3, no. 4, pp. 353-364, Dec. 2017.

[26] *Nordic and Baltic Grid Disturbance Statistics 2019*. https://euagenda.eu/upload/publications/nordic_and_baltic_grid_disturbance_statistics_2019_22.10.2020.pdf, Sep. 2020.

[27] Vladislav Akhmatov. *Induction Generators for Wind Power*. Emerald Publishing Limited, Jun. 2007, ISBN: 9780906522400

[28] F.M. Hughes, O. Anaya-Lara, N. Jenkins, G. Strbac, "Control of DFIG based wind generation for power network support," *IEEE Transactions on Power system*, vol. 20, no. 4, pp. 1958–1966, 2005.

[29] M.M. Hossain, M.H. Ali, "Future research directions for the wind turbine generator system," *Renewable and Sustainable Energy Reviews*, vol. 49, pp: 481–489, Sep. 2015.

[30] K. I. Jennett, C. D. Booth, F. Coffele, and A. J. Roscoe, "Investigation of the sympathetic tripping problem in power systems with large penetrations of distributed generation," *IET Generation, Transmission Distribution*, vol. 9, no. 4, pp. 379–385, 2015.

[31] X. Liu, Z. Xu, K. P. Wong, "Recent advancement on technical requirements for grid integration of wind power," *Journal of Modern Power System and Clean Energy*, vol. 1, no. 3, pp: 216–222, 2013. DOI 10.1007/s40565-013-0036-9

[32] R. Cardenas, R. Pena, S. Alepuz, G. Asher, "Overview of control systems for the operation of DFIGs in wind energy applications," *IEEE Transactions on Industrial Electronics*, vol. 60, no. 7, pp. 2776–2798, 2013.

[33] *Network Code on Requirements for Grid Connection applicable to all Generators*. ENTSO-E, Mar-2013. Available at: http://networkcodes.entsoe.eu /wpcontent/ uploads/2013/08/130308_Final_Version_NC_Rf G1.pdf

[34] H. Wen and S. Cai, "Modeling and LVRT analysis of DFIG wind power system," *2015 IEEE PES Asia-Pacific Power and Energy Engineering Conference (APPEEC)*, pp. 1-5, 2015.

[35] J. Lopez, P. Sanchis, X. Roboam, L. Marroyo, "Dynamic behavior of the doubly-fed induction generator during three-phase voltage dips," *IEEE Transactions on Energy Conversion*, vol. 22, no. 3, pp. 709–717, 2007.

[36] F. Sulla, J. Svensson, O. Samuelsson, "Symmetrical and unsymmetrical short-circuit current of squirrel-cage and doubly-fed induction generators," *Electric Power System Research*, vol. 81, pp. 1610–1618, 2011.

[37] M. Liu, W. Pan and G. Yang, "A new calculation method of short-circuit currents contributed by doubly-fed wind turbines cluster," *2017 IEEE 6th International Conference on Renewable Energy Research and Applications (ICRERA)*, pp. 669-673, 2017.

[38] J. Lopez, E. Gubia, P. Sanchis, X. Roboam, L. Marroyo, "Wind turbines based on doubly fed induction generator under asymmetrical voltage dips," *IEEE Transactions on Energy Conversion*, vol. 23, pp. 321–330, 2008.

[39] B. Li, J. Liu, X. Wang, L. Zhao, "Fault studies and distance protection of transmission lines connected to DFIG-based wind farms," *Applied Sciences*, vol. 8, no. 4, 562, Apr. 2018.

[40] Z. Hao, B. Zhang, and J. Zhang. "Equivalent circuit of DFIG with crowbar protection for relay protection analysis", *13th International Conference on Development in Power System Protection 2016 (DPSP)*, 2016.

[41] IEEE PES Industry Technical Support Task Force, "Impact of Inverter Based Generation on Bulk Power System Dynamics and Short-Circuit Performance," *IEEE*, July 2018.

[42] J. Fortmann, R. Pfeiffer, E. Haesen, F. van Hulle, F. Martin, H. Urdal, and S. Wachtel, "Fault-ride-through requirements for wind power plants in the ENTSO-E network code on requirements for generators," *IET Renewable Power Generation*, vol. 9, no. 1, pp. 18–24, 2015.

[43] K. Jia, L. Hou, Q. Liu, Y. Fang, L. Zheng and T. Bi, "Analytical Calculation of Transient Current from an Inverter-Interfaced Renewable Energy," *in IEEE Transactions on Power Systems*, doi: 10.1109/TPWRS.2021.3107580.

[44] GB/T 19963, *Technical rule for connecting wind farm to power system*, 2011.

[45] Y. Liu, D. Zhao, L. Zhang, “Analysis and Simulation Tools for Short Circuit Dynamic Characteristics of Photovoltaic Power Plants,” *The 1st IEEE Conference on Enery Internet and Enery System Integration EI2*, pp. 1-6, 2017.

[46] H. Hooshyar and M. E. Baran, “Fault analysis on distribution feeders with high penetration of PV systems,” *IEEE Transactions on Power system*, vol. 28, no. 3, pp. 2890–2896, Aug. 2013.

[47] D. F. Howard, “Short circuit currents in wind-turbine generator networks,” Ph.D. thesis, School of Elect. Comput. Eng., Georgia Inst. Technol., Atlanta, GA, USA, Dec. 2013.

[48] M. Fischer and Â. Mendonça, "Representation of variable speed full conversion Wind Energy Converters for steady state short-circuit calculations," *PES T&D 2012*, pp. 1-7, 2012.

[49] Y. Liu, R. Yu, L. Zhang, D. Jiang, N. Chen and D. Zhao, "Research on Short-Circuit Currents Calculation Method Considering Dynamic Reactive Power Support of Renewable Energy Systems," *2018 2nd IEEE Conference on Energy Internet and Energy System Integration (EI2)*, pp. 1-9, 2018.

[50] EPRI, *Impact of renewables on system protection: Wind/PV short-circuit phasor model library and guidelines for system protection studies*, EPRI, Palo Alto, CA, Tech. Rep. 3002008367, 2016.

[51] R. Teodorescu, M. Liserre, and P. Rodriguez, *Grid Converters for Photovoltaic and Wind Power Systems*. Hoboken, NJ, USA: Wiley, 2011.

[52] T. Kauffmann, U. Karaagac, I. Kocar, S. Jensen, E. Farantatos, A. Haddadi, J. Mahseredjian, “Short-circuit model for type-IV wind turbine generators with decoupled sequence control,” *IEEE Transactions on Power Delivery*, vol. 34, no. 5, Oct., 2019.

[53] Paul M. Anderson, *Power System Protection*, IEEE Press power engineering series, New York: McGraw-Hill : IEEE Press, 1999.

[54] S. Miao, P. Liu, and X. Lin, “An adaptive operating characteristic to improve the operation stability of percentage differential protection,” *IEEE Transactions on Power Delivery*, vol. 25, no. 3, pp. 1410-1417, Jul. 2010.

[55] S. AsghariGovar, H. Seyedi, “Adaptive CWT-based transmission line differential protection scheme considering cross-country faults and CT saturation,” *IET Generation, Transmission & Distribution*, vol. 10, no. 9, pp. 2035-2041, Mar. 2016.

[56] S. Sarangi, A. K. Pradhan, “Adaptive α-plane line differential protection,” *IET Generation, Transmission & Distribution*, vol. 11, no. 10, pp. 2468-2477, Feb. 2017.

[57] M. L. S. Almeida, K. M. Silva, “Transmission lines differential protection based on an alternative incremental complex power alpha plane,” *IET Generation, Transmission & Distribution*, vol. 11, no. 1, pp. 10–17, 2017.

[58] A. Lei, X. Dong, S. Shi, and B. Wang, “Impedance-based pilot protection for ultra-high-voltage/extra-high-voltage transmission lines,” *IET Journal of Engineering*, vol. 2018, no. 15, pp. 904-907, Aug. 2018.

[59] C. Wang, G. Song, X. Kang, and J. Suonan, “Novel transmission line pilot protection based on frequency domain model recognition,” *IEEE Transactions on Power Delivery*, vol. 30, no. 2, pp. 1243-1250, Jun. 2014.

[60] B. Zhang, X. Yin, *Power system protective relaying*, 1st ed., Beijing: China Electric Power Press, 2005.

[61] S. M. Hashemi, M. T. Hagh and H. Seyedi, "A Novel Backup Distance Protection Scheme for Series-Compensated Transmission Lines," *IEEE Transactions on Power Delivery*, vol. 29, no. 2, pp. 699-707, Apr. 2014.

[62] Y. Liang, Z. Lu, W. Li, W. Zha and Y. Huo, "A Novel Fault Impedance Calculation Method for Distance Protection Against Fault Resistance," *IEEE Transactions on Power Delivery*, vol. 35, no. 1, pp. 396-407, Feb. 2020.

[63] S. Azizi, M. Sun, G. Liu, M. Popov and V. Terzija, "High-Speed Distance Relaying of the Entire Length of Transmission Lines Without Signaling," *IEEE Transactions on Power Delivery*, vol. 35, no. 4, pp. 1949-1959, Aug. 2020.

[64] Y. Zhong, X. Kang, Z. Jiao, et al. A Novel Distance Protection Algorithm for the Phase-Ground Fault [J]. *IEEE Transactions on Power Delivery*, vol. 29, no. 4, pp. 1718-1725, 2014.

[65] G. Li, B. Zhang, J. Wang, Z. Bo, T. Yip, D. Writer, et al., "DFIG-based wind farm electromagnetic dynamic model and impact on protection relay of transmission network", *Proc.2011 the International Conf. on Advanced Power System Automation and Protection*, pp. 694-698.

[66] G Pannell, D.J. Atkinson and B. Zahawi, "Analytical study of grid fault response of wind turbine doubly fed induction generator", *IEEE Transactions on Energy Conversion*, vol. 25, pp. 1081-1091, Dec. 2010.

[67] W. Wei, L. Zhang, B. Gao, Y. Tang, N. Chen and L. Zhu, "Frequency inconsistency in DFIG-based wind farm during outgoing transmission line faults and its effect on longitudinal differential protection," *The 4th Annual IEEE International Conference on Cyber Technology in Automation, Control and Intelligent*, pp. 25-30, 2014.

[68] F. Xiao, Y. Xia, K. Chen, K. Zhou, K. Zhang and D. Yang, "Study on the Influence of Distance Protection in Power Grid with New Energy Sources," *2019 IEEE 3rd Conference on Energy Internet and Energy System Integration (EI2)*, pp. 2568-2572, 2019.

[69] Q. Li, Y. Zhang, W. Yuan and F. Li, "A study on influence of wind power on positive sequence voltage polarized impedance relay," *2012 Power Engineering and Automation Conference*, 2012, pp. 1-4, doi: 10.1109/PEAM.2012.6612485.

[70] G. Feng, G. Zhe, Z. Shuang, Z. Jun and D. Jingming, "Influence on transmission line relay protection under DFIG-based wind farm intergration," *2015 5th International Conference on Electric Utility Deregulation and Restructuring and Power Technologies (DRPT)*, pp. 290-295, 2015.

[71] G. Yang, M. Dong, Z. Zhou, C. Zhou, D. Du, Z. Zhan and D. Yang, "The influences and countermeasures of wind farm access to transmission line differential protection," *2012 IEEE Power Electronics and Machines in Wind Applications*, pp. 1-4, 2012.

[72] Y. Li, K. Jia, T. Bi, R. Yan, W. Li and B. Liu, "Analysis of line current differential protection considering inverter-interfaced renewable energy power plants," *2017 IEEE PES Innovative Smart Grid Technologies Conference Europe (ISGT-Europe)*, pp. 1-6, 2017.

[73] Y. Liang, W. Li, G. Xu, "Performance Problem of Current Differential Protection of Lines Emanating from Photovoltaic Power Plants," *Sustainability*, vol. 12, no. 4, 1436, 2020.

[74] H. Gao, J. Li, B. Xu, "Principle and implementation of current differential protection in distribution networks with high penetration of DGs," *IEEE Transactions on Power Delivery*, vol. 32, pp. 565–574, 2017.

[75] B. Han, H. Li, G. Wang, "A Virtual Multi-Terminal current differential protection scheme for distribution networks with inverter-interfaced distributed generators," *IEEE Transactions on Smart Grid*, vol. 9, pp. 5418–5431, 2018.

[76] H. Li, C. Deng, Z. Zhang, Y. Liang, G. Wang, "An adaptive fault-component-based current differential protection scheme for distribution networks with inverter-

based distributed generators", *International Journal of Electrical Power & Energy Systems*, vol. 128, 106719, 2021.

[77] S. Chen, N. Tai, C. Fan, J. Liu, S. Hong, "Sequence-component-based current differential protection for transmission lines connected with IIGs," *IET Generation Transmission & distribution*, vol. 12, no. 12 pp. 3086–3096, 2018.

[78] Y. Feng, Z. Zhang, Q. Lai, X. Yin and H. Liu, "Impact of Inverter Interfaced Generators on Distance Protection," *2019 4th International Conference on Intelligent Green Building and Smart Grid (IGBSG)*, pp. 512-515, 2019.

[79] Y. Fang, K. Jia, Z. Yang, Y. Li and T. Bi, "Impact of Inverter-Interfaced Renewable Energy Generators on Distance Protection and an Improved Scheme," in *IEEE Transactions on Industrial Electronics*, vol. 66, no. 9, pp. 7078-7088, Sep. 2019.

[80] A. Hooshyar, M. A. Azzouz and E. F. El-Saadany, "Distance Protection of Lines Emanating From Full-Scale Converter-Interfaced Renewable Energy Power Plants—Part I: Problem Statement," in *IEEE Transactions on Power Delivery*, vol. 30, no. 4, pp. 1770-1780, Aug. 2015, doi: 10.1109/TPWRD.2014.2369479.

[81] A. Banaiemoqadam, A. Hooshyar and M. A. Azzouz, "A Control-Based Solution for Distance Protection of Lines Connected to Converter-Interfaced Sources During Asymmetrical Faults," *IEEE Transactions on Power Delivery*, vol. 35, no. 3, pp. 1455-1466, Jun. 2020.

[82] M. Sun, H. Wang and X. Zhu, "Fault characteristics of photolvoltaic power station and its influence on relay protection of transmission line," *5th IET International Conference on Renewable Power Generation (RPG) 2016*, 2016, pp. 1-5, doi: 10.1049/cp.2016.0584.

[83] Y. Q. Xia, K. K. Li and A. K. David, "Adaptive relay setting for stand-alone digital distance protection," *IEEE Transactions on Power Delivery*, vol. 9, no. 1, pp. 480-491, Jan. 1994.

[84] A. K. Pradhan and G. Joos, "Adaptive Distance Relay Setting for Lines Connecting Wind Farms," *IEEE Transactions on Energy Conversion*, vol. 22, no. 1, pp. 206-213, March 2007.

[85] H. Sadeghi, "A novel method for adaptive distance protection of transmission line connected to wind farms", *International Journal of Electrical Power & Energy Systems*, vol. 43, no. 1, pp. 1376-1382, 2012.

[86] S. Paladhi and A. K. Pradhan, "Adaptive distance protection for lines connecting converter-interfaced renewable plants," *IEEE Journal of Emerging and Selected Topics in Power Electronics*, vol. 9, no. 6, Dec. 2021.

[87] Y. Liang, W. Li, and Y. Huo, "Zone I distance relaying scheme of lines connected to MMC-HVDC stations during asymmetrical faults: problems, challenges, and solutions," *IEEE Transactions on Power Delivery*, vol. 36, no. 5, pp. 2929-2941, Oct. 2021.

[88] Y. Liang, W. Li and W. Zha, "Adaptive mho characteristic-based distance protection for lines emanating from photovoltaic power plants under unbalanced faults," *IEEE Systems Journal*, vol. 15, no. 3, pp. 3506-3516, Sept. 2021.

[89] R. Leelaruji, L. Vanfretti, M. Ghandhari, et al. ”Coordination of protection and VSC-HVDC systems for mitigating cascading failures,” *International Conference on Power System Technology, POWERCON*, pp: 1-8, 2010.

[90] P. Kundu and A. K. Pradhan, "Power Network Protection Using Wide-Area Measurements Considering Uncertainty in Data Availability," *in IEEE Systems Journal*, vol. 12, no. 4, pp. 3358-3368, Dec. 2018.

[91] M. K. Jena, S. R. Samantaray and B. K. Panigrahi, "A New Decentralized Approach to Wide-Area Back-Up Protection of Transmission Lines," *in IEEE Systems Journal*, vol. 12, no. 4, pp. 3161-3168, Dec. 2018.

[92] S. M. Hashemi and M. Sanaye-Pasand, "A New Predictive Approach to Wide-Area Out-of-Step Protection," *in IEEE Transactions on Industrial Informatics*, vol. 15, no. 4, pp. 1890-1898, Apr. 2019.

[93] W. Li et al., "A Fully Decentralized Multi-Agent Fault Location and Isolation for Distribution Networks With DGs," *in IEEE Access*, vol. 9, pp. 27748-27757, 2021.

[94] P. Wang and M. Govindarasu, "Multi-Agent Based Attack-Resilient System Integrity Protection for Smart Grid," *in IEEE Transactions on Smart Grid*, vol. 11, no. 4, pp. 3447-3456, Jul. 2020.

[95] T. S. Aghdam, H. Kazemi Karegar and H. H. Zeineldin, "Variable Tripping Time Differential Protection for Microgrids Considering DG Stability," *in IEEE Transactions on Smart Grid*, vol. 10, no. 3, pp. 2407-2415, May 2019.

[96] M. N. Alam, "Adaptive Protection Coordination Scheme Using Numerical Directional Overcurrent Relays," *in IEEE Transactions on Industrial Informatics*, vol. 15, no. 1, pp. 64-73, Jan. 2019.

[97] M. K. Jena, S. R. Samantaray and B. K. Panigrahi, "A New Adaptive Dependability-Security Approach to Enhance Wide Area Back-Up Protection of Transmission System," *in IEEE Transactions on Smart Grid*, vol. 9, no. 6, pp. 6378-6386, Nov. 2018.

[98] Guangqi Li, *Power System Transient Analysis*, 3rd ed, China Electric Power Press, China, 2007. (In Chinese)

[99] *Technische regeln für den anschluss von kundenanlagen an das hochspannungsnetz und deren betrieb (TAR Hochspannung)*, VDE-AR-N 4120 Anwendungsregel: 2018-11, 2018.

[100] K. Ma, Z. Chen, Z. Liu, C. L. Bak, M. Castillo, "Protection collaborative fault control for power electronic-based power plants during unbalanced grid faults", *International Journal of Electrical Power and Energy Systems*, vol. 130, 107009, Sep. 2021.

[101] G. Zziegler, *Numerical differential protection: principles and applications*, 2nd ed, Nuremberg, Germany: Siemens AG, 2012.

[102] K. Ma, Z. Chen, C. L. Bak, Z. Liu, M. Castillo, R. E. Torres-Olguin, N. Qin, "Novel differential protection using model recognition and unsymmetrical vector reconstruction for the transmission line with wind farms connection", *International Journal of Electrical Power and Energy Systems*, vol. 123, 106311, Dec. 2020.

[103] K. Ma, Y. Wang, Z. Chen, "Analysis of the line current differential protection considering inverter-interfaced generation station and countermeasures", *Journal of Yangtze University*, accepted.

[104] G. Zziegler, *Numerical distance protection: principles and applications*, 4th ed, Nuremberg, Germany: Siemens AG, 2012.

[105] K. Ma, Z. Liu, Z. Chen, C. L. Bak, M. Castillo, "Influence of converter-based power sources on the distance relay under system asymmetrical Faults," *2020 12th IEEE PES Asia-Pacific Power and Energy Engineering Conference (APPEEC)*, Nanjing, China, 2020.

[106] B. Nhlapo and K. Awodele, "Review and comparison of the South African grid code requirements for wind generation with the European countries' grid codes," *2020 International SAUPEC/RobMech/PRASA Conference*, pp. 1-6, 2020.

[107] D. T. Dantas, E. L. Pellini, and Jr G. Manassero, "Time-Domain Differential Protection Method Applied to Transmission Lines," *IEEE Transaction on Power Delivery*, vol. 33, no. 6, pp. 2634-2642, Dec. 2018.

[108] L. Tang, X. Dong, S. Luo, S. Shi, and B. Wang, “A New Differential Protection of Transmission Line Based on Equivalent Travelling Wave,” *IEEE Transaction on Power Delivery*, vol. 32, no. 3, pp. 1359-1369, Jun. 2017.

[109] K. Ma, Z. Chen, C. L. Bak, Z. Liu, “A Novel Model Recognition -based Current Differential Protection in Time-Domain”, *in Proceedings of 2019 IEEE Milan PowerTech*, Milano, Italy, 2019.

[110] K. Ma, Z. Liu, C. L. Bak, Z. Chen, “Novel differential protection based on the ratio of model error indices in time-domain for transmission cable system”, *Journal of Electric Power Systems Research*, vol. 180, 106077, Mar. 2020.

[111] C. L. Bak, F. Silva, “High voltage AC underground cable systems for power transmission – a review of the Danish experience: part 2,” *Journal of Electric Power System Research*, vol. 140, pp. 984-994, 2016.

[112] Y. Xue, D. Finney, B. Le, “Charging Current in Long Lines and High-Voltage Cables – Protection Application Considerations,” *67th Annual Georgia Tech Protective Relaying Conference*, Atlanta, Georgia, pp. 1-17, 2013.

[113] P.S. Rane, R.D. Jawale, S.D. Bhaisare, P.D. Debre, “Impact of capacitive current of EHV/UHV lines on current differential protection,” *2016 International Conference on Energy Efficient Technologies for Sustainability*, Nagercoil, India, pp. 372-376, 2016.

[114] J. Bell, A. Hargrave, G. Smelich, and B. Smyth, “Considerations When Using Charging Current Compensation in Line Current Differential Applications,” *72nd Annual Conference for Protective Relay Engineers*, pp. 1-11, Mar. 2019.

[115] A. Khanna, “Application of Differential Protection to Long Power Cables – Cable Modelling and Charging Current Compensation Methods,” *IET DPSP*, Copenhagen, Denmark, Mar. 2014.

[116] *IEEE Guide for Application of Digital Line Current Differential Relays Using Digital Communication*. IEEE Std C37.243, 2015.

[117] K. Ma, H. K. Høidalen, Z. Chen, C. L. Bak, “Improved zone 1 top-line tilting scheme for the polygonal distance protection in the outgoing line of type-4 wind parks”, *CSEE Journal of Power and Energy Systems*, second revision.

[118] *DIgSILENT PowerFactory 2020, Technical Reference, External Grid (ElmXnet)*, DIgSILENT GmbH. https://www.digsilent.de

[119] D. Zheng, W. Zhang, S. N. Alemu, P. Wang, G. T. Bitew, D. Wei, J. Yue, *Microgrid Protection and Control*, Academic Press, 2021, pp: 13-44, ISBN 9780128211892.

[120] N. Hoffmann, F. W. Fuchs, "Minimal invasive equivalent grid impedance estimation in inductive-resistive power networks using extended Kalman filter," *IEEE Transactions on Power Electronics*, vol. 29, no. 2 pp. 631-641, 2014.

[121] C. Santiago, J. B. Emilio, P. Daniel, J. R. Francisco, and H. Francisco, "Grid Impedance Monitoring System for Distributed Power Generation Electronic Interfaces," *IEEE Transactions on instrumentation and measurement*, vol. 58, no. 9, Sep. 2009.

[122] A. Hooshyar, E. F. El-Saadany, and M. Sanaye-Pasand, "Fault type classification in microgrids including photovoltaic DGs," *IEEE Transactions on Smart Grid*, vol. 7, no. 5, pp. 2218–2229, Sep. 2016.

[123] S. Paladhi and A. K. Pradhan, "Adaptive Fault Type Classification for Transmission Network Connecting Converter-Interfaced Renewable Plants," *in IEEE Systems Journal*, vol. 15, no. 3, pp. 4025-4036, Sep. 2021.

[124] CIGRE Working Group C4.503, Power system test cases for EMT-type simulation studies. CIGRE Technical Report, Aug. 2018. [Online]. Available: https://e-cigre.org/publication/736-power-system-test-casesfor-emt-type-simulation-studies.

[125] C.F. Jensen, Online Location of Faults on AC Cables in Underground Transmission Systems. Department of Energy Technology, Aalborg University, Jul. 2013.

[126] J. Sadeh, A.M. Ranjbar, N. Hajsaid and R. Feuillet, "Accurate Fault Location Algorithm for Power Transmission Lines," *European Transactions on Electrical Power*, vol. 10, no. 5, pp. 313-318, Sept./ Oct. 2000.

APPENDICES

Appendix A. Line parameters for modeling and simulation

TABLE A-1 PARAMETERS OF THE TEST SYSTEM IN FIGURE 2-6

Category		Sequence parameters	
		1/2 sequence	0 sequence
Line parameters in per km	Resistance Ω	0.02089	0.30299
	Inductance mH	0.846704	3.154451
	Capacitance uF	0.01377995	0.00841993
Transformer short-circuit voltage %	T_1	10.5	3.5
	T_2	11	11
	T_f	10.5	3
		Other parameters	
Loads MW	L_d	200	
Line length km	$L_{2\text{-}3}$ / $L_{3\text{-}4}$	80 / 10	

*Note: per unit length line data is cited from [124]

TABLE A-2 PARAMETERS OF THE TEST SYSTEM IN FIGURE 2-16 [100]

Category		**Sequence parameters**	
		1/2 sequence	0 sequence
Line parameters in per km	Resistance Ω	0.0424	0.1696
	Inductance mH	0.739994	2.959996
	Capacitance uF	0.0023	0.002306
Transformer short-circuit voltage %	T_S (Ynd110/50)	10.5	3.5
Grid impedance	*Zr* Ω	3.1436∠88.2º	4.7154∠88.2º

TABLE A-3 PARAMETERS OF THE TEST SYSTEM IN FIGURE 3-4 [109]

Category / **Sequence**	Sequence parameter in per unit length /km			Other
	Resistance Ω	Inductance mH	Capacitance uF	Length km
Positive sequence	0.01958	0.8192	0.0135	100
Zero sequence	0.1828	2.74	0.0092	

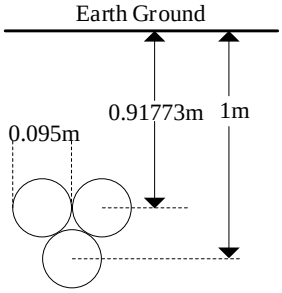

Figure A-1 Cable system configuration [110]

TABLE A-4 ELECTRICAL DATA OF 165 KV SINGLE-CORE CABLE [125]

Category	Parametres
Type of core	1200 mm^2 Cu
Diameter of conductor mm	41.5
Thickness of insulation mm	19.75
Thickness of sheath mm	1.11
Thickness of oversheath mm	5.89
Resistivity of conductor Ωm	3.156e-08 (at 20 °C)
Resistivity of sheath Ωm	3.65e-08 (at 20 °C)
Relative permittivity of insulation	2.74
Relative permittivity of oversheath	2.3

TABLE A-5 PARAMETERS OF THE CABLE TRANSMISSION SYSTEM [110]

Category		Sequence parameters		Other parameters
		1/2 sequence	0 sequence	
Sending end source Es	Rs	0.586	0.294	400kV (0°)
	Xs	17.62	14.52	
Recieving end source Er	Rr	0.012	0.01	50kV (-5°)
	Xr	0.322	0.28	
Sending end transformer Ts	uk%	12	8	250 MVA Yd/Yd
Recieving end transformer Tr	uk%	8	5	250 MVA Yd/Δ
Cable section km	# 1	\	\	30
	# 2	\	\	30

* uk% short-circuit voltage.

TABLE A-6 PARAMETERS OF THE EQUIVALENT GRID IN FIGURE 4-8 [118]

Category	Parametres
Short-circuit power	3000 MVA
Impedance ratio X_0/X_1	1.5
X/R ratio	4
c-Factor	1.1
Transient time constants T'_d, T'_q	1, 1
Subtransient time constants T''_d, T''_q	0.1, 0.1
Synchronous reactances x_d, x_q (p.u.)	0.2, 0.2
Transient reactances x'_d, x'_q (p.u.)	0.2, 0.2
Power factor	0.8

Appendix B. Bergeron model-based time-domain current (along the line) computation method [109]

Figure B-1 illustrates the lossy line model. In the figure, parameters D and R are the total length and resistance of transmission line, respectively. u_s, i_s and u_r, i_r denotes the two-sided line currents and terminal voltages. Based on the Bergeron model-based time-domain computation method [109, 126], one can calculate any current on the line by the sending (or receiving) end instantaneous current and voltage, as expressed in (B.1).

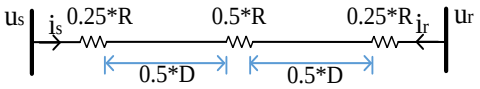

Figure B-1 Bergeron transmission line model

$$\begin{aligned} i(x,t) = & \frac{Z_c + rx/4}{2Z_c^2}\left[u_s\left(t+\frac{x}{v}\right) - \left(Z_c + rx/4\right) i_s\left(t+\frac{x}{v}\right)\right] \\ & - \frac{Z_c - rx/4}{2Z_c^2}\left[u_s\left(t-\frac{x}{v}\right) + \left(Z_c - rx/4\right) i_s\left(t-\frac{x}{v}\right)\right] \\ & - \frac{rx}{4Z_c^2}\left[u_s(t) - \left(rx/4\right) i_s(t)\right] \end{aligned} \tag{B.1}$$

where

$v = 1/\sqrt{lc}$ —wave velocity;

$Z_c = \sqrt{(l/c)}$ —surge impedance;

r, l, c, —per unit values of the line resistance, inductance, and capacitance

x —distance from computation point to terminal m.

Appendix C. Least-square method-based parameter estimation

The unknown parameters R_{eq} and L_{eq} in the restraining equation (3.14) are estimated by using the least-square method [39, 102, 110]. Firstly, define the discrete energy function of parameter error to be estimated in the restraining equation (3.14),

$$J = \sum_{k=1}^{N} \left(u_{cd}(k) + R_{eq} i_{cd}(k) + L_{eq} D(k) \right)^2 \tag{C.1}$$

From the partial differential equation of (C.1) to R_{eq} and L_{eq}, it yields,

$$\begin{cases} \hat{R} = \dfrac{\sum_{k=1}^{N} u_{cd}(k) i_{cd}(k) \sum_{k=1}^{N} \left(D(k) \right)^2 - \sum_{k=1}^{N} u_{cd}(k) D(k) \sum_{k=1}^{N} i_{cd}(k) D(k)}{\sum_{k=1}^{N} \left(i_{cd}(k) \right)^2 \sum_{k=1}^{N} \left(D(k) \right)^2 - \left(\sum_{k=1}^{N} i_{cd}(k) D(k) \right)^2} \\ \hat{L} = \dfrac{\sum_{k=1}^{N} \left(i_{cd}(k) \right)^2 \sum_{k=1}^{N} u_{cd}(k) D(k) - \sum_{k=1}^{N} u_{cd}(k) i_{cd}(k) \sum_{k=1}^{N} i_{cd}(k) D(k)}{\sum_{k=1}^{N} \left(i_{cd}(k) \right)^2 \sum_{k=1}^{N} \left(D(k) \right)^2 - \left(\sum_{k=1}^{N} i_{cd}(k) D(k) \right)^2} \end{cases} \tag{C.2}$$

where

$D(k) = \left(i_{cd}(k) - i_{cd}(k-1) \right) / T_s$.

T_S —sampling period.

N —data window.

ISSN (online): 2446-1636
ISBN (online): 978-87-7573-908-0

AALBORG UNIVERSITY PRESS